

The effects of axial flow and surface mass-flux on the stability  
of the rotating-sphere boundary layer

Thesis submitted for the degree of  
Doctor of Philosophy  
at the University of Leicester

by

Alistair Barrow  
Department of Mathematics  
University of Leicester

March 2013

# The effects of axial flow and surface mass-flux on the stability of the rotating-sphere boundary layer

Alistair Barrow

## Abstract

A theoretical investigation is carried out into the linear stability of the boundary-layer flow around a rotating sphere immersed in an incompressible viscous fluid. Two potentially stabilising mechanisms are considered: a forced uniform axial flow in the surrounding fluid, and the introduction of mass suction/injection through the surface of the sphere. The investigation is broadly split into a “local” analysis, where a parallel-flow assumption is made which limits the study to individual latitudinal positions; and a “global” analysis, where the entire streamwise extent of the flow is considered. In the local analysis, both stationary and travelling convective disturbances are considered. For a representative subset of the parameter space, critical Reynolds numbers are presented for the predicted onset of convective and absolute instabilities. Axial flow and surface suction are typically found to postpone the onset of all types of instability by raising the critical Reynolds number, whereas surface injection has the opposite effect. This is further demonstrated by a consideration of the convective and absolute growth rates at various parameter values.

The results of the global analysis suggest that the rotating sphere can support a self-sustained, linearly globally-unstable global mode for sufficiently large rotation rates. This is in contrast to the case of the rotating disk, where it is generally accepted that self-sustained linear global modes do not occur.

# Acknowledgements

I am very grateful to my supervisor, Dr. Stephen Garrett, whose support and guidance throughout this work have been invaluable. I would also like to extend my thanks to my friends, family and colleagues, for their continued encouragement.

This work was funded by the Department of Mathematics and the College of Science and Engineering at the University of Leicester.

# Contents

<b>Abstract</b>	<b>i</b>
<b>1 Introduction</b>	<b>1</b>
1.1 Motivation and literature review . . . . .	1
1.2 Stability theory . . . . .	10
1.2.1 Local stability . . . . .	10
1.2.2 Global stability . . . . .	14
<b>2 Incompressible boundary-layer flow over a rotating sphere</b>	<b>18</b>
2.1 Formulation and governing equations . . . . .	18
2.2 Obtaining the steady flow . . . . .	21
2.2.1 A series-solution method . . . . .	22
2.2.2 A full numerical solution . . . . .	25
2.2.3 Analysis of error in the series-solution method . . . . .	26
2.3 Boundary-layer flow over a rotating sphere with heating . . . . .	27
<b>3 Boundary-layer flow over a rotating sphere with heating and mass flux</b>	<b>31</b>
<b>4 Introducing an axial flow</b>	<b>41</b>
4.1 Formulation . . . . .	41
4.2 Results . . . . .	43
4.3 Error in the series-solution method . . . . .	48

<b>5</b>	<b>Convective stability analysis with emphasis on critical Reynolds number</b>	<b>51</b>
5.1	Derivation of the perturbation equations . . . . .	52
5.2	Solution method . . . . .	57
5.3	Convective stability analysis of stationary vortices . . . . .	60
5.4	Convective stability analysis of non-stationary vortices . . . . .	72
5.5	Summary of results . . . . .	80
<b>6</b>	<b>Convective growth rates</b>	<b>83</b>
6.1	Growth rates . . . . .	83
6.2	Results . . . . .	84
<b>7</b>	<b>Absolute stability analysis</b>	<b>88</b>
7.1	Absolute instability . . . . .	88
7.2	Results . . . . .	89
7.2.1	Comparison to experiment . . . . .	91
7.2.2	Absolute growth rates . . . . .	93
<b>8</b>	<b>Global stability analysis</b>	<b>95</b>
8.1	Introduction . . . . .	95
8.2	Formulation . . . . .	95
8.3	Global modes . . . . .	98
8.4	Conclusions . . . . .	106
<b>9</b>	<b>Global instability with surface mass-flux and axial flow</b>	<b>107</b>
<b>10</b>	<b>Conclusions</b>	<b>112</b>
10.1	Review and summary . . . . .	112
10.2	Applications . . . . .	115
10.3	Future work . . . . .	116

# List of Tables

4.1	Error in the series-solution method with $\text{Pr} = 0.7$ , $\iota = 0.0$ . . . . .	49
4.2	Error in the series-solution method with $\text{Pr} = 0.7$ , $\theta = 30^\circ$ . . . . .	49
5.1	Critical Reynolds numbers for $\tau = 0.00$ . . . . .	69
5.2	Critical Reynolds numbers for $\tau = 0.10$ . . . . .	69
5.3	Critical Reynolds numbers for $\tau = 0.25$ . . . . .	69
5.4	Number and angle of vortices for $\tau = 0.00$ . . . . .	71
5.5	Number and angle of vortices for $\tau = 0.10$ . . . . .	71
5.6	Number and angle of vortices for $\tau = 0.25$ . . . . .	71
5.7	$R_c$ for a range of parameter values at $\theta = 10^\circ$ . . . . .	78
5.8	$R_c$ for a range of parameter values at $\theta = 30^\circ$ . . . . .	78
5.9	$R_c$ for a range of parameter values at $\theta = 50^\circ$ . . . . .	79
5.10	$R_c$ for a range of parameter values at $\theta = 70^\circ$ . . . . .	79
5.11	Vortex number and angle for a range of parameter values at $\theta = 10^\circ$ .	80
5.12	Vortex number and angle for a range of parameter values at $\theta = 30^\circ$ .	81
5.13	Vortex number and angle for a range of parameter values at $\theta = 50^\circ$ .	81
5.14	Vortex number and angle for a range of parameter values at $\theta = 70^\circ$ .	82
6.1	Vortex speed, $c$ , giving maximum spatial growth rate at $\theta = 30^\circ$ . . .	85
7.1	$R_a$ at selected latitudes for $\iota = 0.0$ . . . . .	91
7.2	$R_a$ at selected parameter values for $\theta = 30^\circ$ . . . . .	91
7.3	Maximum temporal growth rates for absolute instability at $\theta = 30^\circ$ .	93
8.1	Saddle-point location and associated values of global frequencies . . .	103

9.1  $\gamma_G$  location and magnitude for  $\iota = 0.5, \tau = 0$  . . . . . 108

9.2  $\gamma_G$  location and magnitude for  $\iota = -0.5, \tau = 0$  . . . . . 109

9.3  $\gamma_G$  location and magnitude for  $\iota = 0, \tau = 0.15$  . . . . . 110

9.4  $\gamma_G$  location and magnitude for  $\iota = -0.5, \tau = 0.15$  . . . . . 110

9.5  $\gamma_G$  location and magnitude for  $\iota = 0.5, \tau = 0.15$  . . . . . 111

# List of Figures

1.1	Photograph of a rotating sphere . . . . .	2
1.2	Convective and absolute instability . . . . .	12
1.3	Integration contours . . . . .	13
2.1	The coordinate system . . . . .	19
2.2	Velocity profiles for $U(\eta)$ , $V(\eta)$ and $W(\eta)$ . . . . .	25
2.3	Comparison of the series-solution method of Banks (1965) to the numerical NAG solution . . . . .	26
2.4	Comparison of the method of Jain & Venkataraman (1966) to the numerical NAG solution . . . . .	27
2.5	Temperature profiles for a one-unit temperature difference . . . . .	30
3.1	The effects of mass flux on $U$ . . . . .	33
3.2	The effects of mass flux on $V$ . . . . .	33
3.3	The effects of mass flux on $W$ . . . . .	34
3.4	The effects of mass flux on $T$ . . . . .	34
3.5	Velocity and temperature profiles at $\theta = 10^\circ$ . . . . .	36
3.6	Velocity and temperature profiles at $\theta = 40^\circ$ . . . . .	36
3.7	Velocity and temperature profiles at $\theta = 70^\circ$ . . . . .	37
3.8	Temperature profiles at $\iota = 0$ . . . . .	38
3.9	Temperature profiles at $\iota = -1$ . . . . .	38
3.10	Temperature profiles at $\iota = 1$ . . . . .	39
3.11	The effects of mass flux on $T$ . . . . .	39
3.12	Temperature profiles at $\text{Pr} = 7$ . . . . .	40

4.1	$U$ profiles at selected $\theta$ , $\iota$ and $\tau$ . . . . .	44
4.2	$V$ profiles at selected $\theta$ , $\iota$ and $\tau$ . . . . .	44
4.3	$W$ profiles at selected $\theta$ , $\iota$ and $\tau$ . . . . .	45
4.4	$T$ profiles for $\text{Pr} = 0.7$ at selected $\theta$ , $\iota$ and $\tau$ . . . . .	45
4.5	$T$ profiles for $\text{Pr} = 4.0$ at selected $\theta$ , $\iota$ and $\tau$ . . . . .	46
4.6	$T$ profiles for $\text{Pr} = 7.0$ at selected $\theta$ , $\iota$ and $\tau$ . . . . .	46
5.1	Spatial branches at $\theta = 30^\circ$ , $\tau = \iota = 0$ . . . . .	61
5.2	Neutral stability curves for $\alpha_r$ and $\beta$ at $\tau = 0$ , $\iota = 0$ (still fluid) . . .	62
5.3	Neutral stability curves for $\alpha_r$ and $\beta$ at $\tau = 0$ , $\iota = 1.0$ . . . . .	63
5.4	Neutral stability curves for $\alpha_r$ and $\beta$ at $\tau = 0$ , $\iota = -1.0$ . . . . .	63
5.5	The effect of mass flux on the neutral stability curves at $\theta = 10^\circ$ , $\tau = 0$	64
5.6	The effect of mass flux on the neutral stability curves at $\theta = 10^\circ$ , $\tau = 0.1$ . . . . .	64
5.7	The effect of mass flux on the neutral stability curves at $\theta = 10^\circ$ , $\tau = 0.25$ . . . . .	65
5.8	The effect of mass flux on the neutral stability curves at $\theta = 50^\circ$ , $\tau = 0$	65
5.9	The effect of mass flux on the neutral stability curves at $\theta = 50^\circ$ , $\tau = 0.1$ . . . . .	66
5.10	The effect of mass flux on the neutral stability curves at $\theta = 50^\circ$ , $\tau = 0.25$ . . . . .	66
5.11	Illustration of one case where small magnitudes of axial flow decrease $R_c$ . . . . .	68
5.12	Critical Reynolds numbers for the onset of convective instability . . .	70
5.13	Neutral stability curves with non-stationary vortices at $\theta = 10^\circ$ , $\tau =$ $0$ , $\iota = 0$ . . . . .	73
5.14	Neutral stability curves with non-stationary vortices at $\theta = 70^\circ$ , $\tau =$ $0$ , $\iota = 0$ . . . . .	73
5.15	Neutral stability curves with non-stationary vortices at $\theta = 10^\circ$ , $\tau =$ $0.2$ , $\iota = 0$ . . . . .	74

5.16	Neutral stability curves with non-stationary vortices at $\theta = 70^\circ$ , $\tau = 0.2$ , $\iota = 0$ . . . . .	74
5.17	Neutral stability curves with non-stationary vortices at $\theta = 10^\circ$ , $\tau = 0$ , $\iota = 1$ . . . . .	75
5.18	Neutral stability curves with non-stationary vortices at $\theta = 70^\circ$ , $\tau = 0$ , $\iota = 1$ . . . . .	76
5.19	Neutral stability curves with non-stationary vortices at $\theta = 10^\circ$ , $\tau = 0$ , $\iota = -1$ . . . . .	76
5.20	Neutral stability curves with non-stationary vortices at $\theta = 70^\circ$ , $\tau = 0$ , $\iota = -1$ . . . . .	77
5.21	Neutral stability curves with non-stationary vortices at $\theta = 10^\circ$ , $\tau = 0.2$ , $\iota = 1$ . . . . .	77
5.22	Neutral stability curves with non-stationary vortices at $\theta = 70^\circ$ , $\tau = 0.2$ , $\iota = 1$ . . . . .	78
6.1	Spatial growth rates over a range of $c$ , $\tau$ and $\iota$ . . . . .	84
6.2	Spatial branches showing growth rates for various $R$ . . . . .	86
7.1	Neutral absolute instability curves at $\theta = 30^\circ$ . . . . .	90
7.2	Critical Reynolds numbers for absolute instability at $\theta = 30^\circ$ . . . . .	92
7.3	Reynolds numbers at the onset of turbulence . . . . .	92
8.1	Plots of absolute frequency at various $R$ . . . . .	100
8.2	Level curves of $\gamma_i^\circ$ in the complex- $\mathcal{S}$ plane at $\bar{n} = 0.05$ . . . . .	101
8.3	Level curves of $\gamma_i^\circ$ in the complex- $\mathcal{S}$ plane at $\bar{n} = 0.15$ . . . . .	102
8.4	Level curves of $\gamma_i^\circ$ in the complex- $\mathcal{S}$ plane at $\bar{n} = 0.25$ . . . . .	102
8.5	Neutral curve for the onset of linear global instability . . . . .	104
8.6	Comparison of the experimentally-observed onset of turbulence to our results . . . . .	105

# Nomenclature

Symbol	Meaning
$r^*$	Distance from sphere centre
$\theta$	Angle of latitude measured from pole
$\phi$	Angle of azimuth
$U^*, V^*, W^*$	Dimensional velocity in directions $\theta, \phi, r^*$ , respectively
$P^*$	Dimensional pressure
$U, V, W$	Non-dimensional velocity in directions $\theta, \phi, r^*$ , respectively
$\eta$	Non-dimensional distance from sphere surface
$t^*$	Time
$a^*$	Sphere radius
$\Omega^*$	Angular velocity of sphere
$\rho^*$	Fluid density
$\nu^*$	Kinematic viscosity of fluid
$\mathbf{u}^*$	Dimensional velocity vector ( $U^*, V^*, W^*$ )
$\delta^*$	Boundary-layer thickness $\left[ = (\nu^*/\Omega^*)^{\frac{1}{2}} \right]$
Pr	Prandtl number
$T^*$	Temperature
$T_a^*$	Uniform constant temperature of sphere surface
$T_\infty^*$	Uniform constant temperature of the far field

<b>Symbol</b>	<b>Meaning</b>
$F_i, G_i, H_i, M_i$	Non-dimensional functions of $\eta$ (for $i = 1, 3, 5, \dots$ )
$U_0^*$	Slip velocity
$\iota$	Surface mass-flux: positive values for injection, negative for suction
$U_\infty^*$	Free-stream axial flow speed of the fluid
$\tau$	Non-dimensional axial flow speed
$R$	Reynolds number [= $a^*\delta^*\Omega^*/\nu^*$ ]
$R_S$	“Spin” Reynolds number [= $R^2$ ]
$R_X$	“Local” Reynolds number [= $R^2\theta \sin \theta$ ]
$\alpha^*$	Latitudinal wavenumber
$\beta^*$	Azimuthal wavenumber
$\gamma^*$	Disturbance frequency
$\alpha$	Non-dimensional latitudinal wavenumber [= $\alpha^*\delta^*$ ]
$\beta$	Non-dimensional azimuthal wavenumber [= $\beta^*\delta^*$ ]
$\gamma$	Non-dimensional disturbance frequency [= $\gamma^*\delta^*/a^*\Omega^*$ ]
$n$	Number of vortices around the azimuth [= $\beta R \sin \theta$ ]
$\varepsilon$	Ratio of boundary-layer thickness to body size [= $(\nu^*/\Omega^*)^{\frac{1}{2}}/a^*$ ]
$\bar{n}$	Scaled $n$ [= $\varepsilon n$ ]
$\epsilon$	Angle of spiral vortices [= $\tan^{-1}(\beta/\alpha_r)$ ]
$\mathcal{S}$	Slowly-varying latitudinal spatial coordinate

# Chapter 1

## Introduction

### 1.1 Motivation and literature review

This thesis is concerned with the boundary-layer flow over a rotating sphere under various conditions. In the basic case of a sphere rotating in otherwise still fluid, experimental work by, for example, Sawatzki (1970) and Kohama & Kobayashi (1983), shows that for sufficiently high rotation rates, three regions can be observed, each characterised by distinct flow regimes. Close to the pole, the flow is laminar; at higher latitudes, co-rotating spiral vortices, characteristic of cross-flow instability, are present; and at still higher latitudes, the flow undergoes transition and becomes turbulent (see Figure 1.1). As the rotation rate is increased, the unstable regions move closer to the pole in a manner similar to that observed over rotating disks and cones; see Gregory *et al.* (1955), Kobayashi *et al.* (1980), Kohama (1984b) and Kobayashi *et al.* (1987), for example. Some previous theoretical work exists to characterise the instability mechanisms at work within the rotating-sphere boundary layer, most notably by Garrett & Peake (2002, 2004) and Garrett (2010c), and the aim of this thesis is to further this knowledge with particular emphasis on aerodynamically significant flow configurations and suggest possible methods for flow control. In particular we look at the effects of axial flow and surface mass-flux on *local* and *global* instabilities within the boundary layer.

The mathematical description of the steady boundary-layer flow (i.e. that within

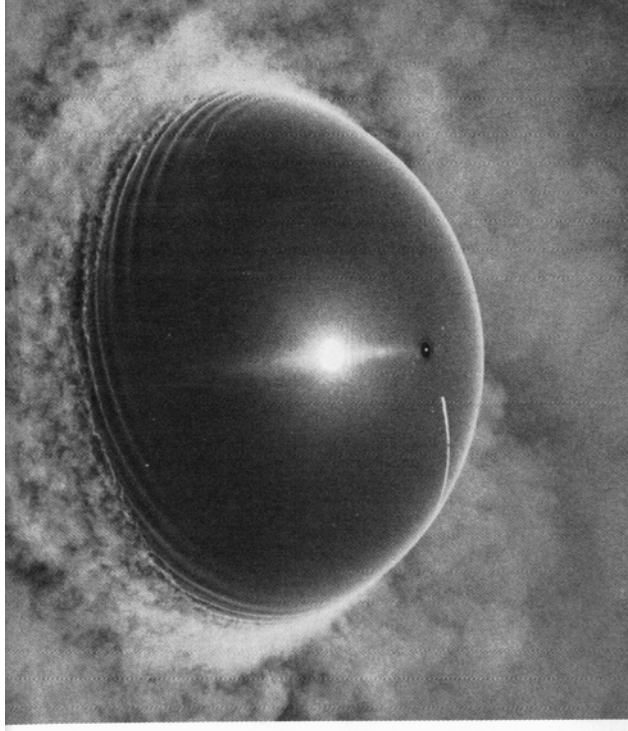


Figure 1.1: Photograph of a rotating sphere illustrating the region of spiral vortices (van Dyke, 1982).

the laminar regime close to the pole) around a sphere rotating within otherwise still fluid has been the subject of some research. Notably, Howarth (1951) derives the partial differential equations that govern the steady flow and develops a solution method that employs a series expansion in powers of the latitudinal angle measured from the pole. These early results, though later shown to be subject to significant numerical inaccuracies, are consistent with the observation that there is an inflow of fluid near the poles, with fluid moving over the sphere surface and being ejected near the equator, and reflect its similarity to the von Kármán flow over a rotating disk which is known to act as a fluid pump (von Kármán (1921)). Improved series-solution methods are later used by Banks (1965) to better approximate the profiles of the velocity components and later Manohar (1967) and Banks (1976) apply more accurate finite-difference techniques to the same problem. Further theoretical research is carried out by El-Shaarawi *et al.* (1985), who also develop and use a finite-difference technique, and include an enforced axial flow in their model. More recently, Garrett and co-workers (Garrett & Peake (2002, 2004), Garrett (2002), Garrett *et al.* (2009a)) have used commercially available NAG routines to solve the

resulting partial differential equations that govern the steady flow.

There has been little directly-pertinent experimental work on the boundary layer on a rotating sphere, beyond the original observations of the three distinct flow regions. Papers by various authors including Noordsij & Rotte (1967), Noordsij & Rotte (1968), Tanaka & Tago (1975) and Furuta *et al.* (1975) present some work in this area, but they are mostly concerned with its effect on mass-transfer rate in electrolysis. However, El-Shaarawi *et al.* (1987) provide measurements of the velocity components within the boundary layer, and later work by Kobayashi *et al.* (1988), Kobayashi & Arai (1990) places emphasis on instability and transition. These papers include results for spheres rotating in both otherwise-still fluids and axial flows.

As observed by Howarth (1951), the behaviour of fluid near the poles of the sphere approximates that over a rotating disk. Physically this is of no surprise as the sphere is locally flat near to the pole and so acts as a rotating disk in that region. It might be expected, therefore, that the results presented here for positions close to the pole show close agreement with those obtained for a rotating disk. For lower rotation rates, where the transitional behaviour manifests away from the pole, the effects of the sphere's surface curvature lead to distinct behaviour and critical parameters. The relationship between disks and spheres means that previous work on disks is relevant to this research. Indeed the observation of spiral vortices within the second of the three flow regions is closely related to the observations of Gregory *et al.* (1955), Kobayashi *et al.* (1980), Malik *et al.* (1981) and Wilkinson & Malik (1985). Further theoretical and experimental work on the rotating-disk boundary layer is performed by Lingwood (1995a, 1996). Kobayashi *et al.* (1980) and Malik *et al.* (1981) find that although the instability waves first appear at different points in the parameter space, dependent on the rotation rate, the onset of turbulence always occurs at a fixed local Reynolds number,  $R_X$ . Garrett & Peake (2002) observe that the results of Kohama & Kobayashi (1983) for the rotating sphere also indicate the occurrence of turbulence at a fixed  $R_X$ , up to a latitude of  $70^\circ$  from the pole, and they give its approximate value as  $R_X = 2.5 \times 10^5$ .

Kobayashi & Arai (1990) observe that for large rotation rates, the vortices that arise in the transitional region are stationary with respect to the sphere surface, while at lower speeds they travel at a constant multiple of the local surface speed, measured as 0.76. These travelling disturbances have not been observed on either the rotating disk (see Kohama (1984b), for example) or the rotating cone (see Kobayashi *et al.* (1987), for example); in both cases the positions of the vortices appear fixed relative to the rotating surface, as they would be expected to appear on surfaces where some elements of roughness exist.

The stability of the rotating-cone boundary layer is also the subject of some research, with experimental work by Kappesser *et al.* (1973), Kobayashi & Izumi (1983), for example, and later theoretical work by, among others, Hussain (2010), Garrett & Peake (2007), Garrett *et al.* (2009a) and Garrett (2010a). As a cone's half-angle approaches  $90^\circ$ , it approaches the case of a flat disk, and in this way the three types of boundary layer - disks, cones and spheres - are closely related.

In his thesis, Garrett (2002) performs a stability analysis on both spheres and cones, subject to axial flow, and examines the relationship between theoretical instabilities and the transition to turbulence. His work relating to spheres has since been elaborated on and published as Garrett & Peake (2002, 2004), Samad & Garrett (2009, 2010, 2013). In particular, Garrett demonstrates the presence of local convective and absolute instabilities within the rotating sphere boundary layer and is able to associate these predictions with the experimental observations reported above, including the observation of a constant local Reynolds number at the onset of turbulence at low to moderate latitudes. Garrett also demonstrates the relationship between the rotating-sphere flow close the pole and the rotating-disk flow mathematically by a comparison of the leading order expressions arising from Banks's original series solution. Furthermore, Garrett (2010a) explains Kobayashi & Arai's observation of slow vortices over the sphere through a consideration of relative growth rates of convective instability modes. Garrett has since predicted similar slow vortices on highly-polished rotating bodies of all geometries (Garrett (2010a,b, 2011), Samad &

Garrett (2013)).

The motivation for the work presented here is in its applicability to problems in engineering, such as the flow over spinning projectiles and aero-engine components. In such situations, it may be useful to be able to predict where and when a flow becomes unstable, since it may be advantageous to prevent transition to turbulence and maintain laminar flow for reasons of efficiency, or to reduce wear on components. Alternatively, there may be applications in which turbulence is desirable, such as when fluids are to be mixed. Many applications in fluid mechanics have shown that suction can be used as an effective flow-control mechanism, and all studies have shown injection to have the converse effect by destabilising the boundary layer to all instability types. It is therefore useful to include the parameters of suction (or injection) and axial flow in this work, and to understand how they affect flow stability.

The effect of axial flow on the stability of flow over rotating bodies has received some limited attention. In the case of the rotating disk, Hussain *et al.* (2011) examine theoretically the effects of axial flow, and find it to increase the critical Reynolds number for the onset of convective stability. Both theoretical (Garrett *et al.* (2009)) and experimental (Salzberg & Kezios (1965), Kobayashi *et al.* (1983), Kohama (1984a)) work on rotating cones has found axial flow to delay the onset of convective and absolute instability types. For the rotating sphere, notable studies incorporating axial flow include experimental work by Kobayashi & Arai (1990), and later theoretical work by Garrett (2002, 2010c).

With regard to the literature on surface mass-flux, Lingwood & Garrett (2011) have calculated theoretical critical Reynolds numbers and disturbance growth rates for the general class of rotating “Bödewadt, Ekman and von Kármán” (BEK) flows, subject to surface suction. Stuart (1954) performs early theoretical work on the effects of surface suction on the rotating-disk boundary layer, and finds increased suction to decrease the radial velocity component of the flow, the dominant factor in the onset of the cross flow instability. Gregory & Walker (1960) study this

experimentally and find suction to increase the critical Reynolds number, delaying the onset of instability. Lingwood (1997c) performs theoretical work in this area; her results predict that suction delays the onset of instability and that injection promotes it - though injection is found to be less destabilising than suction is stabilising. Other literature concerned with mass flux on the rotating disk, using various numerical and asymptotic approaches, includes Ockendon (1972), Dhanak (1992), Bassom & Seddougui (1992). Suction is universally found to be stabilising.

In this thesis, research is conducted into the effects of both axial flow and mass flux (distributed suction or injection of fluid through the surface), on the stability of the laminar boundary-layer flow around a rotating sphere. Throughout this work, perturbations to the steady flow are assumed to be small enough so that nonlinear effects are negligible and a linear stability analysis can be used. We follow Garrett and use a NAG routine to solve the governing partial differential equations (PDEs) for the steady flow and incorporate similar numerical methods to solve the governing, unsteady perturbation equations. In addition, both the sphere and the surrounding fluid are assigned distinct uniform temperatures, and the thermal boundary layer is analysed for fluids with various Prandtl numbers. Jain & Venkataraman (1966) analyse a similar system using a series-solution method; the approach we take will use the same numerical method used for calculating the velocity components. Following Lingwood's and Garrett's various publications, a parallel-flow approximation is made throughout (this is described in more detail in Chapter 5), and the fluid is assumed to be incompressible. The research presented in this thesis effectively extends the work of Garrett (2002), who accounts for axial flow but not mass flux and has, so far, been concerned only by local stability analyses over the sphere. In some respects, this work can be considered as the final stage in the study of incompressible, rotating fluids of this type, and the effects of compressibility are now starting to be included in parallel studies on the cone and sphere at Leicester (Towers & Garrett (2012)).

The presentation of a *global* stability analysis in Chapters 8 and 9 of this thesis is a

major step forward and builds on previous work on the local absolute instability of the boundary layer.

In the study of boundary-layer stability on rotating bodies of revolution, a significant advance has been made by Lingwood (1995a), who showed that the boundary layer on a rotating disk of infinite extent is locally absolutely unstable at Reynolds numbers in excess of a critical value (equivalent to being outside a critical radius at fixed rotation rate), and is at worst convectively unstable inside this radius. The value of the critical Reynolds number agrees exceedingly well with experimentally measured values of the transition Reynolds number, leading to Lingwood's hypothesis that absolute instability plays a role in turbulent transition on the disk. By experimentally tracking the wavepacket response to an impulse excitation on a rotating disk, Lingwood (1996) confirmed the presence of absolute instability above a fixed, critical Reynolds number very close to that predicted for the onset of local absolute instability, thereby adding weight to her assertion.

A few years later, Davies & Carpenter (2003) performed direct numerical simulations solving the linearised Navier-Stokes equations directly on a disk of infinite extent. When they made the same homogeneous-flow approximation, i.e. parallel-flow approximation, as in Lingwood's analysis, they recovered her results in full, with absolute instability clearly present at high Reynolds numbers. However, when the spatial inhomogeneity of the boundary layer was included there was no evidence that absolute instability gives rise to an unstable global oscillator in the long-time response that would be required to give the onset of transition within a purely linear theory. Indeed their study suggests that convective behaviour eventually dominates at all the Reynolds numbers investigated, even for strongly absolutely unstable regions, thereby suggesting that absolute instability was not involved in the transition process through linear effects.

Following this, Pier (2003) demonstrated that a nonlinear approach is required to explain the self-sustained behaviour of the rotating-disk flow. Using the result of Huerre & Monkewitz (1990) that the presence of local absolute instability does

not necessarily give rise to linear global instability, Pier suggested that the flow has a primary nonlinear global mode that is fixed by the onset of the local absolute instability which has a secondary absolute instability that triggers the transition to turbulence. Some experimental evidence for a secondary instability exists (Kohama (1984b) and Imayama *et al.* (2012)), but the behaviour of the secondary instability and also its relation to the primary absolute instability are not fully understood as of yet.

In an attempt to explain Lingwood’s original experimental observations in the light of the subsequent theoretical developments, Healey (2010) presented a theory, based on the Ginzburg-Landau equation, that suggests that there can be a linear global instability when there is local instability at the *edge* of the disk. The finite size of experimental disks is of course a crucial difference between experimental and theoretical studies prior to Healey’s work, and edge effects were a new addition to the arguments in the literature. The very recent experimental study of Imayama *et al.* (2013) finds that edge effects may indeed lead to linear global instability as a first step in the onset of transition. The literature continues to develop a theory of transition over the rotating disk.

The spherical geometry is such that neither experimental nor theoretical studies suffer from edge effects. In this study we consider the linear global modes of the rotating-sphere system, as formulated for weakly nonparallel shear flow by Monke-witz *et al.* (1993). The idea is to use data from the local absolute stability analysis of Garrett & Peake (2002) and the work in Chapters 5–7 of this thesis to construct solutions for the entire flow with single complex frequency  $\gamma_G$ . The long-time re-sponse of the system is then governed by  $\text{Im}(\gamma_G)$  and will be linearly *globally stable* if  $\text{Im}(\gamma_G) < 0$  and *globally unstable* if  $\text{Im}(\gamma_G) > 0$ . The approach taken in Chapters 8 and 9 is to attempt to determine  $\gamma_G$  for the rotating sphere flow.

As demonstrated by Lingwood (1995a) and Garrett & Peake (2002), the absolute instability under consideration in both the local and global analyses presented here exists as a result of inviscid effects. However, Healey (2004) suggests pinch points

resulting from an inviscid formulation (i.e. from the solution of the Rayleigh equation) are in fact distinct from those that exist in a viscous formulation (i.e. from the solution of an Orr-Sommerfeld-type equation). With this in mind, we work with the viscous formulation throughout.

The thesis is presented as follows. Chapters 2–4 are concerned with calculating the basic laminar velocity and temperature profiles. The PDEs that govern the steady flow are derived, and they are generalised to allow for the effects of axial flow and distributed surface suction or injection. In later chapters linear stability analyses on these steady profiles are performed. Chapter 5 deals with convective instability, with §§5.1 and 5.2 concerned with the formulation of perturbation equations and the explanation of the solution method. We then present and discuss the results, assuming stationary disturbances in §5.3, and allowing for non-stationary disturbances in §5.4. Critical Reynolds numbers are calculated for the predicted onset of convective instability, and neutral-stability curves are presented. We also consider the predicted number and angle of spiral vortices, which are experimentally observable quantities. In Chapter 6 the spatial growth rates of the disturbances are considered in order to establish the dominant instability mechanism under various conditions. In Chapter 7 we calculate critical parameters for the occurrence of local absolute instability. Chapters 8 and 9 explain the global linear stability analysis. In Chapter 8 we revert to the still-fluid case and reformulate the problem, and in Chapter 9, we reintroduce the control parameters of axial flow and mass injection. In each case, predicted critical Reynolds numbers are presented. Finally, in Chapter 10, we draw conclusions from the results obtained, and discuss their relevance to engineering applications.

Chapters 2–7 have been published as Barrow & Garrett (2013), and Chapter 8 forms the basis for Barrow *et al.* (2013), which is currently in preparation.

## 1.2 Stability theory

This thesis is concerned with the application of stability theory to flows of practical significance. Given the applied nature of the flows, the thesis is presented in a manner consistent with the intended readership and is not overly mathematical. However, for completeness, we summarise the fundamental mathematics of stability theory here. Much of this theory was originally developed in the field of plasma physics by Briggs (1964) and Bers (1972). We include the formal definitions of local and global instability and the criteria that determine whether an unstable flow is convectively or absolutely unstable. For a more thorough treatment of this topic, Huerre & Monkewitz (1990) give an extensive review, and the theory is also covered by Crighton & Gaster (1976), Bers (1984), Thomas (2007), among many others.

### 1.2.1 Local stability

Given a steady open flow whose streamwise velocity component is given by  $U(y, R)$ , where  $y$  is the cross-stream spatial coordinate, and  $R$  is a set of control parameters, we can characterise its reaction to an initial infinitesimal disturbance at time  $t = 0$  by the general dispersion relation,

$$D(\alpha, \gamma, R) = 0. \tag{1.1}$$

Here,  $\alpha$  and  $\gamma$  are the streamwise wavenumber and the frequency of the disturbance, respectively. By defining  $U$  without a dependence on the streamwise spatial coordinate,  $x$ , we are assuming that the steady mean-velocity profile is independent of streamwise location (the parallel-flow assumption), and this means we are studying local instabilities. The quantities  $\alpha$  and  $\gamma$  are, in general, complex. Solutions of (1.1) where  $\alpha(\gamma)$  is considered a complex function of real  $\gamma$  are called spatial branches, while solutions where  $\gamma(\alpha)$  is considered a complex function of real  $\alpha$  are called temporal modes. Here we will ignore cross-stream variation in the disturbance,  $\psi(x, t)$ , and simply analyse its evolution in the  $(x, t)$  plane. We then associate  $D$  with a

differential operator such that

$$D \left[ -i \frac{\partial}{\partial x}, i \frac{\partial}{\partial t}; R \right] \psi(x, t) = 0, \quad (1.2)$$

allowing an analysis of the system's behaviour in physical space and time (see Huerre & Monkewitz (1990)). The response to the disturbance is characterised by the Green's function,  $G(x, t)$ , for the operator  $D$ , such that

$$D \left[ -i \frac{\partial}{\partial x}, i \frac{\partial}{\partial t}; R \right] G(x, t) = \delta(x)\delta(t), \quad (1.3)$$

where  $\delta$  is the Dirac delta function. Physically, this corresponds to a disturbance introduced at  $t = x = 0$ . We can now state the conditions for linear stability: the flow is stable if

$$\lim_{t \rightarrow \infty} G(x, t) = 0 \text{ along all rays } x/t = \text{constant}, \quad (1.4)$$

and it is unstable if

$$\lim_{t \rightarrow \infty} G(x, t) = \infty \text{ along at least one ray } x/t = \text{constant}. \quad (1.5)$$

If the flow is unstable, it can be further classified as to its type: the flow is *convectively* unstable if

$$\lim_{t \rightarrow \infty} G(x, t) = 0 \text{ along the ray } x/t = 0,$$

and it is *absolutely* unstable if

$$\lim_{t \rightarrow \infty} G(x, t) = \infty \text{ along the ray } x/t = 0.$$

Figure 1.2 illustrates the physical distinction between convective instability (a.) and absolute instability (b.). As time progresses, the disturbance grows in the regions between the dashed rays.

By examining the structure of the dispersion relation, we can deduce general

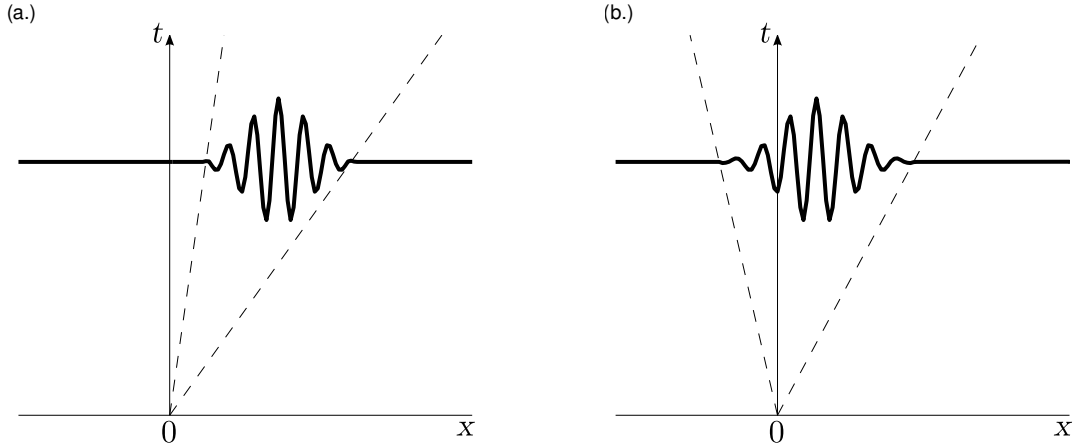


Figure 1.2: Illustration of convective and absolute instabilities. A point disturbance at  $t = 0$  creates a travelling wave. As it moves forward in time, it may convect downstream and away from the source position (convective instability, (a.)) or spread upstream of the initial disturbance, eventually polluting all spatial points in the flow (absolute instability, (b.)).

criteria for distinguishing between convective and absolute instability. The Green's function,  $G$ , can be recast into Fourier-Laplace space by expressing it as the double integral,

$$G(x, t) = \frac{1}{(2\pi)^2} \int_F \int_L \frac{e^{i(\alpha x - \gamma t)}}{D[\alpha, \gamma; R]} d\gamma d\alpha, \quad (1.6)$$

where  $F$  and  $L$  are the integration contours for the Fourier and Laplace transforms, respectively. At time  $t = 0$ , the contour  $L$  is a horizontal line in the complex- $\gamma$  plane; it must be positioned above all singularities of the integrand to satisfy causality, since by assumption the flow is steady before the disturbance is introduced. The  $F$  contour initially lies along the real axis in the complex- $\alpha$  plane. Figures 1.3 (a.) and (b.) show the initial locations of the integration contours in the complex- $\gamma$  plane and the complex- $\alpha$  plane, respectively. These figures also show the forms typically taken by the spatial branches and temporal modes. Note that it is assumed that there are two spatial branches,  $\alpha^+(\gamma)$  and  $\alpha^-(\gamma)$ , corresponding to effects downstream and upstream of the initial disturbance, respectively. In finding the time-asymptotic solution of (1.6) these contours will be deformed using analytic continuation, until a singularity is encountered.

The Green's function defined by (1.6) takes the form of a disturbance wavepacket in the  $(x, t)$ -plane, with the response along each ray  $x/t$  dominated by a single

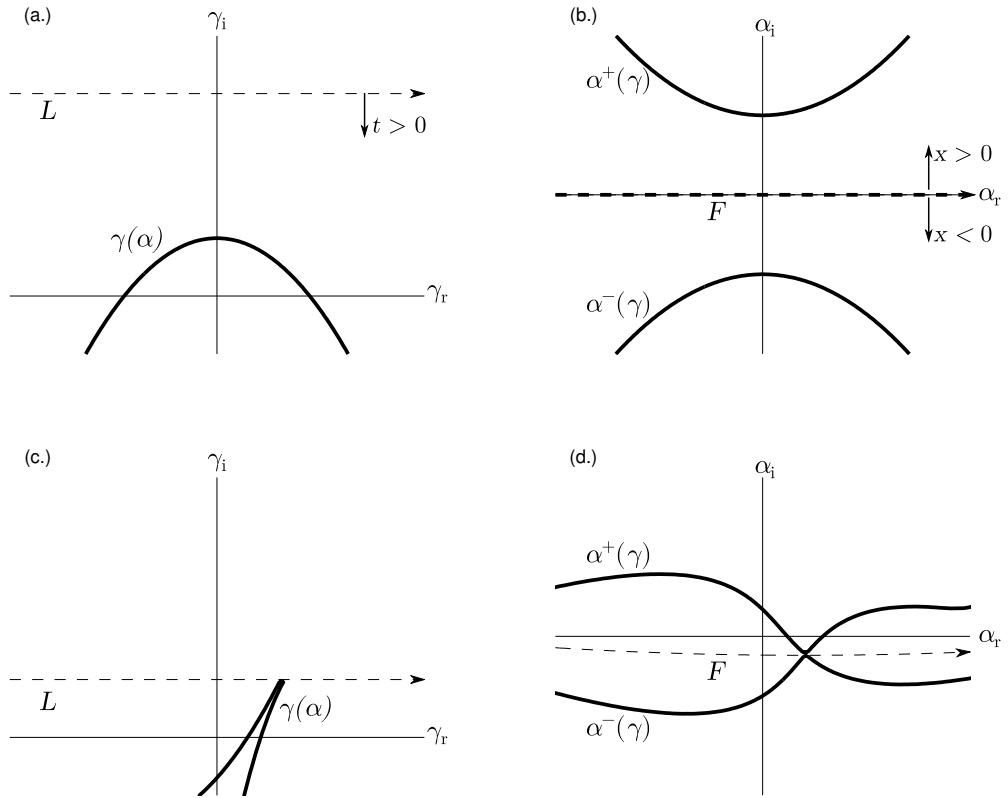


Figure 1.3: Illustration of the contours of integration.

complex wavenumber,  $\alpha_*$ , such that  $\partial\gamma/\partial\alpha(\alpha_*) = x/t$ . The temporal growth rate along each ray is then given by  $\gamma_i(\alpha_*) - (x/t)\alpha_{*i}$ . Within a temporal mode,  $\gamma(\alpha)$ , where  $\alpha$  is real, the growth rate reduces to  $\gamma_i(\alpha_*)$ . The maximum growth rate,  $\gamma_{i,\max}$ , is then found at the stationary point,  $\partial\gamma_i/\partial\alpha = 0$ .

From (1.4) and (1.5), we can now derive more simple criteria for linear stability: the flow is linearly stable when  $\gamma_{i,\max} < 0$ , and it is linearly unstable when  $\gamma_{i,\max} > 0$ .

By considering the dominant wavenumber along the ray  $x/t = 0$  at a fixed spatial location, we can also derive criteria for the convective/absolute nature of the instability. This complex wavenumber,  $\alpha_0$ , has zero group velocity by definition:

$$\frac{\partial\gamma}{\partial\alpha}(\alpha_0) = 0. \quad (1.7)$$

The frequency corresponding to this wavenumber is given by  $\gamma_0 = \gamma(\alpha_0)$ , and is referred to as the absolute frequency. Typically,  $\alpha_0$  is a saddle point of  $\gamma$  in the complex- $\alpha$  plane. The absolute growth rate is then given by the imaginary part of

the absolute frequency,  $\gamma_{0,i}$ , and it is the sign of this quantity that determines the long-time response. If  $\gamma_{0,i} < 0$ , the flow is convectively unstable; if  $\gamma_{0,i} > 0$ , the flow is absolutely unstable.

However, although it is necessary for (1.7) to be satisfied with positive  $\gamma_{0,i}$ , these criteria alone are insufficient to identify absolute instability. The Briggs-Bers method (see Briggs (1964) and Bers (1972)) allows an asymptotic examination of the long-time behaviour of the disturbance: if we let

$$\bar{G}(x, \gamma) = \frac{1}{2\pi} \int_F \frac{e^{i\alpha x}}{D(\alpha, \gamma; R)} d\alpha, \quad (1.8)$$

then by rearranging (1.6), we can write

$$G(x, t) = \frac{1}{2\pi} \int_L \bar{G}(x, \gamma) e^{-i\gamma t} d\gamma. \quad (1.9)$$

As  $t$  increases, we can lower the  $L$  contour. As  $L$  is lowered, the relationship between  $\alpha$  and  $\gamma$  enforced by the dispersion relation means that the two spatial branches,  $\alpha^+$  and  $\alpha^-$ , deform towards each other. The  $F$  contour must be lowered to keep them confined to separate halves of the complex- $\alpha$  plane. At some point, however, the spatial branches will meet, and here  $F$  will become pinched between the two. This “pinch point” prevents us from progressing any further with the lowering of  $L$ . If, at the pinch point,  $L$  remains above the real- $\gamma$  axis, then absolute instability will occur due to the growth of the exponential term in (1.9) as  $t \rightarrow \infty$ . If  $L$  has moved below the real axis, this term will decay, and if there is instability, it is convective at worst. Figures 1.3 (c.) and (d.) show the positions of the contours as they reach a pinch point. In this example, the flow is absolutely unstable.

### 1.2.2 Global stability

Section 1.2.1 describes the process of identifying convective and absolute instabilities assuming that the steady-flow velocity profiles are locally invariant in the streamwise direction. However, it is often more insightful to analyse the behaviour at a global

scale, and to do this it is necessary to overcome the parallel-flow approximation used in the local analyses.

In order to relate the local to the global stability properties of the flow, we require that the velocity,  $U$ , changes over a slow spatial scale in the streamwise direction, so that the flow is weakly non-parallel (see Monkewitz *et al.*, 1993). To this end, we introduce  $X = \varepsilon x$ , where  $\varepsilon \ll 1$  is a small scaling factor.

We redefine the dispersion relation,  $D$ , and the perturbation response,  $\Psi$ , such that they satisfy

$$D \left[ -i \frac{\partial}{\partial x}, i \frac{\partial}{\partial t}; R, X \right] \Psi = 0,$$

and we now seek  $\Psi$  of the form

$$\Psi(x, t; X) = \psi^\pm(x; X) e^{-i\gamma_G t}, \quad (1.10)$$

where  $\psi^+$  and  $\psi^-$  represent the response downstream and upstream of the source, respectively, and take the form

$$\psi^\pm(x; X) \sim A^\pm(X) \exp \left( \frac{i}{\varepsilon} \int^X \alpha^\pm(X; \gamma) dX \right).$$

Here,  $A^+$  and  $A^-$  represent the complex amplitude of the initial disturbance for  $x > 0$  and  $x < 0$ , respectively. The global behaviour of the flow is governed by the single complex frequency,  $\gamma_G$ . Global stability then depends on the growth-rate of this quantity,  $\gamma_{G,i}$ . The flow is said to be *globally stable* if  $\gamma_{G,i} < 0$ , and *globally unstable* if  $\gamma_{G,i} > 0$ .

### Formulation of the global mode

As in §1.2.1, the local absolute frequency,  $\gamma_0$ , is the value of  $\gamma$  at a point along the ray  $x/t = 0$ , satisfying:

$$\frac{\partial \gamma}{\partial \alpha}(\alpha, X) = 0, \quad (1.11)$$

and the value of  $\alpha$  at this stationary point is  $\alpha_0$ . The local absolute growth rate is the imaginary part of the absolute frequency, denoted by  $\gamma_{0,i}$ .

The local maximum growth rate,  $\gamma_{i,\max}$ , is the value of  $\gamma_i$  which satisfies:

$$\frac{\partial \gamma_i}{\partial \alpha}(\alpha, X) = 0.$$

For global instability to exist, it is required that there exists a region of local absolute instability, where  $\gamma_{0,i} > 0$ . This necessarily means that  $\gamma_{i,\max} > 0$ , since the value of the local absolute growth rate can never exceed that of the local maximum growth rate.

Having located points with zero group velocity, as per (1.11), we now seek a point with the additional criterion that

$$\frac{\partial \gamma}{\partial X}(\alpha, X) = 0. \quad (1.12)$$

The symbols  $\alpha_s$  and  $X_s$  are used respectively to refer to the values of  $\alpha$  and  $X$  at such a point, and typically, both are complex quantities.

We then proceed in a manner similar to that of §1.2.1. In the global case, we examine the long-time behaviour of the Green's function for the differential operator,  $D$ :

$$D \left[ -i \frac{\partial}{\partial x}, i \frac{\partial}{\partial t}; R, X \right] G(x, t) = \delta(x) \delta(t),$$

The Green's function is defined as

$$G(x, t) = \frac{1}{2\pi} \int_L \bar{G}(x, \gamma) e^{-i\gamma t} d\gamma, \quad (1.13)$$

where

$$\bar{G}(x; \gamma) \sim A^\pm(X) \exp \left( \frac{i}{\epsilon} \int^X \alpha^\pm(X; \gamma) dX \right). \quad (1.14)$$

$L$  is a horizontal line in the complex- $\gamma$  plane, which initially lies above all singularities in  $\gamma_0(X)$ .  $F$  initially lies on the real  $X$  axis. As time progresses, these contours are

deformed until a second pinch point is reached. Here, the superscripts + and – refer to effects downstream and upstream of the disturbance, respectively.

The global mode is then defined as the value of  $\gamma$  at this double pinch-point, where both (1.11) and (1.12) hold:

$$\gamma_G = \gamma(\alpha_s, X_s).$$

The above mathematics underpins much of what follows. The reader is referred back to this section as appropriate.

# Chapter 2

## Incompressible boundary-layer flow over a rotating sphere

In this chapter, the case of a sphere rotating within still fluid is considered. The effects of heating, mass-flux and axial flow will be the subject of later chapters; however, it is illustrative to consider the still-fluid case in the first instance. The work presented here is based on the description given in Chapter 2 of Garrett (2002) and also Garrett & Peake (2002) and is, in part, based on the previous work of Howarth (1951), Banks (1965), Manohar (1967), Banks (1976). In §2.1 we formulate the problem and derive the governing set of PDEs and the appropriate boundary conditions. In §2.2 this system is solved and the resulting profiles discussed.

### 2.1 Formulation and governing equations

Incompressible fluid flow is governed by the Navier-Stokes equations:

$$\frac{D\mathbf{u}^*}{Dt} = -\frac{1}{\rho}\nabla P^* + \nu^*\nabla^2\mathbf{u},$$
$$\nabla \cdot \mathbf{u}^* = 0.$$

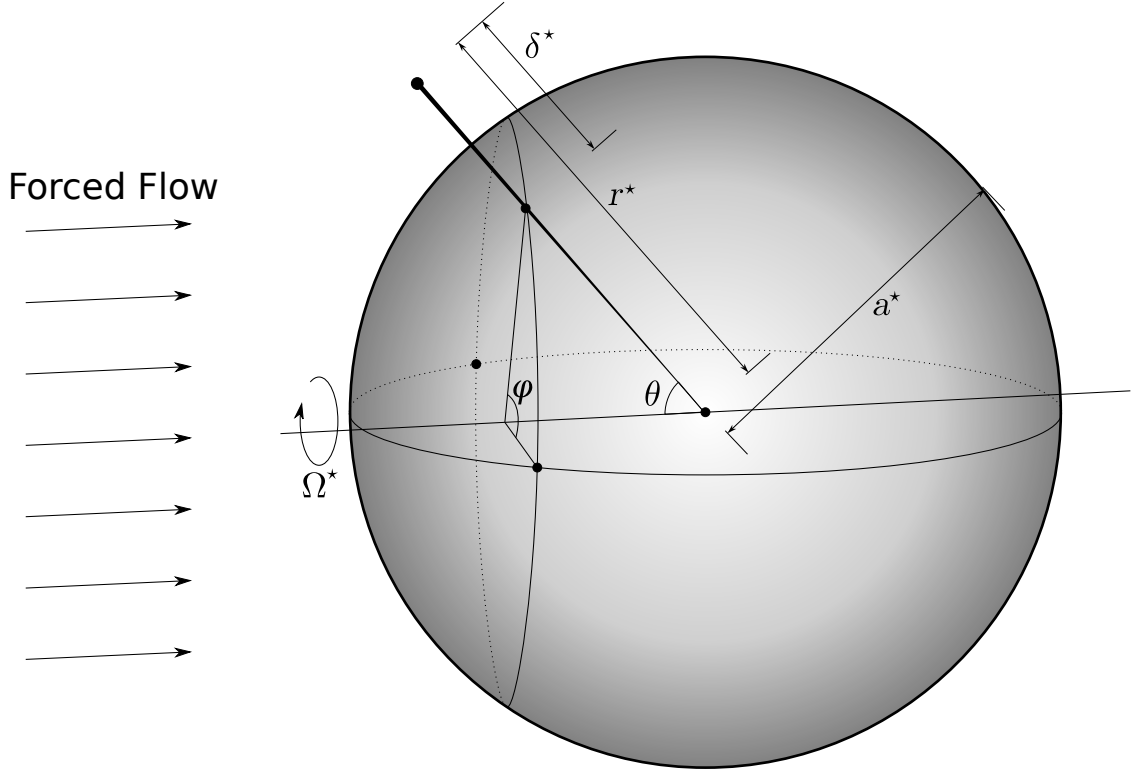


Figure 2.1: Illustration of the coordinate system used throughout this work.

Since we are studying flow over a sphere, it will be convenient to express these equations in spherical coordinates, as follows.

$$\begin{aligned} \frac{\partial W^*}{\partial t^*} + (\mathbf{u}^* \cdot \nabla) W^* - \frac{U^{*2}}{r^*} - \frac{V^{*2}}{r^*} = \\ -\frac{1}{\rho} \frac{\partial P^*}{\partial r^*} + \nu^* \left[ \nabla^2 W^* - \frac{2W^*}{r^{*2}} - \frac{2}{r^{*2} \sin \theta} \frac{\partial}{\partial \theta} (U^* \sin \theta) - \frac{2}{r^{*2} \sin \theta} \frac{\partial V^*}{\partial \phi} \right], \end{aligned}$$

$$\begin{aligned} \frac{\partial U^*}{\partial t^*} + (\mathbf{u}^* \cdot \nabla) U^* + \frac{W^* U^*}{r^*} - \frac{V^{*2} \cot \theta}{r^*} = \\ -\frac{1}{\rho r^*} \frac{\partial P^*}{\partial \theta} + \nu^* \left[ \nabla^2 U^* + \frac{2}{r^{*2}} \frac{\partial W^*}{\partial \theta} - \frac{U^*}{r^{*2} \sin^2 \theta} - \frac{2 \cos \theta}{r^{*2} \sin^2 \theta} \frac{\partial V^*}{\partial \phi} \right], \end{aligned}$$

$$\begin{aligned} \frac{\partial V^*}{\partial t^*} + (\mathbf{u}^* \cdot \nabla) V^* + \frac{V^* W^*}{r^*} + \frac{U^* V^* \cot \theta}{r^*} = \\ -\frac{1}{\rho r^* \sin \theta} \frac{\partial P^*}{\partial \phi} + \nu^* \left[ \nabla^2 V^* + \frac{2}{r^{*2} \sin \theta} \frac{\partial W^*}{\partial \phi} + \frac{2 \cos \theta}{r^{*2} \sin^2 \theta} \frac{\partial U^*}{\partial \phi} - \frac{V^*}{r^{*2} \sin^2 \theta} \right], \end{aligned}$$

where  $r^*$  is the radial distance from the centre of the sphere,  $\theta$  is the angle of latitude measured from the pole, and  $\phi$  is the angle of azimuth measured from some fixed plane parallel to the axis of rotation.  $U^*$ ,  $V^*$  and  $W^*$  are the components of  $\mathbf{u}^*$ , the steady-flow vector, in the directions  $\theta$ ,  $\phi$  and  $r^*$  respectively;  $\nu^*$  is the kinematic viscosity, and  $P^*$  is pressure. Note that  $*$  indicates a dimensional quantity.

The sphere is considered to rotate within a fixed frame of reference, with angular velocity  $\Omega^*$  (see Figure 2.1). Due to this frame of reference, terms representing Coriolis forces do not occur in the governing equations. On the boundary of the sphere,  $r^* = a^*$ , the no-slip condition applies. Also, by assumption, motion in the fluid is caused only by the motion of the sphere, leading to a quiescent fluid condition in the far field; hence

$$\begin{aligned} U^* = W^* = V^* - a^*\Omega^* \sin \theta = 0 & \quad \text{on } r^* = a^*, \\ U^* = V^* = 0 & \quad \text{as } r^* \rightarrow \infty. \end{aligned} \tag{2.1}$$

These give the boundary conditions on the surface of the sphere and in the far field, respectively.

The Navier-Stokes equations can be simplified by making the additional boundary-layer assumptions that

$$\begin{aligned} W^* &\sim O(\delta^*), \quad U^* \sim O(1), \\ V^* &\sim O(1), \quad \frac{\partial}{\partial \theta} \sim O(1), \end{aligned}$$

where  $\delta^*$  is the boundary-layer thickness, given by

$$\delta^* = \left( \frac{\nu^*}{\Omega^*} \right)^{\frac{1}{2}} \ll 1,$$

Making these assumptions, and neglecting azimuthal variation, which reflects the

rotational symmetry of system, leads to the equations

$$W^* \frac{\partial U^*}{\partial r^*} + \frac{U^*}{a^*} \frac{\partial U^*}{\partial \theta} - \frac{V^{*2}}{a^*} \cot \theta = \nu^* \frac{\partial^2 U^*}{\partial r^{*2}}, \quad (2.2)$$

$$W^* \frac{\partial V^*}{\partial r^*} + \frac{U^*}{a^*} \frac{\partial V^*}{\partial \theta} + \frac{U^* V^*}{a^*} \cot \theta = \nu^* \frac{\partial^2 V^*}{\partial r^{*2}}, \quad (2.3)$$

$$\frac{\partial W^*}{\partial r^*} + \frac{1}{a^*} \frac{\partial U^*}{\partial \theta} + \frac{U^*}{a^*} \cot \theta = 0. \quad (2.4)$$

We note that these are identical to those listed in the literature.

Equations (2.2)–(2.4) can be non-dimensionalised by introducing the following non-dimensional variables:

$$U(\eta, \theta) = \frac{U^*}{\Omega^* a^*}, \quad V(\eta, \theta) = \frac{V^*}{\Omega^* a^*}, \quad W(\eta, \theta) = \frac{W^*}{(\nu^* \Omega^*)^{1/2}},$$

with  $\eta = \left(\frac{\Omega^*}{\nu^*}\right)^{\frac{1}{2}} (r^* - a^*)$  being the non-dimensional distance from the surface of the sphere, non-dimensionalised on the boundary-layer thickness. This gives

$$W \frac{\partial U}{\partial \eta} + U \frac{\partial U}{\partial \theta} - V^2 \cot \theta = \frac{\partial^2 U}{\partial \eta^2}, \quad (2.5)$$

$$W \frac{\partial V}{\partial \eta} + U \frac{\partial V}{\partial \theta} + UV \cot \theta = \frac{\partial^2 V}{\partial \eta^2}, \quad (2.6)$$

$$\frac{\partial W}{\partial \eta} + \frac{\partial U}{\partial \theta} + U \cot \theta = 0. \quad (2.7)$$

Note that the latitudinal and azimuthal velocities are scaled on the equatorial surface speed of the sphere.

Using the same scalings, the boundary conditions (2.1) become

$$\begin{aligned} U = W = V - \sin \theta = 0 & \quad \text{on } \eta = 0, \\ U = V = 0 & \quad \text{as } \eta \rightarrow \infty. \end{aligned} \quad (2.8)$$

## 2.2 Obtaining the steady flow

The system of PDEs (2.5)–(2.7) subject to conditions (2.8) governs the scaled steady flow within the rotating-sphere boundary layer. It is now necessary to solve this

system in order to study the properties of the flow. As discussed in Chapter 1, the solution at each latitude can be obtained from approximate series-solution methods as used by Banks (1965) and Jain & Venkataraman (1966), or accurate numerical methods; see Manohar (1967), Banks (1976), Garrett (2002) and Garrett & Peake (2002). We choose to follow Garrett (2002), Garrett & Peake (2002) and use the routine, D03PEF, commercially available from the Numerical Algorithms Group. However, in order to implement this we first require a complete initial solution at a low latitude ( $\theta = 1^\circ$  in this work), which we obtain from the series solution of Banks (1965).

We begin by summarising the series-solution method in §2.2.1, before proceeding to obtain the full solution in §2.2.2. In addition, we will discuss the implications of using the series solution over the entire sphere.

### 2.2.1 A series-solution method

Two series-solution methods have been considered. The first and more accurate of these, originally proposed by Howarth (1951) and later used by Banks (1965), is considered in detail here. The second, by Jain & Venkataraman (1966), assumes a series solution in both  $\theta$  and  $\eta$ , and will be shown to be very inaccurate in §2.2.3.

Banks's method is to express each of  $U$ ,  $V$ , and  $W$  as a series expansion in powers of  $\theta$ ;

$$U = F_1\theta + F_3\theta^3 + \dots, \quad (2.9)$$

$$V = G_1\theta + G_3\theta^3 + \dots, \quad (2.10)$$

$$W = H_1 + H_3\theta^2 + \dots, \quad (2.11)$$

where  $F_i$ ,  $G_i$ , and  $H_i$  are non-dimensional functions of  $\eta$ , and  $i = 1, 3, 5, \dots$ . By applying the boundary conditions from (2.8), and equating coefficients of each power

of  $\theta$ , we obtain

$$F_i(0) = H_i(0) = G_i(0) - \frac{1}{i!}(-1)^{\frac{i-1}{2}} = 0, \quad (2.12)$$

$$F_i(\infty) = G_i(\infty) = 0. \quad (2.13)$$

Substituting the expansions (2.9)–(2.11) into (2.5), after changing to the spatial variable  $\eta$ , we again equate coefficients of each power of  $\theta$ . At orders one to four, we obtain the following nonlinear ordinary differential equations (ODEs) which govern  $F_i, G_i$  and  $H_i$ , with a prime denoting differentiation with respect to  $\eta$ .

$$H_1 F_1' + F_1^2 - G_1^2 = F_1'', \quad (2.14)$$

$$4F_1 F_3 + H_1 F_3' + H_3 F_1' - 2G_1 G_3 + \frac{G_1^2}{3} = F_3'', \quad (2.15)$$

$$6F_1 F_5 + 3F_3^2 + H_1 F_5' + H_3 F_3' + H_5 F_1' - 2G_1 G_5 - G_3^2 + \frac{2}{3}G_1 G_3 + \frac{1}{45}G_1^2 = F_5'', \quad (2.16)$$

$$8F_1 F_7 + 8F_3 F_5 + H_1 F_7' + H_3 F_5' + H_5 F_3' + H_7 F_1' - 2G_1 G_7 - 2G_3 G_5 + \frac{1}{3}G_3^2 + \frac{2}{3}G_1 G_5 + \frac{2}{45}G_1 G_3 + \frac{2}{945}G_1^2 = F_7''. \quad (2.17)$$

Similarly, substituting into (2.6) and then (2.7) gives

$$2F_1 G_1 + H_1 G_1' = G_1'', \quad (2.18)$$

$$4F_1 G_3 + 2F_3 G_1 + H_1 G_3' + H_3 G_1' - \frac{1}{3}F_1 G_1 = G_3'', \quad (2.19)$$

$$6F_1 G_5 + 4F_3 G_3 + 2F_5 G_1 + H_1 G_5' + H_3 G_3' + H_5 G_1' - \frac{1}{3}F_1 G_3 - \frac{1}{3}F_3 G_1 - \frac{1}{45}F_1 G_1 = G_5'', \quad (2.20)$$

$$8F_1 G_7 + 6F_3 G_5 + 4F_5 G_3 + 2F_7 G_1 + H_1 G_7' + H_3 G_5' + H_5 G_3' + H_7 G_1' - \frac{1}{3}F_1 G_5 - \frac{1}{3}F_3 G_3 - \frac{1}{3}F_5 G_1 - \frac{1}{45}F_1 G_3 - \frac{1}{45}F_3 G_1 - \frac{2}{945}G_1 F_1 = G_7'', \quad (2.21)$$

$$2F_1 + H'_1 = 0, \quad (2.22)$$

$$4F_3 + H'_3 - \frac{1}{3}F_1 = 0, \quad (2.23)$$

$$6F_5 + H'_5 - \frac{1}{45}F_1 - \frac{1}{3}F_3 = 0, \quad (2.24)$$

$$8F_7 + H'_7 - \frac{2}{945}F_1 - \frac{1}{45}F_3 - \frac{1}{3}F_5 = 0. \quad (2.25)$$

The solution to Equations (2.14)–(2.25), subject to the boundary conditions (2.12) and (2.13), is found using a shooting method. Values for  $F'_i(0)$  and  $G'_i(0)$  are initially guessed, and the equations are integrated forwards using a fourth-order Runge-Kutta routine over a suitably large domain. On the outer boundary of the domain of integration, the resulting values of  $F_i$  and  $G_i$  are compared with the boundary condition (2.13). If the values for  $F_i$  and  $G_i$  do not satisfy this to within a predefined tolerance, a Newton-Raphson procedure is used to find better approximations for  $F'_i(0)$  and  $G'_i(0)$ . The integration step is performed again, and the process then repeats until the desired level of precision is reached. This algorithm is based on an amended version of a routine used by Garrett (2002), based on code originally developed by Lingwood (1995a).

The domain of integration used in the shooting method is chosen such that it is large enough so that increasing its size further has very little effect on the values of  $F'_i(0)$  and  $G'_i(0)$ . In this case, the domain is chosen by performing the shooting method several times over domains of increasing size, until further enlargement causes the new values for  $F'_i(0)$  and  $G'_i(0)$  to differ in the sixth decimal place only. It is found that this condition is satisfied upon reaching  $\eta = 20$ , so a domain of  $0 \leq \eta \leq 20$  is considered sufficient.

The series-solution method provides acceptable accuracy for small values of  $\theta$ , i.e. for positions close to the sphere's pole, but this accuracy diminishes with latitude, and it is for this reason that the numerical solution of Garrett (2002), described in §2.2.2, is preferable. As  $\theta$  tends to zero, Equations (2.14)–(2.15) limit to the von Kármán equations for the rotating disk, demonstrating the similarity in the two systems. We will return to this in §2.2.3.

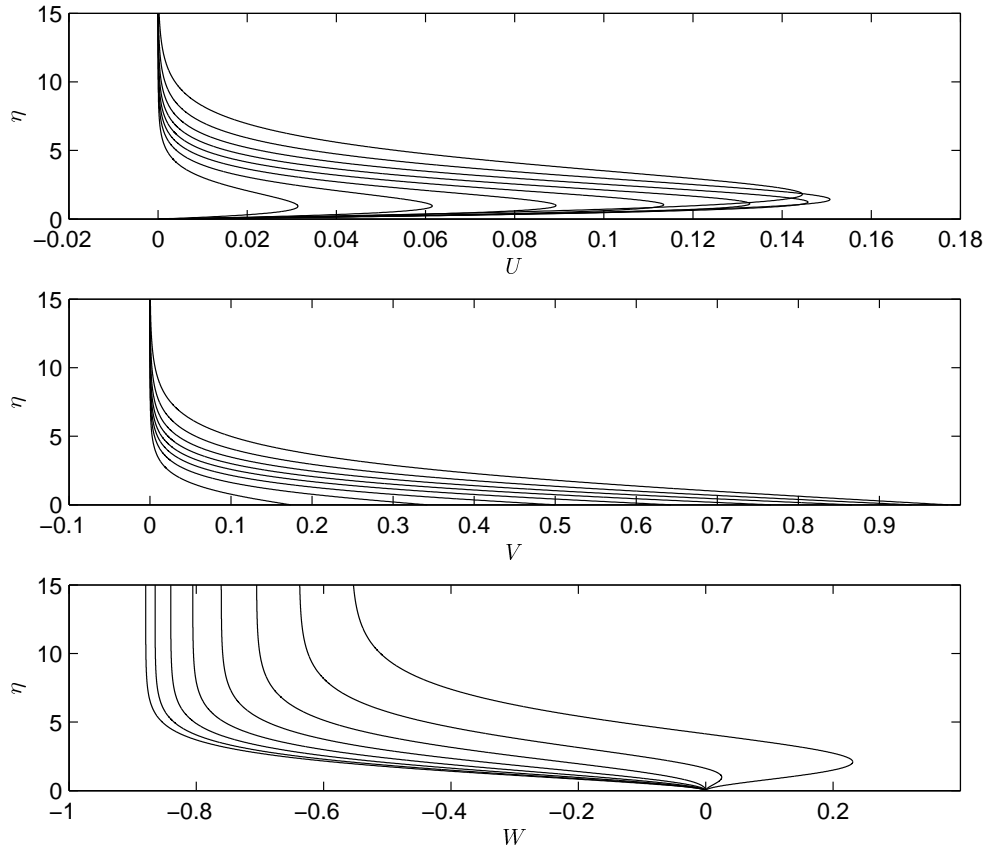


Figure 2.2: Velocity profiles for  $U(\eta)$ ,  $V(\eta)$  and  $W(\eta)$ , each plotted for latitudes of  $10^\circ$  to  $80^\circ$  in increments of  $10^\circ$  (left to right).

## 2.2.2 A full numerical solution

The numerical solution is found using the commercially available NAG routine, D03PEF. This routine is able to integrate a system of first-order PDEs by reducing it to a system of ODEs by using a Keller Box scheme and the method of lines. Starting with a provided complete solution at latitude  $\theta = 1^\circ$ , taken from Banks's series solution method, the NAG routine proceeds to calculate solutions for each one-degree increment of  $\theta$  over the body. Figure 2.2 shows the resultant velocity profiles at selected latitudes. It can be seen that close to the sphere surface, the components  $U$  and  $V$  grow with latitude. The radial component,  $W$ , is negative over most of the sphere, reflecting the fact that fluid is entrained into the boundary layer, but the plots corresponding to latitudes of  $70^\circ$  and  $80^\circ$  indicate a region of reverse flow near the surface. In fact, this reverse flow occurs at latitudes  $63^\circ$  and above.

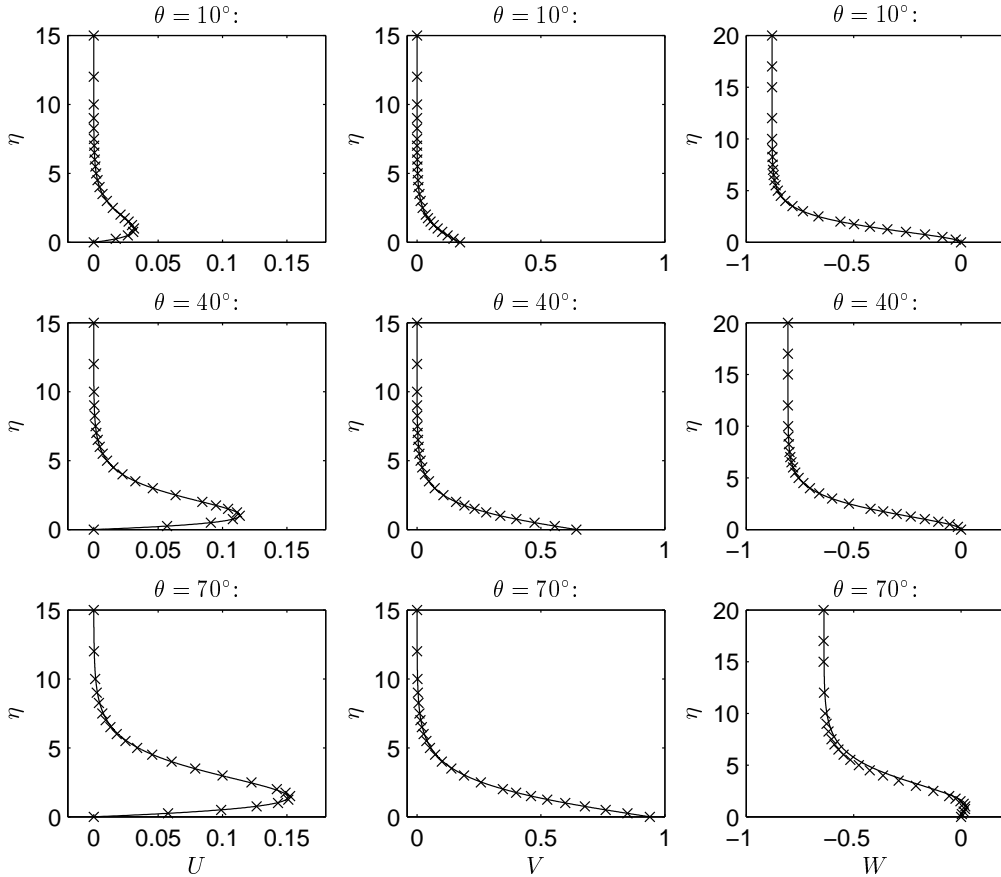


Figure 2.3: Comparison of profiles calculated using the series-solution method of Banks (1965) (crosses) with profiles for the numerical NAG solution (solid line), at  $\theta = 10^\circ, 40^\circ, 70^\circ$ .

### 2.2.3 Analysis of error in the series-solution method

The graphs in Figure 2.3 illustrate the difference between the results obtained by Banks (1965) using the series-solution method and the more accurate numerical method. As expected, the error appears to increase at greater distances from the pole. However, the solutions show close agreement for all  $\eta$  at low latitudes.

Jain & Venkataraman (1966) use a different series-solution method, expressing each component as an expansion in powers of  $\sin \theta$ . This also leads to a system of ODEs, but at increasing orders of  $\sin \theta$ . The resultant ODEs are then solved by assuming expansions in powers of  $\eta$ . Figure 2.4 shows how their results compare with the numerical solution. In this case the error increases with both  $\theta$  and  $\eta$ , which is to be expected from such a series solution. Given the evident inaccuracies shown in Figure 2.4, we will use only the Banks and NAG solutions going forward.

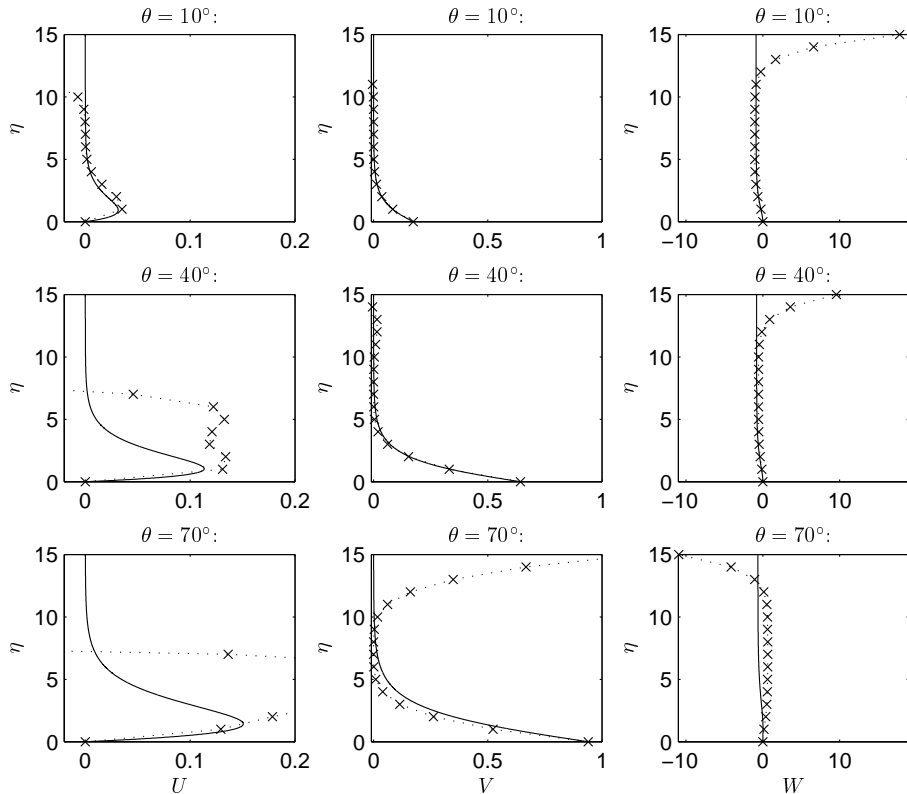


Figure 2.4: Comparison of profiles calculated using the method of Jain & Venkataraman (1966) (crosses) with profiles for the numerical NAG solution (solid line), at  $\theta = 10^\circ, 40^\circ, 70^\circ$ .

## 2.3 Boundary-layer flow over a rotating sphere with heating

In this section we extend the formulation and solution method described in §§2.1 and 2.2 in order to obtain the steady-flow profiles over the rotating sphere for incompressible flow with heating. The Prandtl number of the fluid,  $Pr$ , is a dimensionless number approximating the ratio of momentum diffusivity ( $\nu^*$ ) to thermal diffusivity. Due to the assumption that the fluid is incompressible, heating and cooling have no effect on its density, which remains constant and uniform. This means that velocity profiles are independent of the Prandtl number, and consequently the stability of the flow is not affected. The thermal boundary layer is therefore treated alongside the mean velocity profiles in Chapters 2–4, but it will not be considered further. The results calculated here may form the basis of a future study that allows for a compressible fluid.

In a similar process to that used in §2.2, we first use a series-solution method, before obtaining a numerical solution using the NAG software. The governing equations are again (2.5)–(2.8) with the addition of the energy equation and appropriate boundary conditions. These are stated as

$$W \frac{\partial T^*}{\partial r^*} + \frac{U}{a^*} \frac{\partial T^*}{\partial \theta} = \frac{\nu^*}{\text{Pr}} \frac{\partial^2 T^*}{\partial r^{*2}}, \quad (2.26)$$

$$\begin{aligned} U = W = V - \sin \theta = 0, \quad T^* = T_a^* \quad \text{on } \eta = 0, \\ U = V = 0, \quad T^* = T_\infty^* \quad \text{as } \eta \rightarrow \infty. \end{aligned} \quad (2.27)$$

Here  $T_a^*$  is the surface temperature and  $T_\infty^*$  is the the ambient fluid temperature.

We assume the following expansions, using expressions from Banks (1965) for the velocity components, and for temperature:

$$U^* = a^* \Omega^* (\theta F_1 + \theta^3 F_3 + \dots), \quad (2.28)$$

$$V^* = a^* \Omega^* (\theta G_1 + \theta^3 G_3 + \dots), \quad (2.29)$$

$$W^* = (\nu^* \Omega^*)^{\frac{1}{2}} (H_1 + \theta^2 H_3 + \dots), \quad (2.30)$$

$$T^* = T_a^* + (T_\infty^* - T_a^*) (M_1 + \theta^2 M_3 + \theta^4 M_5 + \dots), \quad (2.31)$$

We obtain the following ODEs at successive orders of  $\theta$ :

$$H_1 M_1' - \frac{M_1''}{\text{Pr}} = 0, \quad (2.32)$$

$$H_1 M_3' + H_3 M_1' + 2F_1 M_3 - \frac{M_3''}{\text{Pr}} = 0, \quad (2.33)$$

$$H_1 M_5' + H_3 M_3' + H_5 M_1' + 4F_1 M_5 + 2F_3 M_3 - \frac{M_5''}{\text{Pr}} = 0, \quad (2.34)$$

$$H_1 M_7' + H_3 M_5' + H_5 M_3' + H_7 M_1' + 6F_1 M_7 + 4F_3 M_5 + 2F_5 M_3 - \frac{M_7''}{\text{Pr}} = 0, \quad (2.35)$$

...

with a prime, as before, denoting differentiation with respect to  $\eta$ . The functions  $F_i$ ,  $G_i$  and  $H_i$  are determined from the equations stated previously, (2.14)–(2.25).

The functions  $M_i$  are subject to boundary conditions,

$$M_i(0) = 0 \tag{2.36}$$

$$M_i(\infty) = 0 \tag{2.37}$$

We use a shooting method to determine the initial conditions for this system of equations for each of several values for  $Pr$ , then evaluate them computationally. Figure 2.5 is based on the data output by the numerical routine from NAG, and illustrates how the temperature profile is affected by varying  $Pr$  over the interval between 1.0 and 7.0 (roughly corresponding to water), plotted at selected latitudes. For illustration, we model a cold body whose temperature is one unit lower than the fluid in the far field. For any cool-body case, the temperature profiles take on an identical shape, and data can be generated for arbitrary values of  $T_a$  and  $T_\infty$  by a simple scaling. The velocity profiles are as discussed in §2.2.2 and are independent of  $Pr$  at any particular  $\theta$ .

A comparison between the results of the series-solution method and the numerical method is included in the error analysis of §4.3.

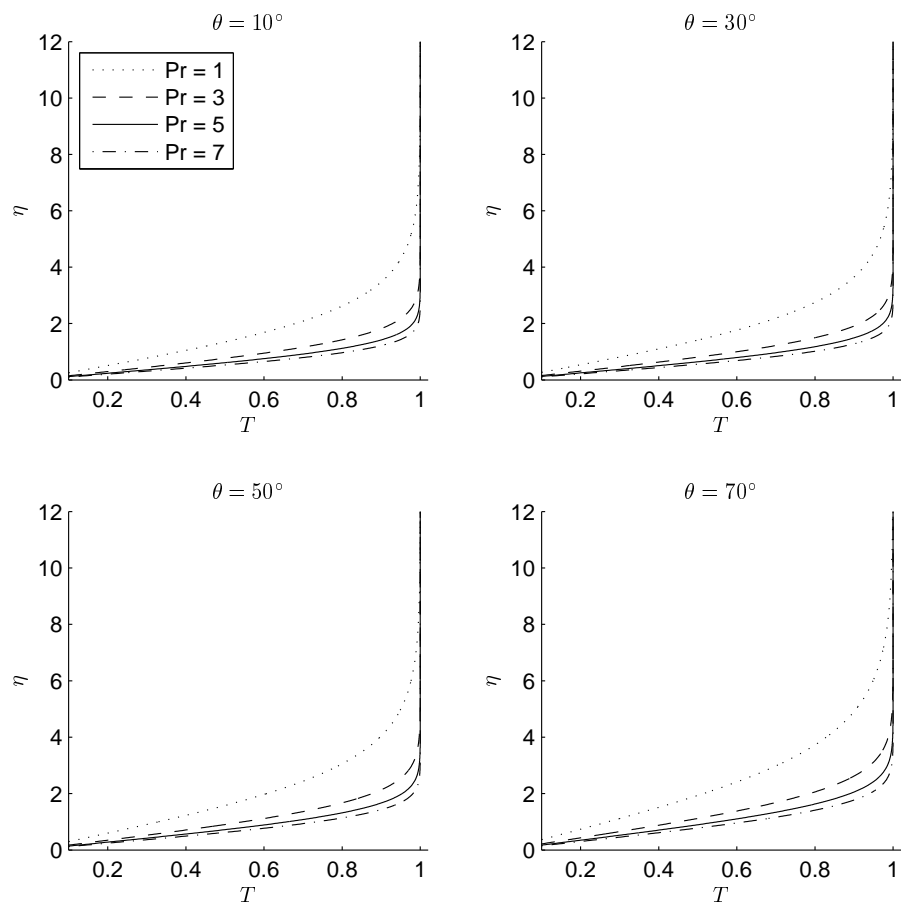


Figure 2.5: Temperature profiles for a one-unit temperature difference;  $\theta = 10^\circ, 30^\circ, 50^\circ, 70^\circ$ ; each with plots for  $Pr = 1, 3, 5, 7$  (top to bottom).

# Chapter 3

## Boundary-layer flow over a rotating sphere with heating and mass flux

In this chapter we examine the effects of distributed surface mass-flux on the steady-flow profiles over the rotating sphere for incompressible flow with heating that were described in §2.3. We introduce a parameter  $\iota^*$ , representing the mass flux through the sphere surface, and change the boundary condition for the normal velocity component such that  $W^* = \iota^*$  on the surface of the sphere. By scaling  $\iota^*$  on  $\sqrt{\nu^*\Omega^*}$ , the non-dimensional scaling for the  $W$ -component (see Chapter 2), we introduce the non-dimensional parameter,  $\iota$ :

$$\iota^* = \frac{a^*\Omega^*}{R}\iota,$$

where  $R = \frac{a^*\delta^*\Omega^*}{\nu^*}$  is the Reynolds number: a non-dimensional measure of the ratio of inertial forces to viscous forces. The Reynolds number will be discussed further in a later chapter, but it is sufficient here to understand that it will be interpreted as a measure of the spin rate for a sphere of fixed dimension. We note that the mass-flux parameter is related to the equatorial surface speed, but scaled on the Reynolds number that otherwise does not appear in the steady flow system. That the scaling of the mass-flux parameter depends only on global properties of the system (not

latitudinal location), means that a particular  $\iota$  can be used to represent the same mass-flux at all latitudes over the sphere. We let  $\iota$  vary between  $-1$  and  $1$ , with positive values interpreted as fluid injection, and negative values as suction. This range is imposed to limit the number of cases to be studied, but can be arbitrarily extended within this formulation.

With the addition of this parameter, the non-dimensional boundary conditions become

$$\begin{aligned} U = V - \sin \theta = 0, \quad W = \iota & \quad \text{on } \eta = 0, \\ U = V = 0 & \quad \text{as } \eta \rightarrow \infty. \end{aligned} \tag{3.1}$$

The system of PDEs governing the steady flow is identical to that in Chapter 2, and we now solve them numerically, using the previously described NAG routine, subject to these altered boundary conditions.

Figures 3.1–3.4 show the velocity and temperature profiles, subject to selected values of  $\iota$ . Each component is presented at  $\iota = -1, -0.5, 0, 0.5, 1$ , and on each set of axes a profile is plotted for a range of latitudes. Note that unless otherwise specified,  $Pr$  is fixed at  $0.7$  (the approximate Prandtl number for air at all temperatures), and the temperatures of the sphere surface and the free stream are fixed at  $0$  and  $1$ , respectively. As demonstrated by Equation (2.31), general surface and free stream-temperatures can be incorporated by a simple scaling; however, it is sufficient to consider only this simple case in the comparisons presented here. The plots corresponding to  $\iota = 0$  are identical to those in Chapter 2.

As might be expected, applying mass flux appears to have the most pronounced effect on the normal velocity component,  $W$ , although the latitudinal velocity,  $U$ , is also seen to be sensitive. The boundary conditions state that on  $\eta = 0$ ,  $W$  is equal to  $\iota$ , and this results in the translation of the lower part of the profile that is observable in Figure 3.3. We also see that suction increases the rate at which fluid is entrained into the boundary layer. Furthermore, injection is seen to exaggerate the region of normal reverse flow at higher latitudes.

Figure 3.1 shows that the  $U$  profile is also significantly distorted by high magni-

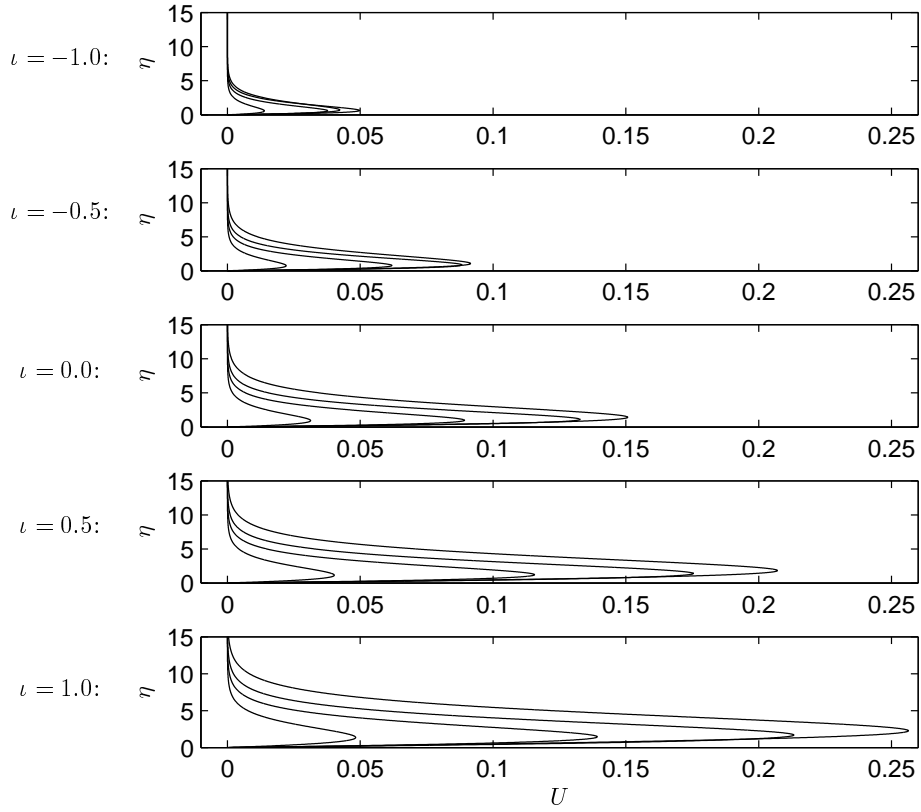


Figure 3.1: The effects of mass flux on  $U$  at  $\nu = -1.0, -0.5, 0, 0.5, 1.0$ , with each case plotted for  $\theta = 10^\circ, 30^\circ, 50^\circ, 70^\circ$  (left to right).

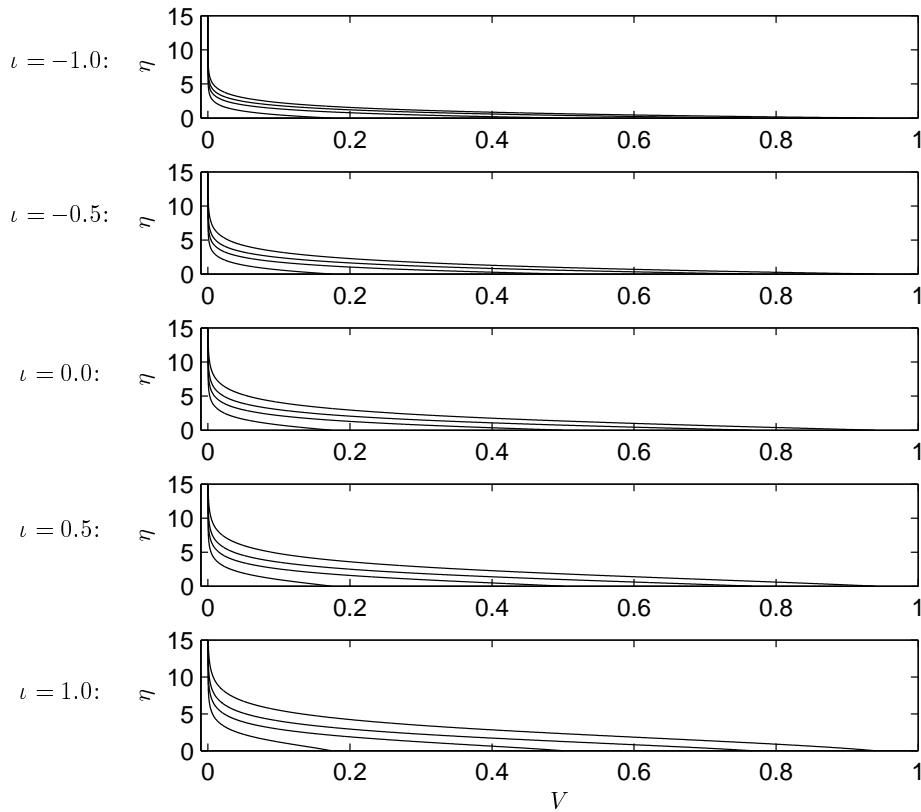


Figure 3.2: The effects of mass flux on  $V$  at  $\nu = -1.0, -0.5, 0, 0.5, 1.0$ , with each case plotted for  $\theta = 10^\circ, 30^\circ, 50^\circ, 70^\circ$  (bottom to top on each set of axes).

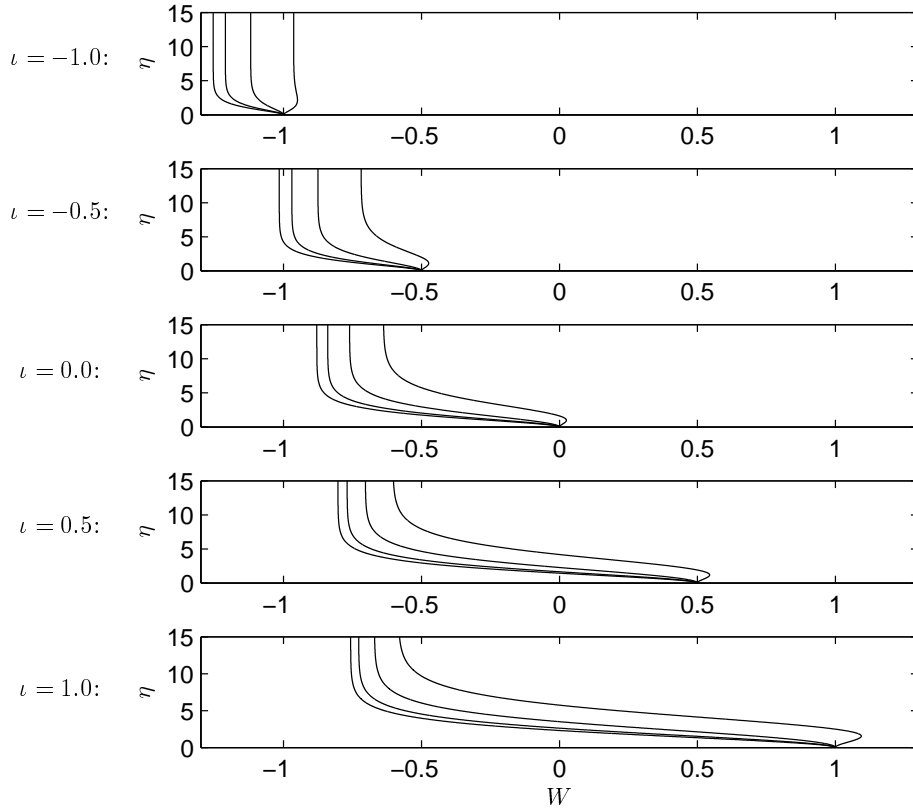


Figure 3.3: The effects of mass flux on  $W$  at  $\nu = -1.0, -0.5, 0, 0.5, 1.0$ , with each case plotted for  $\theta = 10^\circ, 30^\circ, 50^\circ, 70^\circ$  (left to right).

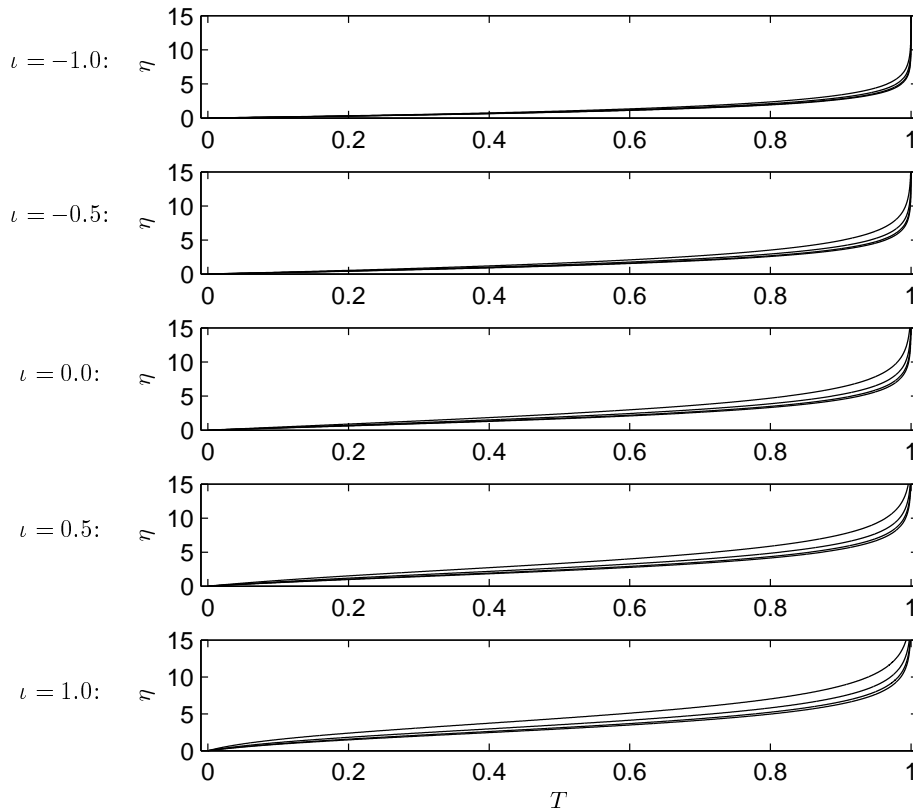


Figure 3.4: The effects of mass flux on  $T$  at  $\nu = -1.0, -0.5, 0, 0.5, 1.0$ , with each case plotted for  $\theta = 10^\circ, 30^\circ, 50^\circ, 70^\circ$  (bottom to top on each set of axes).

tudes of mass flux, with suction producing slower latitudinal jets close to the wall at all  $\theta$  and causing  $U$  to tend to zero more quickly with respect to  $\eta$ . Injection has the opposite effect, producing larger jets. We see that at a given  $\eta$ , the magnitude of the change in  $U$  caused by altering  $\iota$  is greater at higher latitudes. This means that at higher injection speeds,  $U$  has a greater range of values over the range of  $\theta$  considered.

The effects of mass flux on  $V$  and  $T$  are more subtle, but in both cases, suction causes the variable to tend to the free-stream boundary value over a shorter distance in  $\eta$ , and injection has the opposite effect. In physical terms the above observations on each flow component and temperature profile correspond to a narrowing of the boundary layer with suction, and thickening with injection. This is physically sensible.

Figures 3.5–3.7 show the effects of varying  $\iota$  at selected fixed latitudes and with fixed Prandtl number. Note that the velocity plots progress from left to right as  $\iota$  is increased from  $-1$  to  $1$ , while the temperature plots progress from right to left. In each case, the dotted line corresponds to the case of zero mass flux ( $\iota = 0$ ), and is identical to the corresponding plot in Chapter 2. Again we see that injection magnifies the streamwise wall jet effects at all latitudes and also the extent of normal reverse flow seen at higher latitudes (Figure 3.7). Both of these are effects close to the sphere surface.

Comparing the profiles in Figures 3.5–3.7 we see that in every case, for  $U$ ,  $V$  and  $T$ , the effects of mass flux appear to be greater for higher latitudes. For  $W$ , however, this trend appears to be reversed: the range of speeds attained as  $\iota$  moves from  $-1$  to  $1$  is narrower at higher latitudes.

We now proceed to examine the effects of different Prandtl numbers on the temperature profiles. As discussed in §2.3, the velocity profiles are independent of  $Pr$ , so they are not considered at this stage. Note that in this section,  $Pr$  is fixed at a constant value, whereas for many real fluids,  $Pr$  may change as a function of  $T$ . For fluids where  $Pr$  is particularly sensitive to  $T$ , care needs to be taken with the

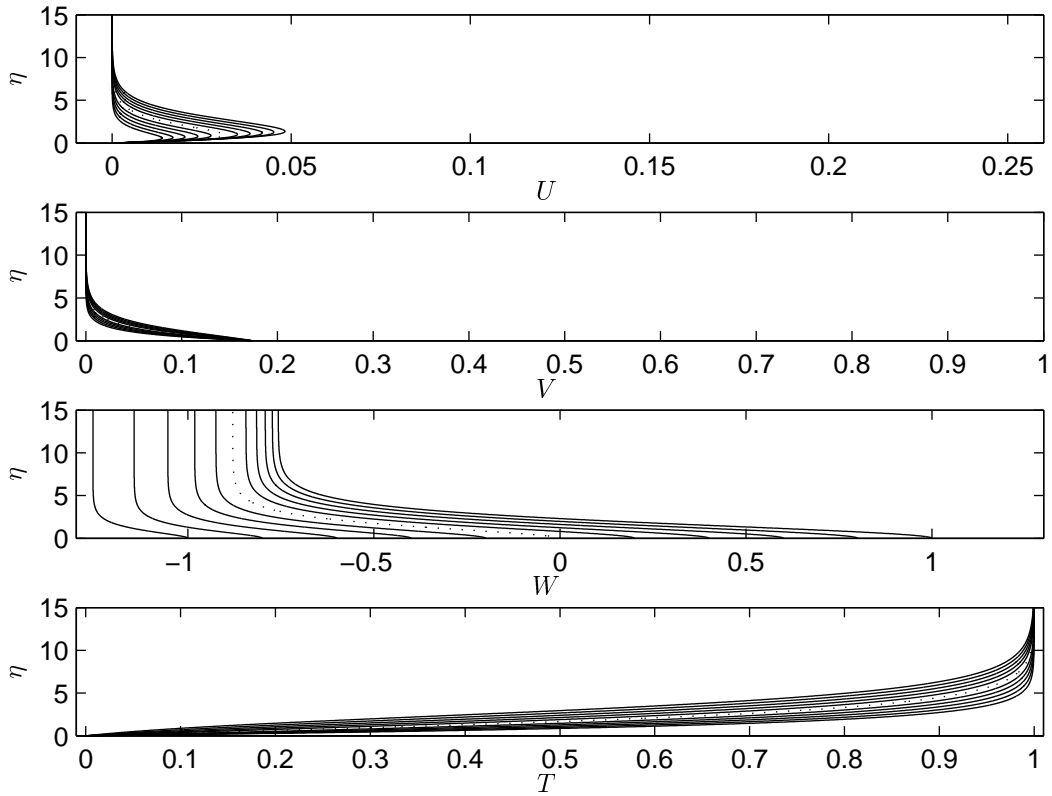


Figure 3.5: Velocity and temperature profiles at  $\theta = 10^\circ$ ; plotted for  $\nu = -1$  to  $1$ , in increments of  $0.2$ . For increasing  $\nu$ , the velocity plots can be seen going from left to right, while the temperature plots proceed from right to left.

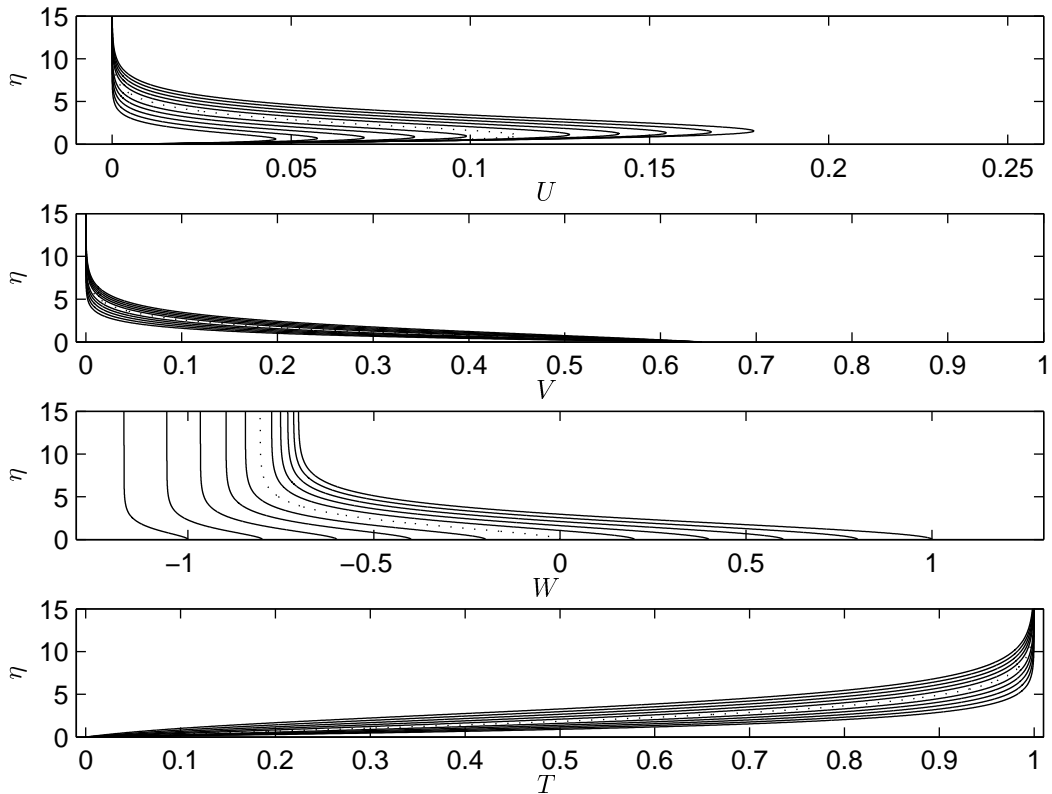


Figure 3.6: Velocity and temperature profiles at  $\theta = 40^\circ$ ; plotted for  $\nu = -1$  to  $1$ , in increments of  $0.2$ . For increasing  $\nu$ , the velocity plots can be seen going from left to right, while the temperature plots proceed from right to left.

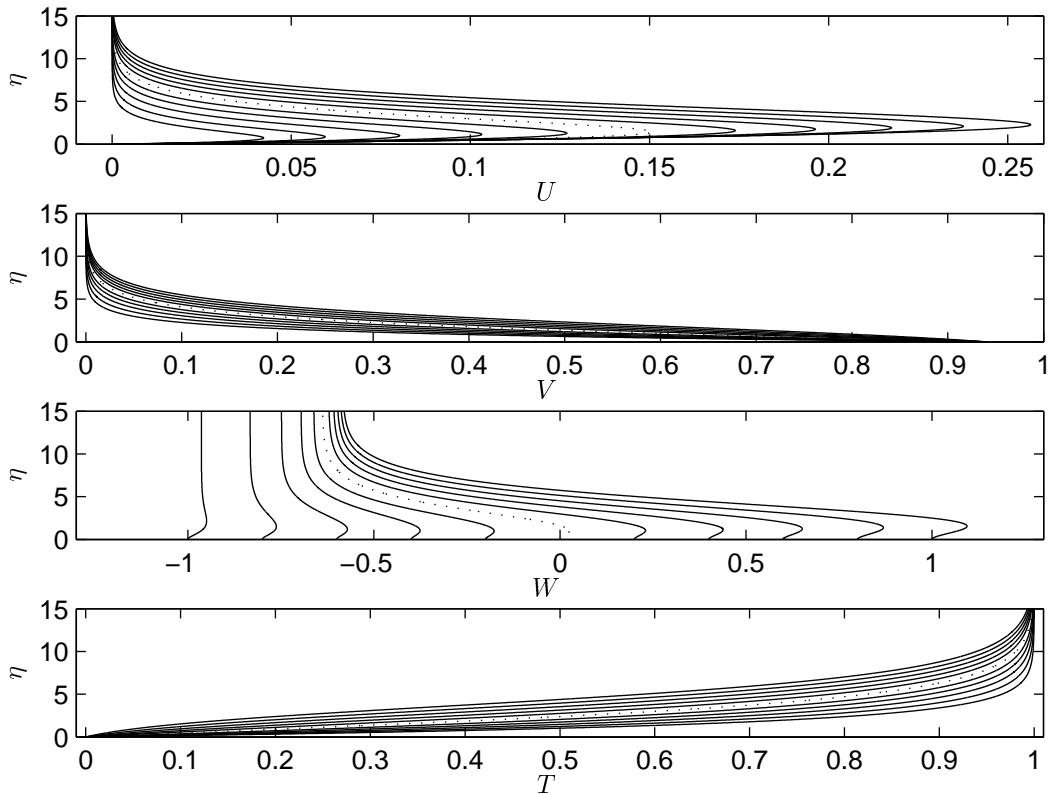


Figure 3.7: Velocity and temperature profiles at  $\theta = 70^\circ$ ; plotted for  $\nu = -1$  to  $1$ , in increments of  $0.2$ . For increasing  $\nu$ , the velocity plots can be seen going from left to right, while the temperature plots proceed from right to left.

interpretation of the results.

As Figures 3.8–3.10 all show, increasing the Prandtl number of the fluid causes  $T$  to change more quickly with respect to  $\eta$ , i.e. most of the change in  $T$  occurs closer to the sphere surface. This corresponds to a narrowing of the thermal boundary layer with increased  $\text{Pr}$ , as would be expected with a decrease in the relative thermal diffusion rate that increasing  $\text{Pr}$  corresponds to.

Figures 3.11 and 3.12 show similar plots to those presented above but for  $\text{Pr} = 7$ . This corresponds to water at a temperature of  $293\text{K}$ . Again we see injection/suction acting to thicken/narrow the thermal boundary layer. These effects are again seen to be exaggerated as the latitude is increased.

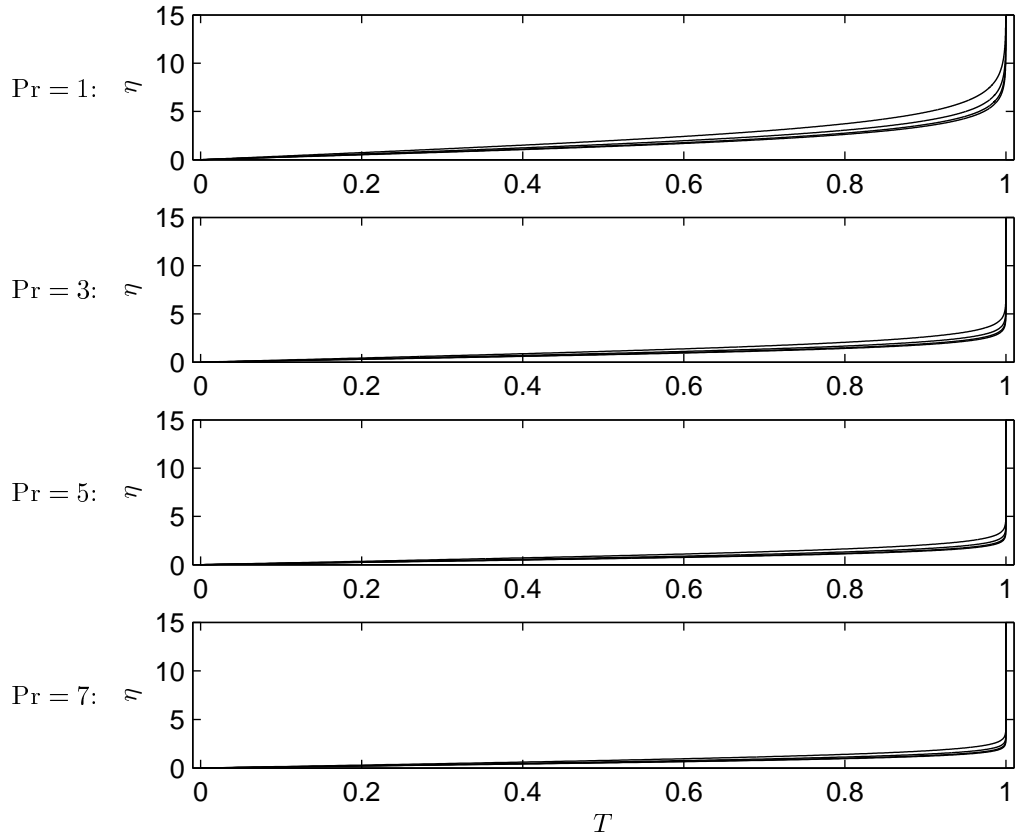


Figure 3.8: Temperature profiles at  $\iota = 0$ ,  $\text{Pr} = 1, 3, 5, 7$ ; each plotted for  $\theta = 10^\circ, 30^\circ, 50^\circ, 70^\circ$  (bottom to top on each set of axes).

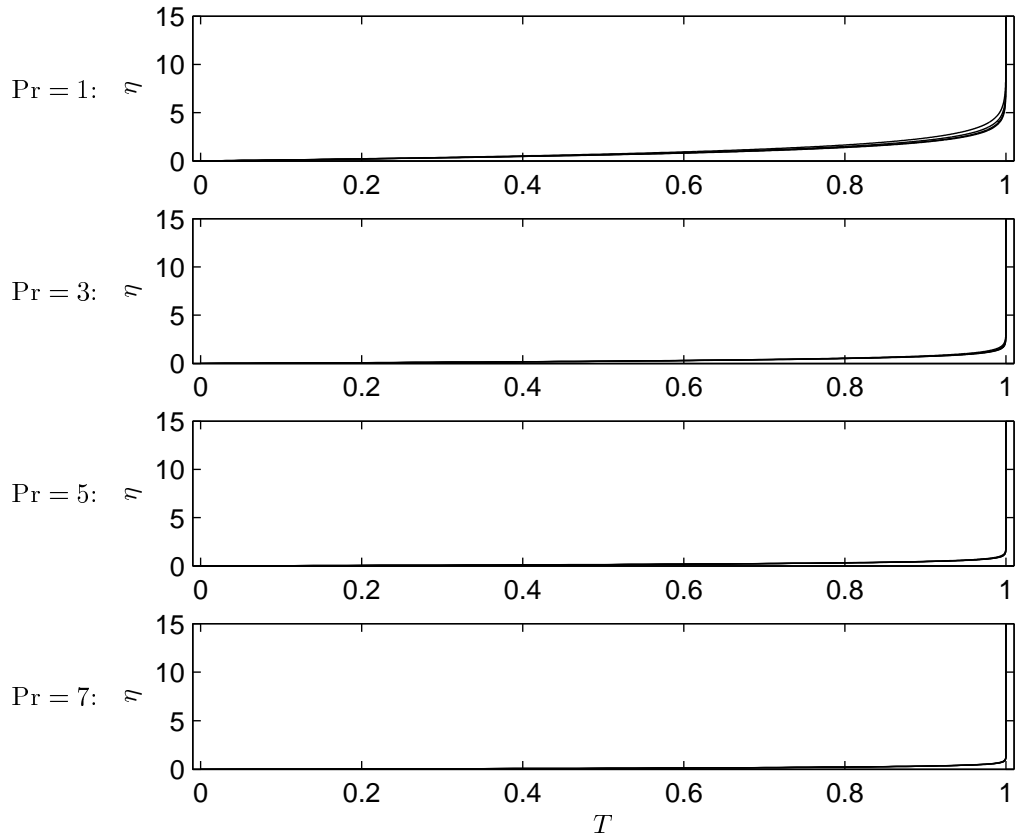


Figure 3.9: Temperature profiles at  $\iota = -1$ ,  $\text{Pr} = 1, 3, 5, 7$ ; each plotted for  $\theta = 10^\circ, 30^\circ, 50^\circ, 70^\circ$  (bottom to top on each set of axes).

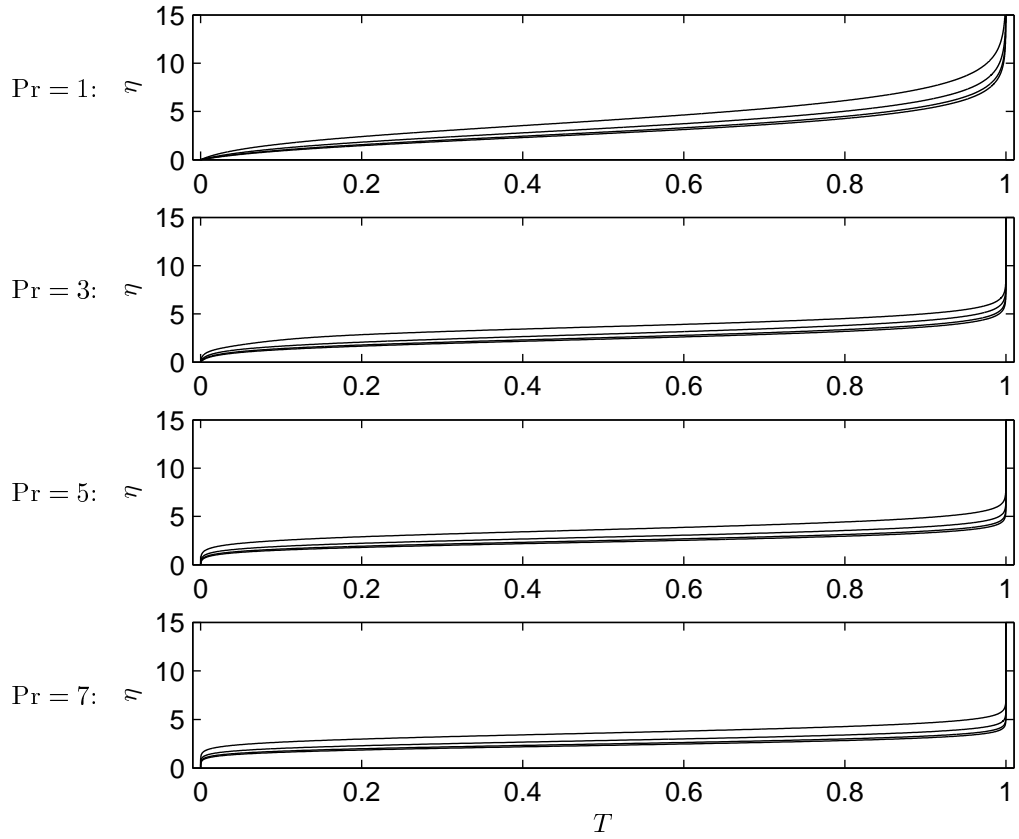


Figure 3.10: Temperature profiles at  $\iota = 1$ ,  $\text{Pr} = 1, 3, 5, 7$ ; each plotted for  $\theta = 10^\circ, 30^\circ, 50^\circ, 70^\circ$  (bottom to top on each set of axes).

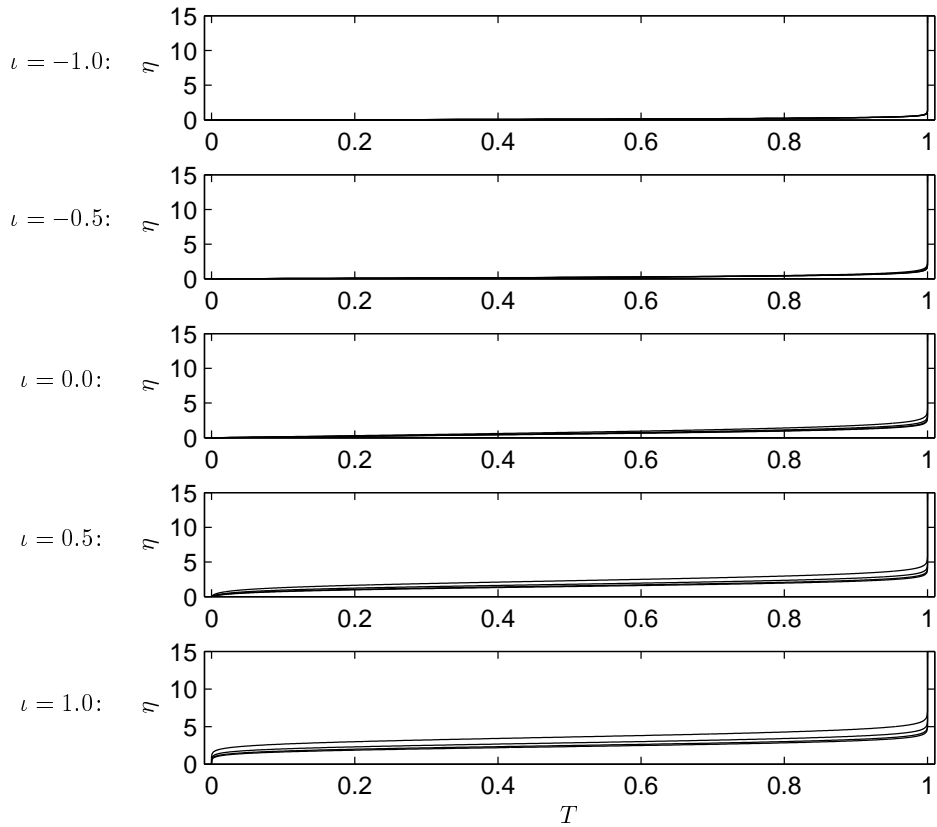


Figure 3.11: The effects of mass flux on  $T$  with  $\text{Pr} = 7$  at  $\iota = -1.0, -0.5, 0, 0.5, 1.0$ , with each case plotted for  $\theta = 10^\circ, 30^\circ, 50^\circ, 70^\circ$  (bottom to top on each set of axes).

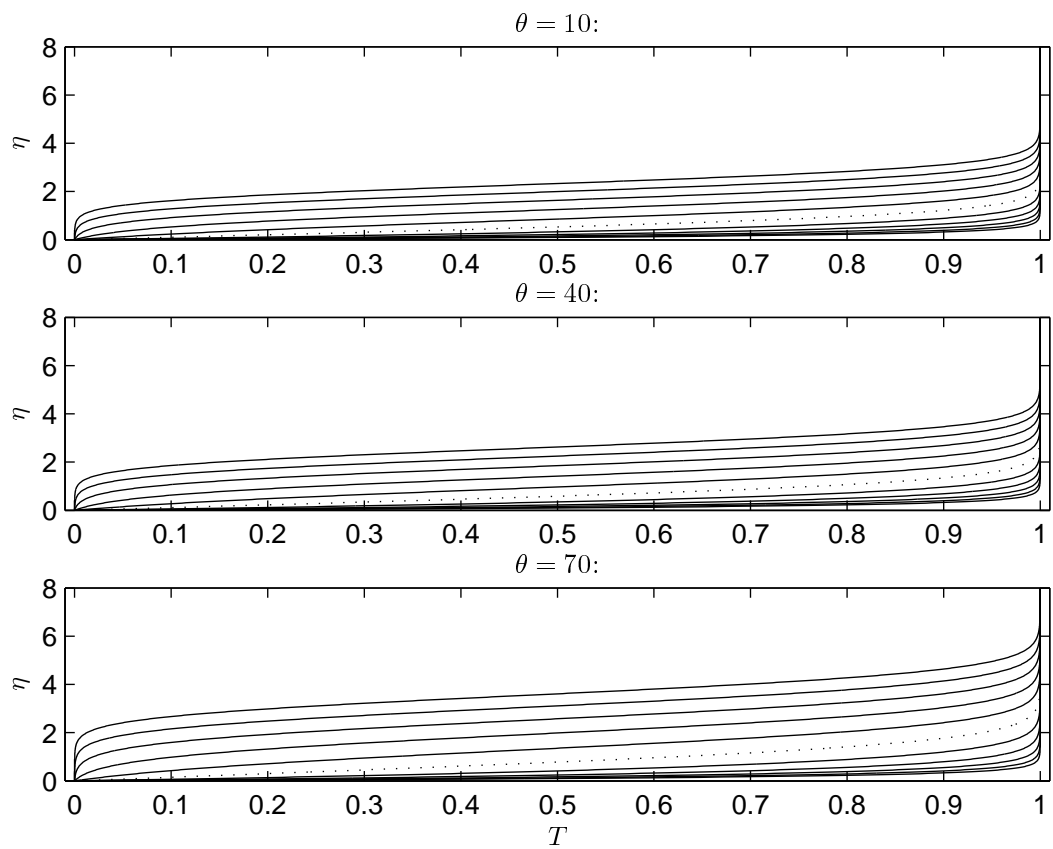


Figure 3.12: Temperature profiles at  $Pr = 7$ ;  $\theta = 10^\circ, 40^\circ, 70^\circ$ ; plotted for  $\nu = -1$  to  $1$  in increments of  $0.2$  (bottom to top).

# Chapter 4

## Introducing an axial flow

In this chapter, we extend the model with an additional parameter which controls the magnitude of a uniform flow enforced onto the rotating sphere, parallel to its axis of rotation. We take the same approach as Garrett (2002), Garrett & Peake (2004), and calculate the steady mean flow by solving the altered governing equations formulated in §4.1. We then examine the results in §4.2, with a view to understanding the combined effects of mass flux and axial flow on the behaviour of the velocity and temperature profiles.

### 4.1 Formulation

We let  $U_\infty^*$  be the dimensional free-stream speed of axial fluid flow, and  $U_0^*(\theta)$  be the latitudinal velocity distribution at the outer edge of the boundary layer, referred to as the slip velocity. The free-stream velocity is non-dimensionalised on the equatorial speed of the sphere by

$$\tau = U_\infty^*/a^*\Omega^*.$$

The form of  $U_0^*(\theta)$  is determined by the pressure distribution,  $P^*(\theta)$ , over the sphere, and satisfies

$$\frac{U_0^*}{a^*} \frac{\partial U_0^*}{\partial \theta} = -\frac{1}{a^*\rho^*} \frac{\partial P^*}{\partial \theta}. \quad (4.1)$$

It is non-dimensionalised on the free-stream speed by

$$U_0(\theta) = U_0^*/U_\infty^*.$$

The form of  $U_0(\theta)$  used throughout this work is a series expansion obtained experimentally by Fage (1936):

$$U_0(\theta) \approx 1.5\theta - 0.4371\theta^3 + 0.1481\theta^5 - 0.0423\theta^7, \quad (4.2)$$

where, in this case,  $\theta$  must be measured in radians. In using this we are assuming that the magnitude of suction is sufficiently small so as not to affect the free-stream flow around the sphere.

Using the above, we non-dimensionalise the governing equations stated by Mangler (1945), and we obtain

$$W \frac{\partial U}{\partial \eta} + U \frac{\partial U}{\partial \theta} - V^2 \cot \theta = \tau^2 U_0 \frac{dU_0}{d\theta} + \frac{\partial^2 U}{\partial \eta^2}, \quad (4.3)$$

$$W \frac{\partial V}{\partial \eta} + U \frac{\partial V}{\partial \theta} + UV \cot \theta = \frac{\partial^2 V}{\partial \eta^2}, \quad (4.4)$$

$$\frac{\partial W}{\partial \eta} + \frac{\partial U}{\partial \theta} + U \cot \theta = 0. \quad (4.5)$$

Note that in the case of zero axial flow ( $\tau = 0$ ), these equations reduce to Equations (2.5)–(2.7) derived in Chapter 2.

Also, we now have the far-field boundary condition that  $U = \tau U_0$ , so that the boundary conditions for the system become

$$\begin{aligned} U = V - \sin \theta = 0, \quad W = \iota \quad & \text{on } \eta = 0, \\ V = U - \tau U_0 = 0 \quad & \text{as } \eta \rightarrow \infty. \end{aligned} \quad (4.6)$$

We therefore have mass flux affecting the lower boundary conditions within the boundary layer and axial flow affecting the upper boundary conditions; these are assumed to be independent. Again, when  $\tau = 0$ , these conditions reduce to (2.8).

With a distribution chosen for  $U_0(\theta)$ , we can now simply use  $\tau$  as a parameter controlling the magnitude of axial flow. We allow  $\tau$  to vary between 0.00 and 0.25: a reasonable range of experimentally attainable values. This was the range considered by Garrett (2002) and Garrett & Peake (2004) in the absence of surface mass-flux.

We non-dimensionalise  $P^*$  using  $P = P^*/\rho^*(a^*\Omega^*)^2$ . Then at the edge of the boundary layer, from (4.1) we obtain

$$\frac{\partial P}{\partial \theta} = -\tau^2 U_0 \frac{dU_0}{d\theta}. \quad (4.7)$$

The slip-velocity distribution (4.2) attains a maximum at  $\theta = 1.2912$ , or  $74^\circ$ , and  $dU_0/d\theta$  is positive in the range  $0 \leq \theta < 1.2912$ . Given this, it can be seen from (4.7) that  $\partial P/\partial \theta$  is negative over the same range, which implies the existence of a favourable pressure gradient for all latitudes below  $74^\circ$ ; this is expected to have a stabilising effect on the flow.

## 4.2 Results

These governing equations are solved subject to their boundary conditions, using the commercially available NAG routine discussed in earlier chapters. Figures 4.1–4.4 show the combined effects of axial flow and mass flux on the profiles of each velocity component and temperature. In each figure, profiles are arranged in a  $3 \times 3$  grid, with rows corresponding to latitudes  $\theta = 10^\circ, 40^\circ$  and  $70^\circ$ . The central column corresponds to zero mass flux, while the left and right columns show example cases of suction and injection, respectively. Lines corresponding to zero axial flow are identical to corresponding results from Chapter 3.

Examining Figure 4.1, we see that increased axial flow causes  $U$  to tend to a larger constant value. It has a much greater effect on the streamwise flow component at higher latitudes. For any given latitude and axial-flow magnitude, mass flux does not alter the value to which  $U$  tends in the far field, although it does affect the

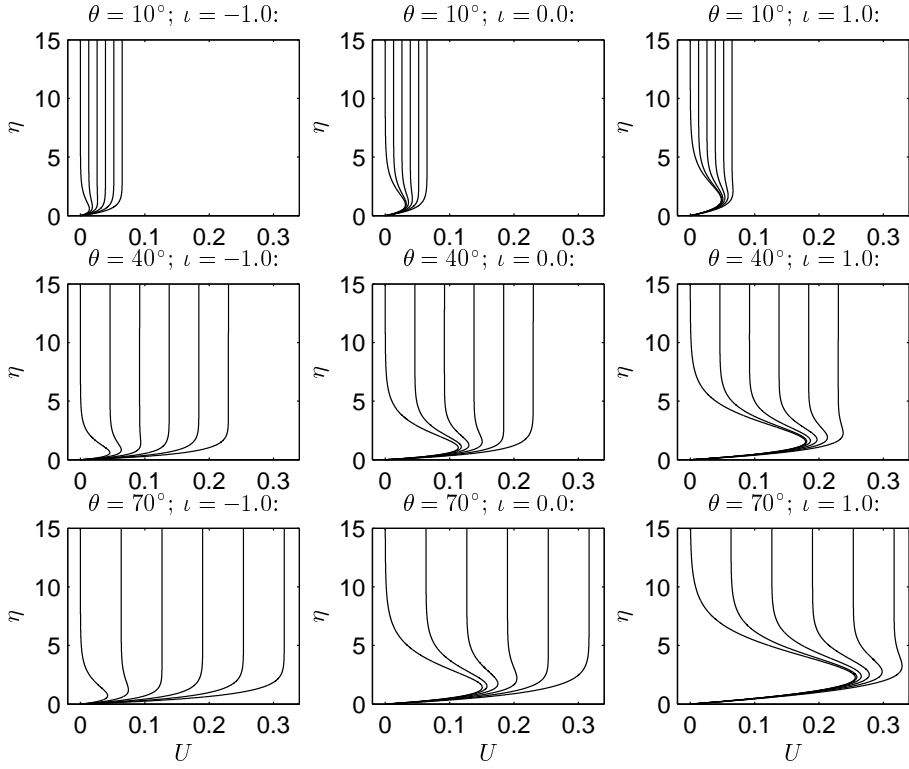


Figure 4.1:  $U$  profile at selected latitudes (rows) and selected  $\nu$  (columns), plotted for  $\tau = 0$  to 0.25 in increments of 0.05 (left to right in each frame).

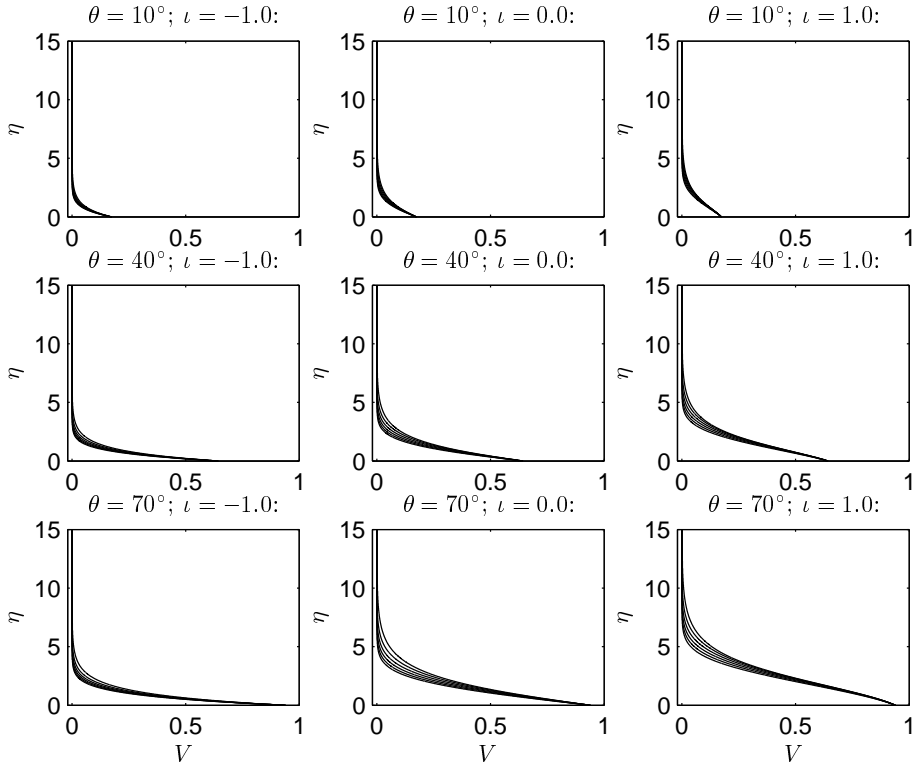


Figure 4.2:  $V$  profile at selected latitudes (rows) and selected  $\nu$  (columns), plotted for  $\tau = 0$  to 0.25 in increments of 0.05 (right to left in each frame).

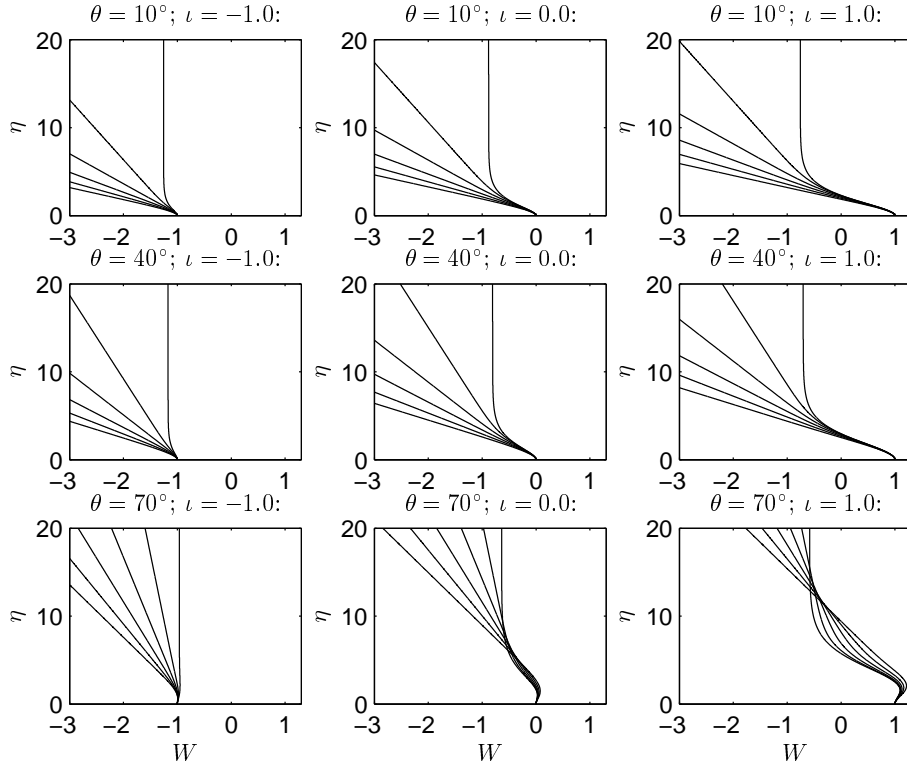


Figure 4.3:  $W$  profile at selected latitudes (rows) and selected  $\iota$  (columns), plotted for  $\tau = 0$  to 0.25 in increments of 0.05 (right to left in each frame). (In the case of the bottom-right frame, the order is right to left as measured at  $\eta = 20$ .)

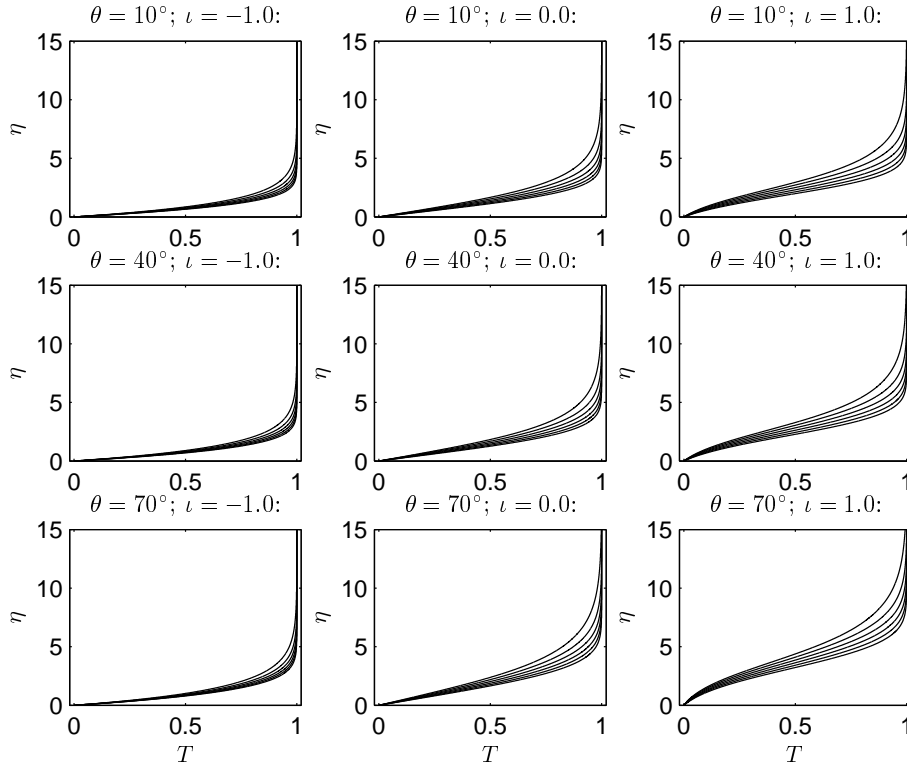


Figure 4.4:  $T$  profile at selected latitudes (rows) and selected  $\iota$  (columns), plotted for  $\tau = 0$  to 0.25 in increments of 0.05, at  $\text{Pr} = 0.7$  (top to bottom in each frame).

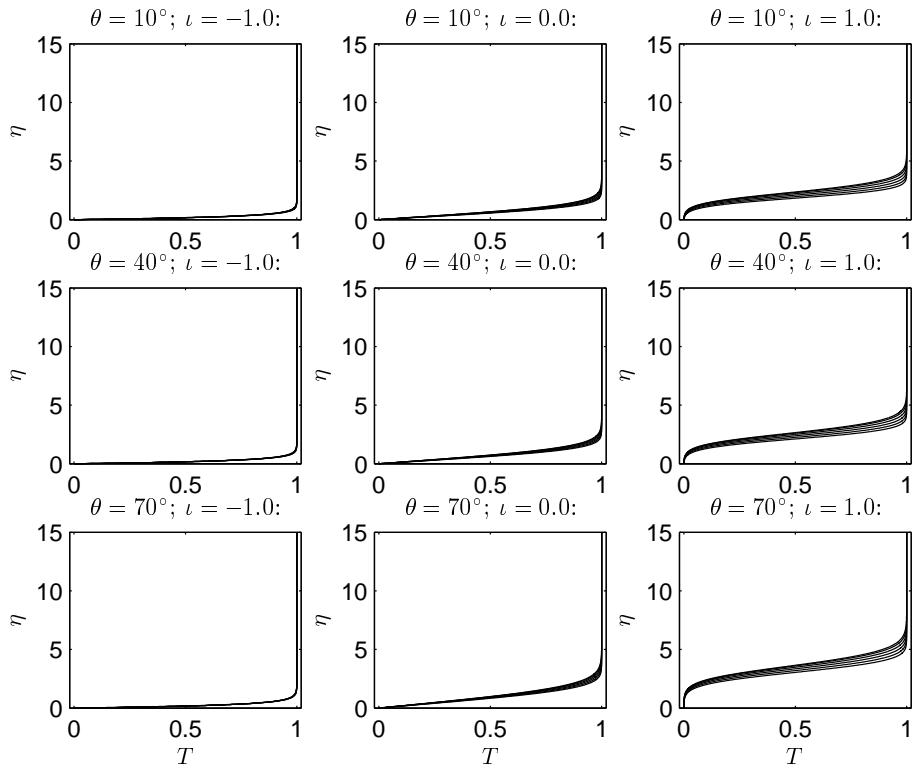


Figure 4.5:  $T$  profile at selected latitudes (rows) and selected  $\nu$  (columns), plotted for  $\tau = 0$  to 0.25 in increments of 0.05, at  $\text{Pr} = 4.0$  (top to bottom in each frame).

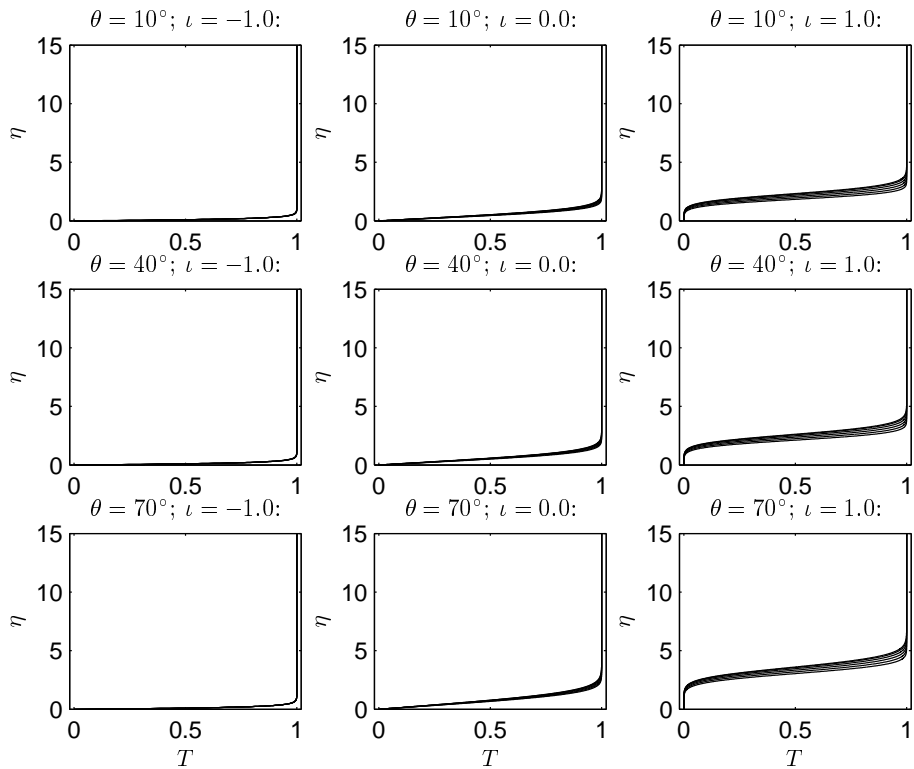


Figure 4.6:  $T$  profile at selected latitudes (rows) and selected  $\nu$  (columns), plotted for  $\tau = 0$  to 0.25 in increments of 0.05, at  $\text{Pr} = 7.0$  (top to bottom in each frame).

profile close to the sphere surface. The previously-observed distortion of the wall jets caused by mass flux is significantly reduced by increased rates of axial flow. This can be seen from the figure by observing that across any row, the left-most line undergoes a much larger change than the right-most.

Increasing axial flow has a less pronounced effect on  $V$ , but it clearly causes it to maintain a lower magnitude close to the sphere surface, eventually tending to the same constant value as  $\eta \rightarrow \infty$ . Similarly to the case for  $U$ , the effect is greater at higher latitudes. Mass flux appears to have a small effect, with positive values slightly magnifying the effects of axial flow.

It can be seen from Figure 4.3 that non-zero enforced axial flow prevents the normal velocity component,  $W$ , from tending to a constant value with increasing  $\eta$ , and instead causes it to assume a constant rate of change as  $\eta \rightarrow \infty$ . This implies that fluid is entrained into the boundary layer at unbounded speed as  $\eta \rightarrow \infty$ . As noted by Garrett (2002) and Garrett & Peake (2004), this is a consequence of the boundary-layer approximations used in the model; it is clearly impossible for the fluid to maintain this acceleration at an indefinite distance from the sphere, although El-Shaarawi *et al.* (1987) experimentally show that this behaviour does occur close to the surface in practice. The effects of axial flow are seen to *decrease* with increasing latitude.

Rearranging (4.5), we obtain

$$\frac{\partial W}{\partial \eta} = -\tau \left( U_0 \cot \theta + \frac{\partial U_0}{\partial \theta} \right).$$

Hence, the  $W$  gradient is independent of mass flux, which is clearly seen in Figure 4.3.

Increasing the axial flow rate causes  $T$  to tend more quickly (with respect to  $\eta$ ) to its free-stream value. This implies greater heat diffusion. Positive mass flux increases the effect varying axial flow has upon the behaviour of the  $T$  profile, while negative mass flux decreases it. Plots of these effects on  $T$  are presented for Pr values 0.7, 4.0 and 7.0, in Figures 4.4, 4.5 and 4.6, respectively. It can be seen

that for higher Pr, the greater heat diffusion causes the thermal boundary layer to become thinner, and the effects of other parameters upon the profiles are reduced.

### 4.3 Error in the series-solution method

It is these profiles calculated with the NAG routine on which we will perform stability analyses in later chapters. Having completed the model with these parameters, we examine the accuracy of the series-solution method by comparing it to the numerical method. For a quantitative measure of the series-solution's deviation from the numerical one, we take the root mean square (RMS) of the difference between corresponding results. The RMS error for some fixed injection ( $\iota$ ), axial flow ( $\tau$ ), Prandtl number (Pr), and latitude ( $\theta$ ) is given by

$$E_X(\iota, \tau, \text{Pr}, \theta) = \sqrt{\sum_{i=1}^N \frac{(X_n(\eta_i) - X_s(\eta_i))^2}{N}},$$

where  $X$  represents any one of the velocity or temperature components:  $U$ ,  $V$ ,  $W$ , or  $T$ , subject to the specified values for the four fixed parameters. The subscript  $n$  indicates that the component was calculated using the numerical method, while  $s$  indicates that it was obtained by the series-solution method. The sum is taken over a discrete set of  $N$  evenly-spaced values of  $\eta$  between 0 and 20.

Table 4.1 shows consistently higher error for higher latitudes, as is expected for a series solution in  $\theta$ . Higher rates of axial flow also cause increased error. Table 4.2 suggests that the effect of surface mass flux upon the error is less consistent than that of axial flow or increased latitude. With non-zero axial flow, the  $U$  and  $W$  errors appear to decrease slightly with increasingly positive mass flux, but they remain at the same order of magnitude. However, the error in  $V$  increases with both  $\tau$  and  $\iota$ .

Although Tables 4.1 and 4.2 show only data for Pr = 0.7, the error in  $T$  is found to increase with increased Pr. Since  $U$ ,  $V$  and  $W$  are independent of Pr, the error in these quantities is unaffected.

$\theta$	$\tau = 0.00$				$\tau = 0.10$			
	$U$	$V$	$W$	$T$	$U$	$V$	$W$	$T$
$10^\circ$	.00002	.00006	.00024	.00002	.00009	.00002	.02216	.00017
$30^\circ$	.00003	.00016	.00082	.00005	.00205	.00037	.14667	.00133
$50^\circ$	.00028	.00087	.00849	.00160	.00667	.00133	.21764	.00307
$70^\circ$	.00747	.02032	.18237	.03071	.01313	.00486	.35305	.00808
	$\times 10^{-1}$							

$\theta$	$\tau = 0.15$				$\tau = 0.25$			
	$U$	$V$	$W$	$T$	$U$	$V$	$W$	$T$
$10^\circ$	.00013	.00003	.03468	.00022	.00023	.00004	.06033	.00029
$30^\circ$	.00314	.00055	.22964	.00178	.00535	.00080	.40160	.00235
$50^\circ$	.01023	.00192	.34345	.00403	.01749	.00277	.60596	.00528
$70^\circ$	.02029	.00629	.57042	.00988	.03500	.00845	1.03609	.01233

Table 4.1: Error,  $E_X$ , in the series-solution method with  $\text{Pr} = 0.7$ ,  $\iota = 0.0$

$\iota$	$\tau = 0.00$				$\tau = 0.10$			
	$U$	$V$	$W$	$T$	$U$	$V$	$W$	$T$
-1	.00083	.00981	.08078	.00923	.00321	.00035	.24303	.00101
-0.5	.00264	.01234	.05226	.00648	.00319	.00047	.23774	.00140
0	.00264	.01584	.08211	.00490	.00314	.00055	.22964	.00178
0.5	.00534	.01901	.10852	.01047	.00308	.00058	.21999	.00211
1	.00792	.02215	.10279	.01551	.00300	.00059	.20934	.00242
	$\times 10^{-3}$							

$\iota$	$\tau = 0.15$				$\tau = 0.25$			
	$U$	$V$	$W$	$T$	$U$	$V$	$W$	$T$
-1	.00431	.00041	.32727	.00115	.00541	.00045	.41168	.00125
-0.5	.00428	.00056	.32274	.00161	.00539	.00062	.40801	.00175
0	.00424	.00069	.31507	.00211	.00535	.00080	.40160	.00235
0.5	.00417	.00077	.30501	.00259	.00529	.00094	.39218	.00296
1	.00410	.00082	.29363	.00303	.00521	.00104	.38073	.00354

Table 4.2: Error,  $E_X$ , in the series-solution method with  $\text{Pr} = 0.7$ ,  $\theta = 30^\circ$

The series-solution method is considerably simpler to implement and so, for this reason, would be preferable to incorporate into engineering design codes. However, given the inaccuracies just described, the series-solution method is of significantly less use once these additional parameters are included in the model and, despite its ease of use, we focus on the NAG profiles in all that follows. We do not recommend using the series-solution method in any application, with the exception of at latitudes very close to the pole.

# Chapter 5

## Convective stability analysis with emphasis on critical Reynolds number

In this chapter, a theoretical convective stability analysis is performed on the previously described system.

Convective instability is characterised by a response to an initial disturbance which grows in space, but which convects away from the source, leaving the fluid at the source undisturbed after some period of time; see §1.2. Physically, convective instability in the rotating sphere and related systems is known to give rise to co-rotating spiral vortices, and we proceed with the analysis by fixing the local speed of these vortices with respect to the sphere surface. This speed is referred to as  $c$ , and is defined in §5.3.

In §5.1, the perturbation equations are derived. In §§5.3 and 5.4, stability analyses are conducted using these equations. §5.3 uses the assumption that vortices are stationary with respect to the sphere surface ( $c = 1$ ), while §5.4 permits travelling vortices. It is assumed throughout that any disturbances to the mean flow are of sufficiently small magnitude that no secondary instability occurs, and transition is controlled only by the primary instability of the steady flow profiles.

In formulating the problem, we make the assumption that the boundary layer is locally spatially homogeneous. This is sometimes called the “parallel flow” approximation, and amounts to assuming that  $\eta/R \approx 0$  in some instances. Because the critical Reynolds numbers are generally lower at high latitudes, and the boundary layer is typically thicker, the validity of this approximation decreases with proximity to the equator, but as discussed by Garrett (2002), the error remains within a tolerable magnitude. The parallel-flow assumption simplifies the governing equations by removing the dependence on latitudinal position, apart from via the steady flows obtained in Chapters 2–4, but limits us to performing a “local” analysis, i.e. we can only analyse the behaviour of the boundary layer at individual latitudes, where we observe the reaction of the local velocity profile to the initial disturbance, rather than over the whole streamwise extent of the sphere. However, an investigation into the global behaviour is presented in Chapter 8.

In the case of incompressible fluid considered here, the stability properties are completely defined by the velocity and pressure profiles; the temperature profiles considered in Chapters 2–4 have no effect. We therefore focus on the  $U$ ,  $V$ ,  $W$  and  $P$  profiles in what follows.

## 5.1 Derivation of the perturbation equations

We now derive perturbation equations by adding infinitesimally small perturbing quantities to each of the basic variables,  $U^*(\eta, \theta; \iota, \tau)$ ,  $V^*(\eta, \theta; \iota, \tau)$ ,  $W^*(\eta, \theta; \iota, \tau)$  and  $P^*(\eta, \theta; \iota, \tau)$  at particular latitudinal positions,  $\theta$ . Once again, we initially follow Garrett (2002) in the formulation of the problem. The perturbing quantities are assumed to have the normal mode form given by

$$(\hat{u}^*, \hat{v}^*, \hat{w}^*, \hat{p}^*) = (u^*(r^*), v^*(r^*), w^*(r^*), p^*(r^*))e^{i(\alpha^* a^* \theta + \beta^* a^* \phi \sin \theta - \gamma^* t^*)}, \quad (5.1)$$

where  $\alpha^*$  and  $\beta^*$  are the dimensional wavenumbers of the disturbance in the directions of  $\theta$  and  $\phi$ , respectively, and  $\gamma^*$  is the temporal frequency. Hence, we write

the perturbed variables as

$$(\bar{U}^*, \bar{V}^*, \bar{W}^*, \bar{P}^*) = (U^* + \hat{u}^*, V^* + \hat{v}^*, W^* + \hat{w}^*, P^* + \hat{p}^*)$$

Substituting these perturbed quantities into the previously derived governing equations, (2.2)–(2.4), we obtain

$$\begin{aligned} W^* \frac{du^*}{dr^*} + \left[ i \left\{ (\alpha^* U^* + \beta^* V^*) \frac{a^*}{r^*} - \gamma^* \right\} + \frac{1}{r^*} \left( \frac{\partial U^*}{\partial \theta} + W^* \right) \right] u^* \\ - \frac{2V^* \cot \theta}{r^*} v^* + \left( \frac{\partial U^*}{\partial r^*} + \frac{U^*}{r^*} \right) w^* = - \frac{i\alpha^* a^* p^*}{r^* \rho^*} \\ + \nu^* \left[ \frac{d^2 u^*}{dr^{*2}} + \frac{2}{r^*} \frac{du^*}{dr^*} + \left\{ -(\alpha^{*2} + \beta^{*2}) \frac{a^{*2}}{r^{*2}} + \frac{i\alpha^* a^* \cot \theta}{r^{*2}} \right. \right. \\ \left. \left. + \frac{1}{r^{*2} \sin^2 \theta} \right\} u^* - \frac{2i\beta^* a^* \cot \theta}{r^{*2}} v^* + \frac{2i\beta^* a^*}{r^{*2}} w^* \right], \end{aligned} \quad (5.2)$$

$$\begin{aligned} W^* \frac{dv^*}{dr^*} + \left[ i \left\{ (\alpha^* U^* + \beta^* V^*) \frac{a^*}{r^*} - \gamma^* \right\} + \frac{1}{r^*} (U^* \cot \theta + W^*) \right] v^* \\ + \left( \frac{\partial V^*}{\partial \theta} + V^* \cot \theta \right) \frac{u^*}{r^*} + \left( \frac{\partial V^*}{\partial r^*} + \frac{V^*}{r^*} \right) w^* = - \frac{i\beta^* a^* p^*}{r^* \rho^*} \\ + \nu^* \left[ \frac{d^2 v^*}{dr^{*2}} + \frac{2}{r^*} \frac{dv^*}{dr^*} + \left\{ -(\alpha^{*2} + \beta^{*2}) \frac{a^{*2}}{r^{*2}} + \frac{i\alpha^* a^* \cot \theta}{r^{*2}} \right. \right. \\ \left. \left. - \frac{2}{r^{*2} \sin^2 \theta} \right\} v^* + \frac{2(i\alpha^* a^* \cot \theta)}{r^{*2}} u^* + \frac{2i\beta^* a^*}{r^{*2}} w^* \right], \end{aligned} \quad (5.3)$$

$$\begin{aligned} W^* \frac{dw^*}{dr^*} + \left[ i \left\{ (\alpha^* U^* + \beta^* V^*) \frac{a^*}{r^*} - \gamma^* \right\} + \frac{\partial W^*}{\partial r^*} \right] w^* \\ + \frac{2V^*}{r^*} v^* + \left( \frac{\partial W^*}{\partial \theta} - 2U^* \right) \frac{u^*}{r^*} = - \frac{1}{\rho^*} \frac{dp^*}{dr^*} \\ + \nu^* \left[ \frac{d^2 w^*}{dr^{*2}} + \frac{2}{r^*} \frac{dw^*}{dr^*} + \left\{ -(\alpha^{*2} + \beta^{*2}) \frac{a^{*2}}{r^{*2}} + \frac{i\alpha^* a^* \cot \theta}{r^{*2}} \right. \right. \\ \left. \left. - \frac{2}{r^{*2}} \right\} w^* - \frac{2(i\alpha^* a^* + \cot \theta)}{r^{*2}} u^* - \frac{2i\beta^* a^*}{r^{*2}} v^* \right], \end{aligned} \quad (5.4)$$

$$\frac{i\alpha^* a^* + \cot \theta}{r^*} u^* + \frac{i\beta^* a^*}{r^*} v^* + \frac{2}{r^*} w^* + \frac{dw^*}{dr^*} = 0. \quad (5.5)$$

Equations (5.2)–(5.5) can be non-dimensionalised by introducing the scaled variables:

$$(u, v, w) = (u^*, v^*, w^*) / a^* \Omega^*,$$

$$p = p^* / \rho^* a^{*2} \Omega^{*2},$$

$$\alpha = \alpha^* \delta^*,$$

$$\beta = \beta^* \delta^*,$$

$$\gamma = \gamma^* \delta^* / a^* \Omega^*,$$

$$\delta_1 = \delta^* / a^*.$$

During this spatial analysis,  $\alpha$  is in general complex, while  $\beta$  and  $\gamma$  remain real. We use  $\alpha_r$  and  $\alpha_i$  to refer to the real and imaginary parts of  $\alpha$ , respectively. The Reynolds number is defined as in Chapter 3:  $R = \frac{a^* \delta^* \Omega^*}{\nu^*}$ .  $R$  is the dimensionless ratio of inertial forces to viscous forces; for a sphere of fixed radius,  $a^*$ , this formulation allows  $R$  to be interpreted as the spin rate. This is contrast to the interpretation of the Reynolds number in studies of the rotating disk, where, for fixed rotation rate, it gives the non-dimensional radial position of the stability analysis. For the sphere the corresponding position is given by the latitude,  $\theta$ .

$U^*$ ,  $V^*$ ,  $W^*$  are non-dimensionalised using the same scalings as in Chapter 2. This yields the following system of equations:

$$\begin{aligned} \delta_1 W \frac{du}{d\eta} + \left[ i \{ (\alpha U + \beta V) l - \gamma \} + \delta_1 l \frac{\partial U}{\partial \theta} \right] u - 2V \delta_1 l \cot \theta \\ + \left( \frac{\partial U}{\partial \eta} + \delta_1 l U \right) w = -i\alpha l p + \frac{1}{R} \left[ \frac{d^2 u}{d\eta^2} - l^2 (\alpha^2 + \beta^2) u \right], \end{aligned} \quad (5.6)$$

$$\begin{aligned} \delta_1 W \frac{dv}{d\eta} + [i \{ (\alpha U + \beta V) l - \gamma \} + \delta_1 l U \cot \theta] v + \left( \frac{\partial V}{\partial \theta} + V \cot \theta \right) \delta_1 l u \\ + \left( \frac{\partial V}{\partial \eta} + \delta_1 l V \right) w = -i\beta l p + \frac{1}{R} \left[ \frac{d^2 v}{d\eta^2} - l^2 (\alpha^2 + \beta^2) v \right], \end{aligned} \quad (5.7)$$

$$\begin{aligned} \delta_1 W \frac{dw}{d\eta} + \left[ i \{ (\alpha U + \beta V) l - \gamma \} + \delta_1 \frac{\partial W}{\partial \eta} \right] w - 2U \delta_1 l u - 2V \delta_1 l v \\ = -\frac{dp}{d\eta} + \frac{1}{R} \left[ \frac{d^2 w}{d\eta^2} - l^2 (\alpha^2 + \beta^2) w \right], \end{aligned} \quad (5.8)$$

$$\frac{dw}{d\eta} + 2\delta_1 l w = -l \{ (i\alpha + \delta_1 \cot \theta) u + i\beta v \}, \quad (5.9)$$

where  $l = 1/(1 + \delta_1 \eta)$ . During the stability analyses, we make the assumption that  $l = 1$ , representing the parallel-flow assumption described at the start of this chapter. We introduce the following scaled variables:

$$\phi_1(\eta; \alpha, \beta, \gamma; R, \theta) = \left( \alpha - \frac{i}{R} \right) u + \beta v, \quad (5.10)$$

$$\phi_2(\eta; \alpha, \beta, \gamma; R, \theta) = \left( \alpha - \frac{i \cot \theta}{R} \right) u' + \beta v', \quad (5.11)$$

$$\phi_3(\eta; \alpha, \beta, \gamma; R, \theta) = w, \quad (5.12)$$

$$\phi_4(\eta; \alpha, \beta, \gamma; R, \theta) = p, \quad (5.13)$$

$$\phi_5(\eta; \alpha, \beta, \gamma; R, \theta) = \left( \alpha - \frac{i \cot \theta}{R} \right) v + \beta u, \quad (5.14)$$

$$\phi_6(\eta; \alpha, \beta, \gamma; R, \theta) = \left( \alpha - \frac{i \cot \theta}{R} \right) v' + \beta u', \quad (5.15)$$

where a prime denotes differentiation with respect to  $\eta$ . Using (5.10)–(5.15) and Equations (5.6)–(5.9), the following system of six differential equations can be de-

rived:

$$\phi'_1 = \phi_2, \quad (5.16)$$

$$\begin{aligned} \left[ \frac{\phi'_2}{R} \right]_v &= \frac{1}{R} \left( [\alpha^2 + \beta^2]_v + iR(\alpha U + \beta V - \gamma) \right) \phi_1 + \left[ \frac{W\phi_2}{R} \right]_s \\ &+ \left( \alpha_1 U' + \beta V' + \left[ \frac{1}{R} (\alpha_1 U + \beta V) \right]_s \right) \phi_3 + i \left( \alpha^2 + \beta^2 - \left[ \frac{i\alpha \cot \theta}{R} \right]_s \right) \phi_4 \\ &- \left[ \frac{V \cot \theta \phi_5}{R} \right]_s + \left[ \frac{1}{R} \left( \left( \alpha_1 \frac{\partial U}{\partial \theta} + \beta \frac{\partial V}{\partial \theta} \right) u - (\alpha_1 V - \beta U) v \cot \theta \right) \right]_s, \end{aligned} \quad (5.17)$$

$$\phi'_3 = -i\phi_1 - \left[ \frac{2\phi_3}{R} \right]_s, \quad (5.18)$$

$$\begin{aligned} \phi'_4 &= \left[ \frac{iW\phi_1}{R} \right]_s - \left[ \frac{i\phi_2}{R} \right]_v + \left[ \frac{2}{R} (Uu + Vv) \right]_s \\ &- \frac{1}{R} \left( [\alpha^2 + \beta^2]_v + iR(\alpha U + \beta V - \gamma) + W'_s \right) \phi_3, \end{aligned} \quad (5.19)$$

$$\phi'_5 = \phi_6, \quad (5.20)$$

$$\begin{aligned} \left[ \frac{\phi'_6}{R} \right]_v &= \left[ \frac{V \cot \theta \phi_1}{R} \right]_s + \left[ \frac{W\phi_6}{R} \right]_s + \left[ \frac{\beta \cot \theta \phi_4}{R} \right]_s + \left( \alpha_1 V' - \beta U' \right. \\ &+ \left. \left[ \frac{1}{R} (\alpha_1 V - \beta U) \right]_s \right) \phi_3 + \left[ \frac{1}{R} \left( \left( \alpha_1 \frac{\partial V}{\partial \theta} - \beta \frac{\partial U}{\partial \theta} \right) u + (\alpha_1 U + \beta V) v \cot \theta \right) \right]_s \\ &+ \frac{1}{R} \left( [\alpha^2 + \beta^2]_v + iR(\alpha U + \beta V - \gamma) \right) \phi_5, \end{aligned} \quad (5.21)$$

with  $\alpha_1 = \alpha - (i \cot \theta / R)$ . Terms with the subscript  $s$  arise due to streamline curvature, while terms with the subscript  $v$  arise due to viscous effects.

Equations (5.16)–(5.21) represent an eigenvalue problem for which solutions will be found during the stability analysis, subject to the homogeneous boundary conditions,

$$\begin{aligned}\phi_i &= 0 & \text{on} & \quad \eta = 0 \\ \phi_i &\rightarrow 0 & \text{as} & \quad \eta \rightarrow \infty,\end{aligned}\tag{5.22}$$

for  $i = 1, 2, \dots, 6$ . These conditions stipulate that the perturbations are contained within the boundary layer. We note that (5.16)–(5.21) are identical to Garrett’s. We further note that neglecting streamline curvature terms leads to the standard Orr-Sommerfeld equation,

$$\begin{aligned}\frac{i}{R}(\phi_3'''' - 2(\alpha^2 + \beta^2)\phi_3'' + (\alpha^2 + \beta^2)^2\phi_3) \\ + (\alpha U + \beta V - \gamma)(\phi_3'' - (\alpha^2 + \beta^2)\phi_3) - (\alpha U'' + \beta V'')\phi_3 = 0.\end{aligned}$$

Additionally neglecting viscous terms leads to the Rayleigh equation,

$$(\alpha U + \beta V - \gamma)(\phi_3'' - (\alpha^2 + \beta^2)\phi_3) - (\alpha U'' + \beta V'')\phi_3 = 0.$$

This thesis considers the full version of the perturbation equations only. However, it is instructive to demonstrate their consistency with the standard equations of stability theory.

Note that because  $\iota$  does not appear in the mean-flow equations, (4.3)–(4.5), the perturbation equations derived above are independent of  $\iota$ . Because  $\tau$  only appears in the pressure term of (4.5), which is determined completely by the slip velocity, the perturbation equations are also independent of  $\tau$ . Thus, the introduction of axial flow and surface mass-flux parameters only affects the steady mean-flow profiles upon which the stability analysis is performed, and Equations (5.16)–(5.21) are identical to the equations that would be used in the absence of these parameters.

## 5.2 Solution method

In this section, the method of solving the perturbation equations is described. The description given here is brief, since the method is the same as that used by Garrett (2002), who provides a more detailed explanation in his thesis.

The system of equations allows six independent solutions for each of  $\phi_1, \phi_2, \dots, \phi_6$ . For each of the transformed variables, a superscript  $j$  is used to indicate which of the six possible solutions is being referred to. Hence, solutions have the form  $\phi_i^j(\eta; \alpha, \beta, \gamma; R, \theta; \iota, \tau)$ . We form each full solution,  $\phi_i$ , by taking a linear combination of these, discounting those which do not decay with  $\eta$ , since they fail to satisfy the second boundary condition of (5.22).

At the edge of the boundary layer, the equations take on the form

$$\phi_1' = \phi_2, \quad (5.23)$$

$$\begin{aligned} \phi_2' = & (\alpha^2 + \beta^2 + iR(\alpha U_\infty - \gamma)) \phi_1 + W_\infty \phi_2 + \alpha_1 U_\infty \phi_3 \\ & + iR \left( \alpha^2 + \beta^2 - \frac{i\alpha \cot \theta}{R} \right) \phi_4 + \alpha_1 \frac{\partial U_\infty}{\partial \theta} u + \beta U_\infty v \cot \theta, \end{aligned} \quad (5.24)$$

$$\phi_3' = -i\phi_1 - \frac{2\phi_3}{R}, \quad (5.25)$$

$$R\phi_4' = iW_\infty \phi_1 - i\phi_2 + 2U_\infty u - (\alpha^2 + \beta^2 + iR(\alpha U_\infty - \gamma) + W_\infty') \phi_3, \quad (5.26)$$

$$\phi_5' = \phi_6, \quad (5.27)$$

$$\begin{aligned} \phi_6' = & W_\infty \phi_6 + \beta \cot \theta \phi_4 - (R\beta U_\infty' + \beta U_\infty) \phi_3 \\ & - \beta \frac{\partial U_\infty}{\partial \theta} u + \alpha_1 U_\infty v \cot \theta + (\alpha^2 + \beta^2 + iR(\alpha U_\infty - \gamma)) \phi_5. \end{aligned} \quad (5.28)$$

Equations (5.23)–(5.28) are obtained by substituting the boundary values of  $U$ ,  $V$  and  $W$  into the system (5.16)–(5.21) for  $\eta \rightarrow \infty$ .  $U_\infty$  and  $W_\infty$  are these boundary values of  $U$  and  $W$ , respectively.

Due to our assumption that the perturbing quantities decay exponentially as  $\eta \rightarrow \infty$ , (5.23)–(5.28) permit solutions of the form

$$\phi_i^j(\eta \rightarrow \infty; \alpha, \beta, \gamma; R, \theta) = c_i^j e^{\kappa_j \eta}, \quad (5.29)$$

where  $\kappa_j < 0$ , and  $c_i^j$  and  $\kappa_j$  are independent of  $\eta$ . By substituting (5.29) into

(5.23)–(5.28), we find  $c_i^j$  and  $\kappa_j$ :

$$\kappa_1 = \kappa_3 = \frac{W_\infty}{2} - \left[ \left( \frac{W_\infty}{2} \right)^2 + \alpha^2 + \beta^2 - iR\gamma \right]^{1/2}, \quad (5.30)$$

$$\kappa_2 = \kappa_4 = \frac{W_\infty}{2} + \left[ \left( \frac{W_\infty}{2} \right)^2 + \alpha^2 + \beta^2 - iR\gamma \right]^{1/2}, \quad (5.31)$$

$$\kappa_5 = - \left[ \alpha^2 + \beta^2 - \frac{i\alpha \cot \theta}{R} \right]^{1/2}, \quad (5.32)$$

$$\kappa_6 = + \left[ \alpha^2 + \beta^2 - \frac{i\alpha \cot \theta}{R} \right]^{1/2}. \quad (5.33)$$

We take the real parts of the complex square roots to be positive. Only the solutions with  $j = 1, 3$  and  $5$  decay as  $\eta \rightarrow \infty$  so only these are relevant. We find the required coefficients to be

$$\begin{array}{lll} c_1^1 = 1 & c_1^3 = 0 & c_1^5 = i\kappa_5, \\ c_2^1 = \kappa_1 & c_2^3 = 0 & c_2^5 = i\kappa_5^2, \\ c_3^1 = -i/\kappa_1 & c_3^3 = 0 & c_3^5 = 1, \\ c_4^1 = 0 & c_4^3 = 0 & c_4^5 = \frac{1}{R\kappa_5} \left( iR\gamma - \frac{i\alpha \cot \theta}{R} - W_\infty \kappa_5 \right), \\ c_5^1 = 0 & c_5^3 = 1 & c_5^5 = 0, \\ c_6^1 = 0 & c_6^3 = \kappa_3 & c_6^5 = 0. \end{array}$$

Starting from this initial solution, the equations are integrated down towards  $\eta = 0$ .

The first boundary condition (5.22), stipulates that on the surface of the sphere, the value of the perturbation quantities must be zero, so we have

$$\begin{pmatrix} \phi_1(0) \\ \phi_3(0) \\ \phi_5(0) \end{pmatrix} = \begin{pmatrix} \phi_1^1(0) & \phi_1^3(0) & \phi_1^5(0) \\ \phi_3^1(0) & \phi_3^3(0) & \phi_3^5(0) \\ \phi_5^1(0) & \phi_5^3(0) & \phi_5^5(0) \end{pmatrix} \begin{pmatrix} C_1 \\ C_2 \\ C_3 \end{pmatrix} = \begin{pmatrix} 0 \\ 0 \\ 0 \end{pmatrix}$$

for some constant coefficients  $C_{1,2,3}$ . The coefficient matrix must be singular in order

for the solution to be non-trivial, and this condition leads to the dispersion relation,

$$D(\alpha, \beta, \gamma; R, \theta, \tau, \iota) = 0, \quad (5.34)$$

where  $D$  is the determinant of the matrix. This requirement means that in any given configuration, i.e. fixing values for  $R, \theta, \tau$  and  $\iota$ , the value of any of  $\alpha, \beta$  or  $\gamma$  can be deduced if the other two are known.

The code used to find solutions to (5.16)–(5.21) is an amended version of that used by Garrett (2002), based on the code originally developed by Lingwood (1995a) that incorporated routines from Press *et al.* (1992).

### 5.3 Convective stability analysis of stationary vortices

Regions of convective instability are now calculated by fixing the longitudinal disturbance phase velocity,  $\gamma_r/\beta$ , with respect to the sphere surface, and using this to determine  $\alpha$  and  $\beta$ . The non-dimensional speed of the sphere surface is  $\sin \theta$ ; hence the non-dimensional disturbance speed,  $c$ , is given by  $\gamma_r/\beta \sin \theta$ . For this section, we set  $c = 1$ , so that the vortices are stationary with respect to the sphere surface. Using the approach of fixing  $c$ , the dispersion relation (see §1.2) reduces to

$$D(\alpha, \beta, \gamma = c\beta \sin \theta; R, \theta, \tau, \iota) = D(\alpha, \beta; R, \theta, c, \tau, \iota) = 0. \quad (5.35)$$

At high latitudes, travelling vortices with  $c = 0.76$  have been observed experimentally on the rotating sphere by Kobayashi & Arai (1990). Travelling vortices are considered in §5.4.

Figure 5.1 displays typical examples of the form of the spatial branches that govern convective instability, in the complex- $\alpha$  plane. Points on these branches correspond to solutions to (5.35). The case illustrated is that of a still fluid at a latitude of  $\theta = 30^\circ$ . In each case, two branches are visible, referred to as branches 1

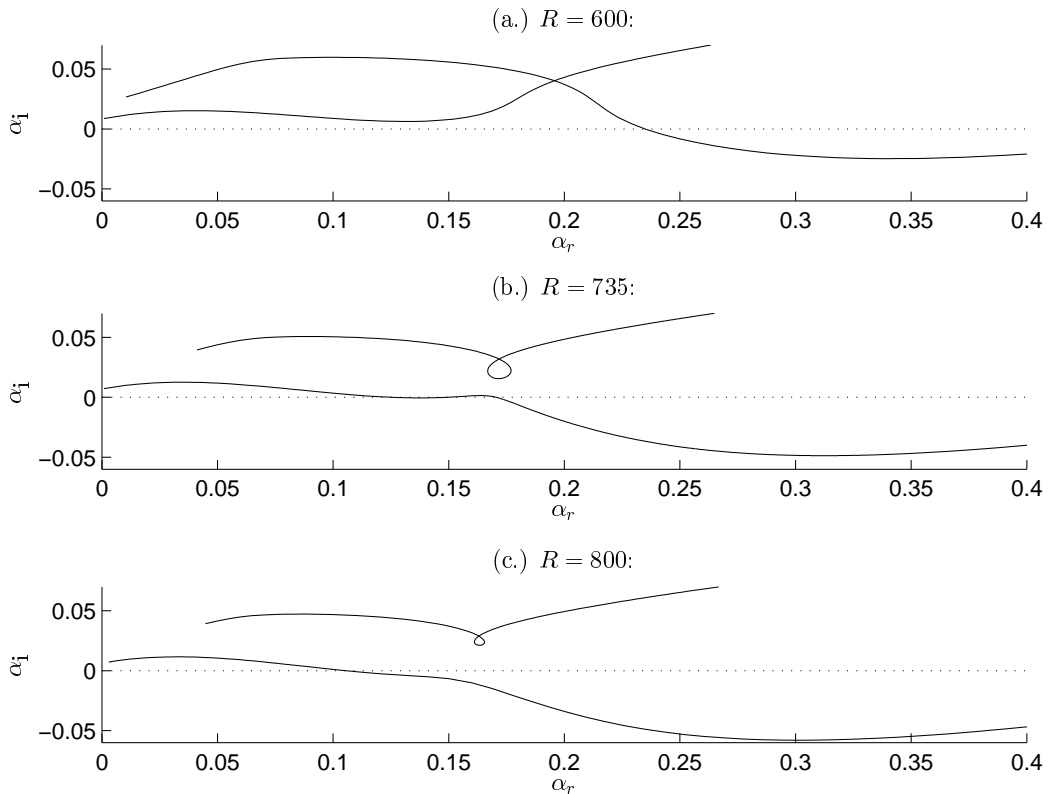


Figure 5.1: Spatial branches at  $\theta = 30^\circ$ ,  $\tau = \nu = 0$ ;  $R = 600, 735, 800$ .

and 2; however, in Figure 5.1a, branch 2 resides entirely above the  $\alpha_r$  axis, and so it does not contribute to the instability. Figures 5.1b and 5.1c show the positions of the branches at successively higher Reynolds numbers. By Figure 5.1b, an exchange of modes has occurred, and what was formerly branch 2 has moved down enough to intersect the  $\alpha_r$  axis, forming a second unstable region, which manifests itself on the neutral curve as the streamline-curvature lobe.

Presented in Figures 5.2–5.10 are neutral-stability curves in the  $(R, \alpha_r)$ - and  $(R, \beta)$ -planes for a representative sample of the parameter space. These curves indicate the points at which the imaginary parts of both  $\alpha$  and  $\gamma$  are equal to zero. The regions enclosed by the curves are convectively unstable. As will be seen from the following figures, these curves typically exhibit two lobes. The upper lobe, which occurs at higher wavenumbers, represents crossflow instability; this is an inviscid effect that arises due to the inflectional nature of the mean velocity profiles. The lower lobe, which occurs at lower wavenumbers, arises due to streamline-curvature instabilities caused by the geometry of the flow and viscous effects. These modes of instability are also referred to as Type I and Type II, respectively. We use the

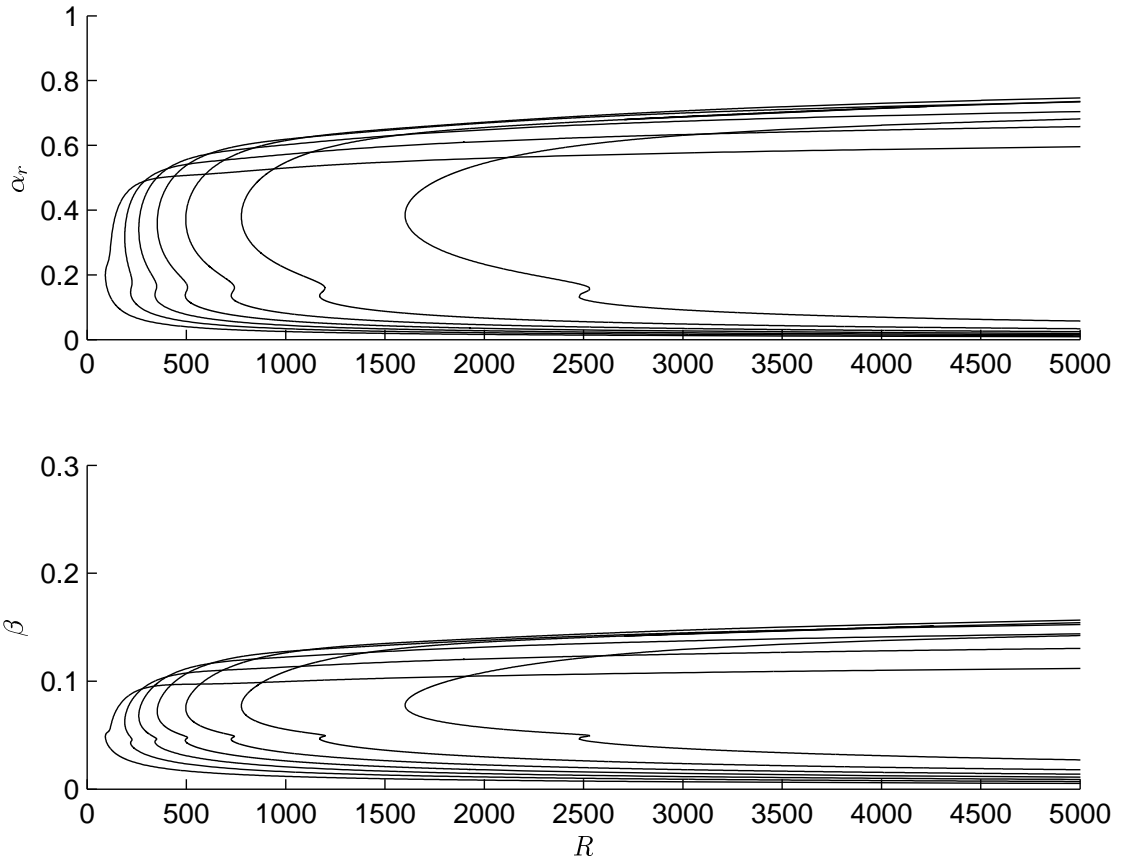


Figure 5.2: Neutral stability curves for  $\alpha_r$  and  $\beta$  at  $\tau = 0$ ,  $\iota = 0$  (still fluid), and  $\theta = 10^\circ$  to  $70^\circ$  in increments of  $10^\circ$  (right to left).

critical Reynolds number,  $R_c(\theta; \iota, \tau; c)$ , as a quantitative measure of the stability of a system. It is the value of  $R$  below which the flow is always stable for a given set of parameters, and is therefore visible as the leftmost point on the curve. In cases where two lobes are present, the one which extends to the smallest Reynolds number (i.e. the one which determines  $R_c$ ) is referred to as the dominant lobe.

The first three Figures, 5.2–5.4, show example cases of zero, positive and negative surface mass-flux, all without forced axial flow, at various latitudes. Figures 5.5–5.7 show the effects of both axial flow and surface mass-flux at a fixed latitude of  $\theta = 10^\circ$ . Figures 5.8–5.10 show the same, but at  $\theta = 50^\circ$ .

Note that the visible range of values on each axis varies based on the parameter set in order to optimally display the data. In Figure 5.7, the restricted range has resulted in the neutral curve not being visible for the extremely stable case of  $(\tau, \iota) = (0.25, -1)$ , since this causes  $R_c$  to exceed 10,000.

In all cases, increased suction exaggerates the two-lobe profile of the curve and

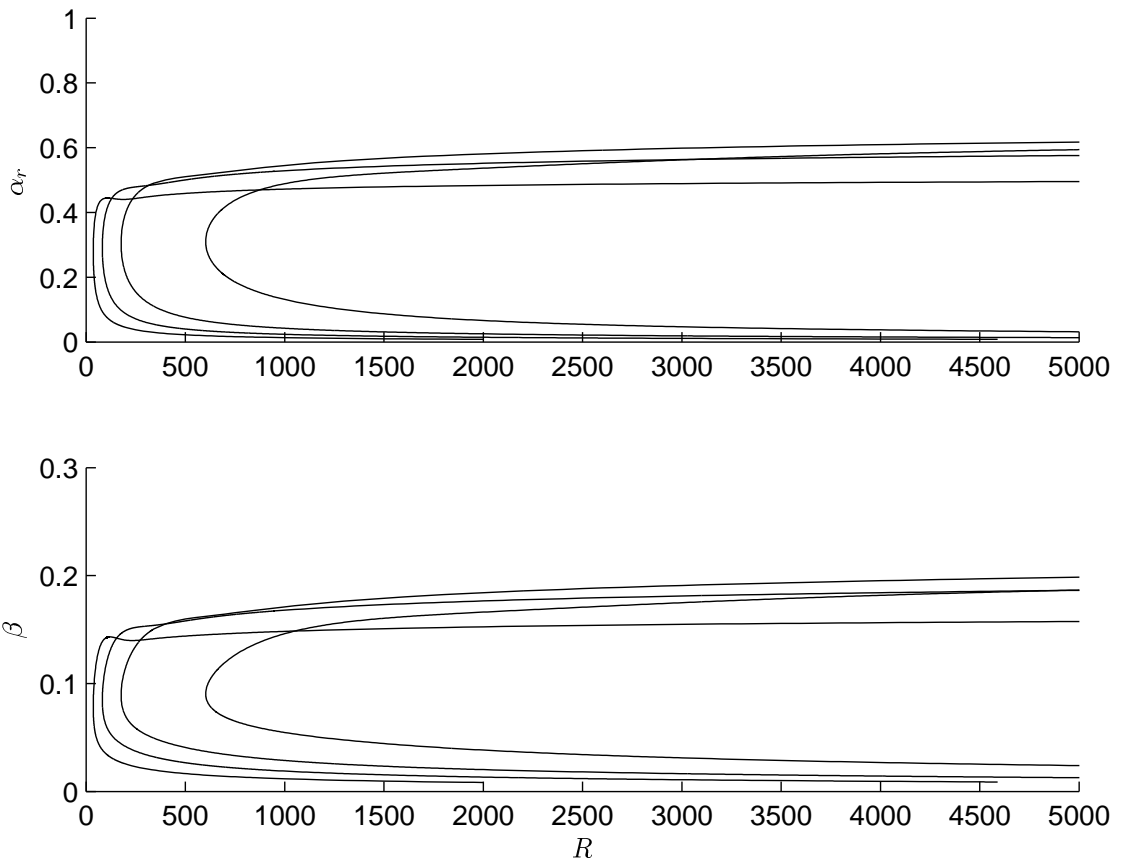


Figure 5.3: Neutral stability curves for  $\alpha_r$  and  $\beta$  at  $\tau = 0$ ,  $\nu = 1.0$ , and  $\theta = 10^\circ, 30^\circ, 50^\circ, 70^\circ$  (right to left).

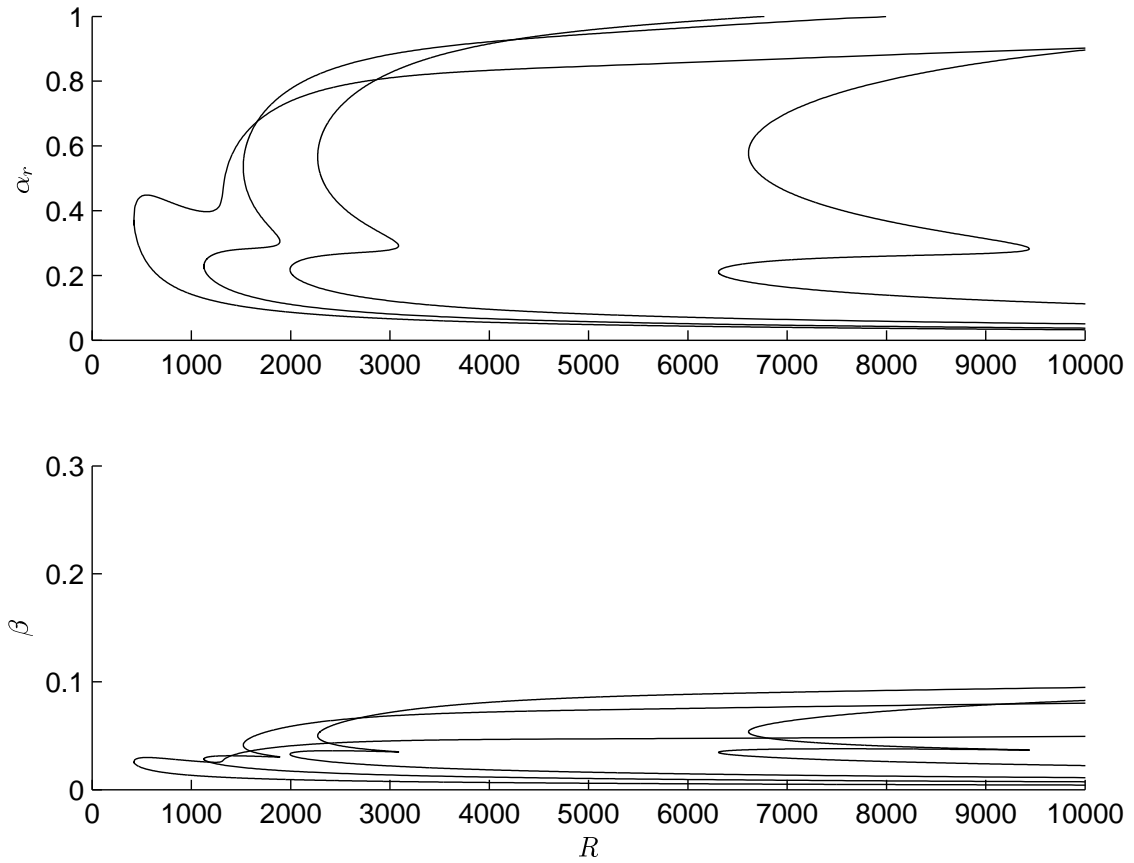


Figure 5.4: Neutral stability curves for  $\alpha_r$  and  $\beta$  at  $\tau = 0$ ,  $\nu = -1.0$ , and  $\theta = 10^\circ, 30^\circ, 50^\circ, 70^\circ$  (right to left).

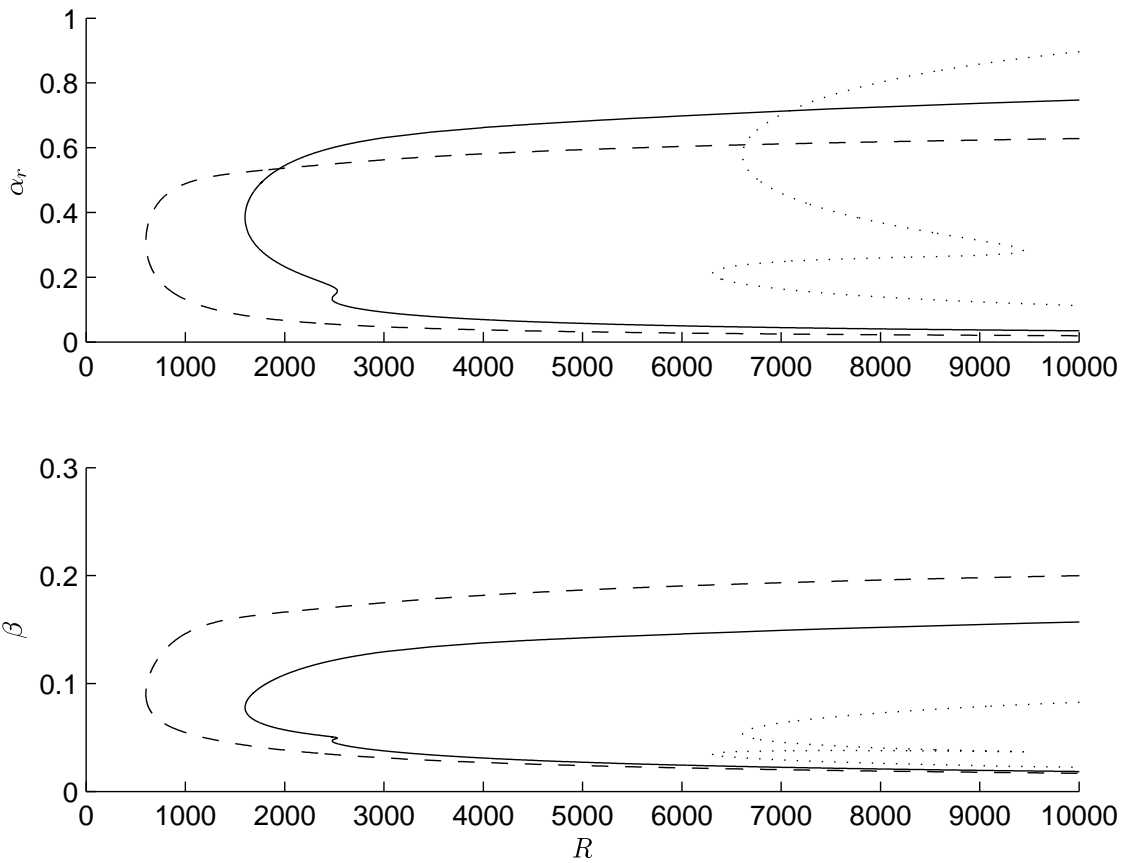


Figure 5.5: Neutral stability curves for  $\alpha_r$  and  $\beta$  at  $\theta = 10^\circ$ ,  $\tau = 0$ , and  $\nu = -1$  ( $\cdots$ ),  $0$  ( $-$ ),  $1$  ( $- -$ ).

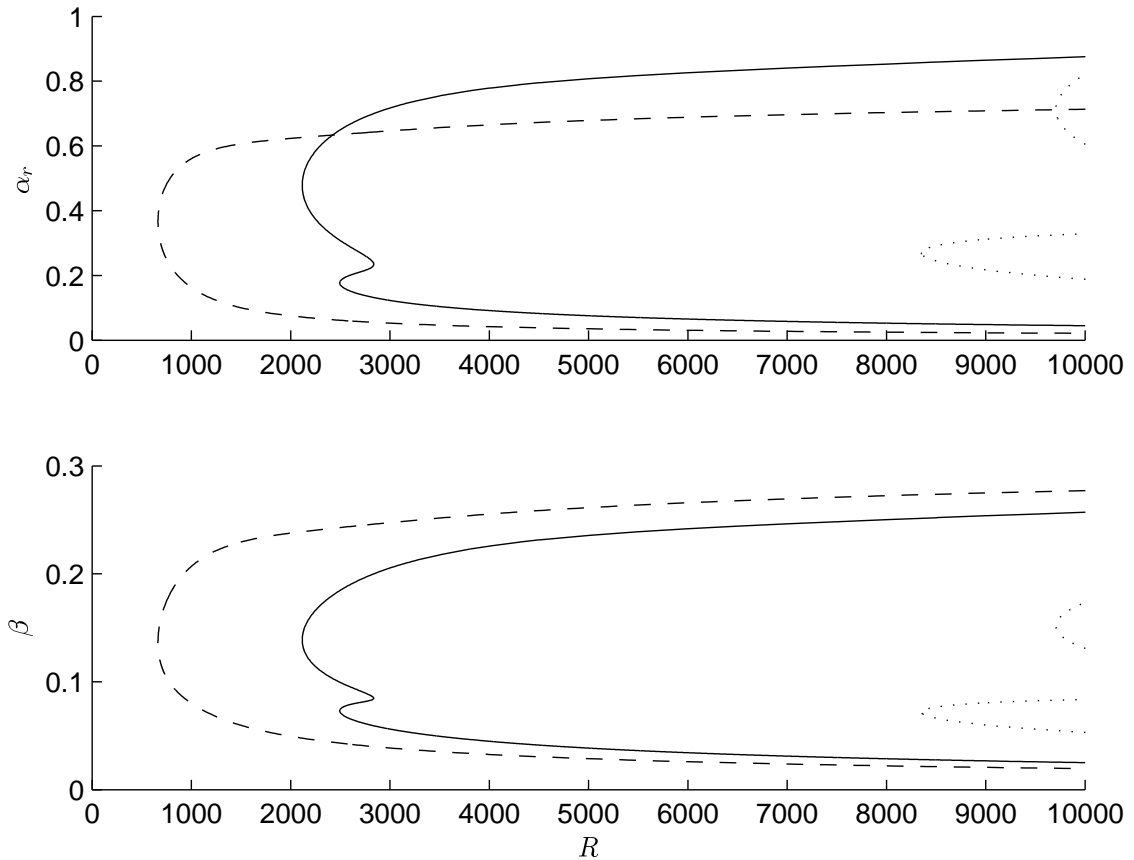


Figure 5.6: Neutral stability curves for  $\alpha_r$  and  $\beta$  at  $\theta = 10^\circ$ ,  $\tau = 0.1$ , and  $\nu = -1$  ( $\cdots$ ),  $0$  ( $-$ ),  $1$  ( $- -$ ).

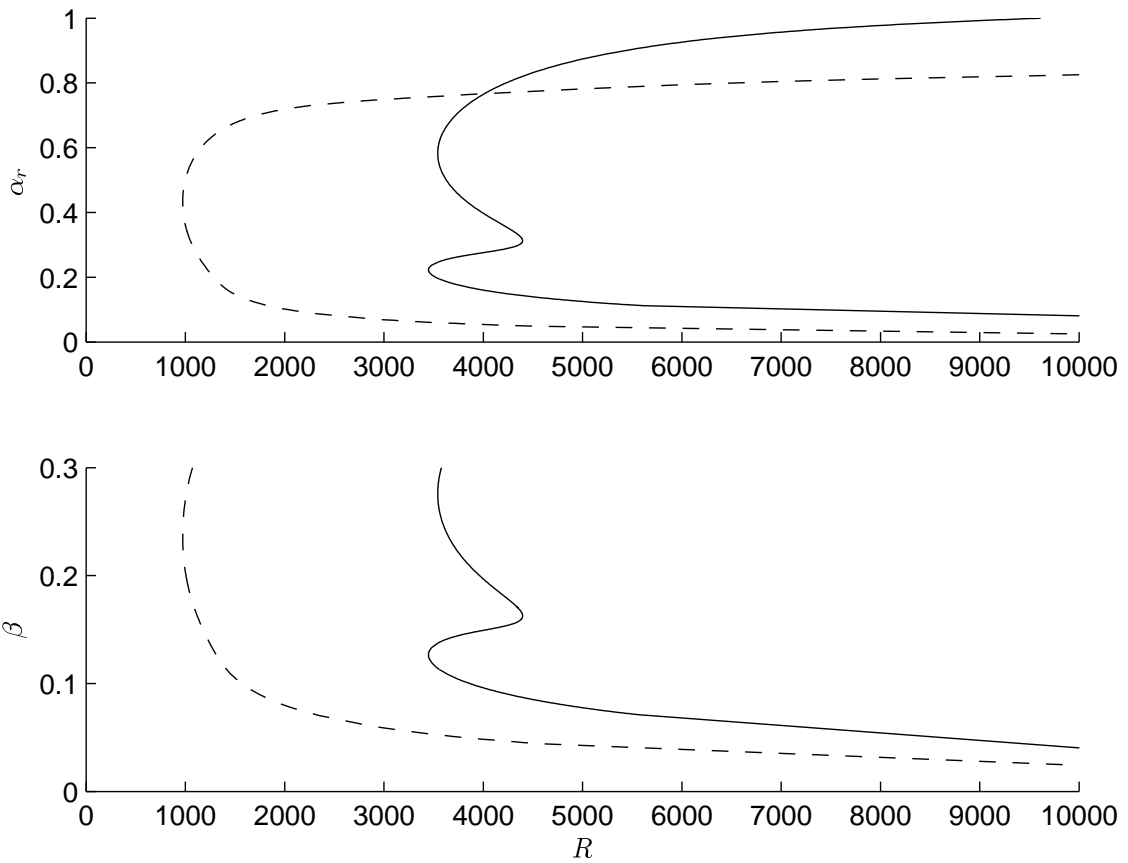


Figure 5.7: Neutral stability curves for  $\alpha_r$  and  $\beta$  at  $\theta = 10^\circ$ ,  $\tau = 0.25$  and  $\iota = 0$  (—), 1 (---), 1 (- -).

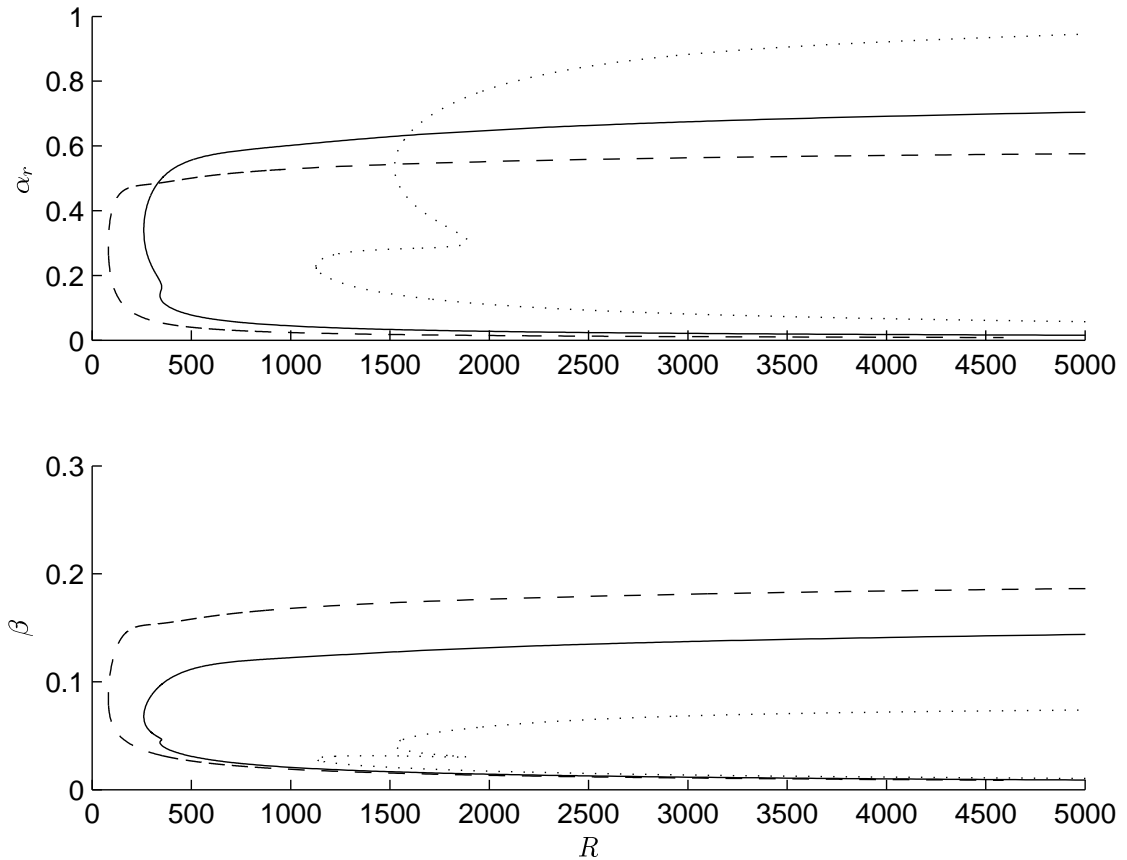


Figure 5.8: Neutral stability curves for  $\alpha_r$  and  $\beta$  at  $\theta = 50^\circ$ ,  $\tau = 0$ , and  $\iota = -1$  ( $\cdots$ ), 0 (—), 1 (---).

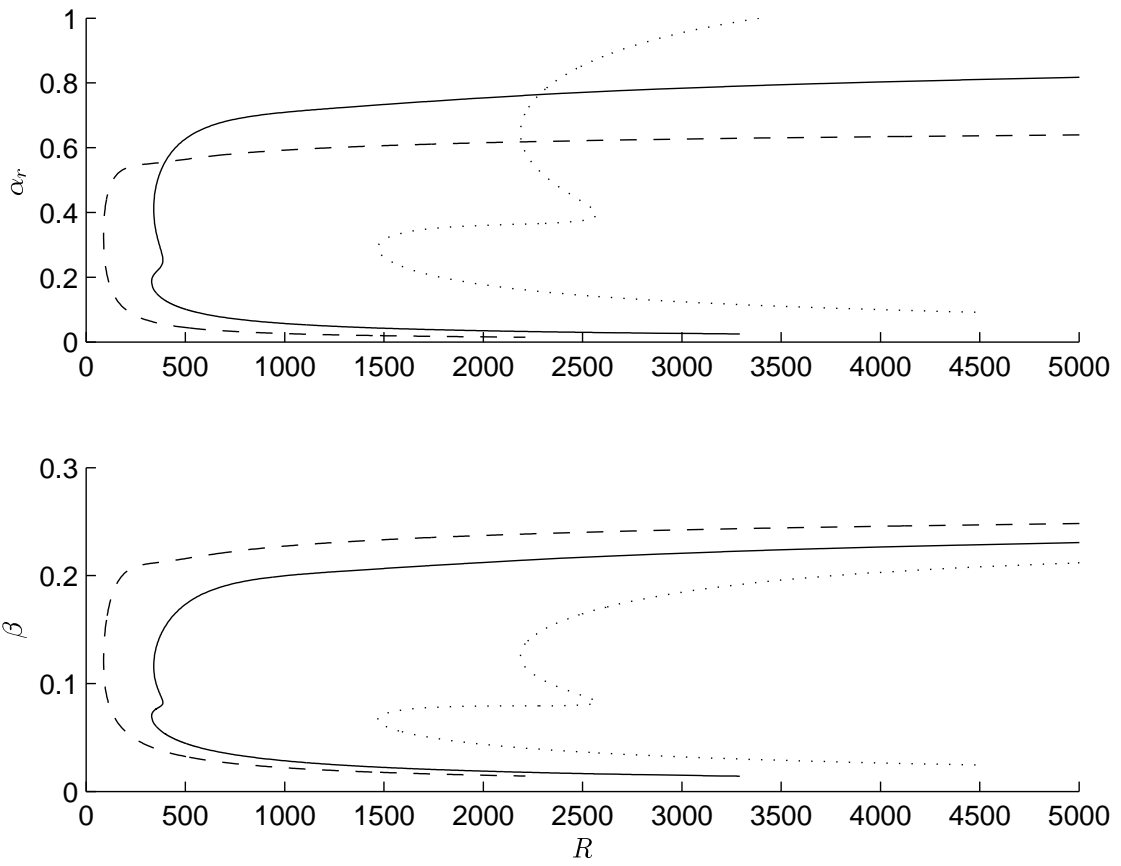


Figure 5.9: Neutral stability curves for  $\alpha_r$  and  $\beta$  at  $\theta = 50^\circ$ ,  $\tau = 0.1$ , and  $\iota = -1$  ( $\cdots$ ),  $0$  ( $-$ ),  $1$  ( $- -$ ).

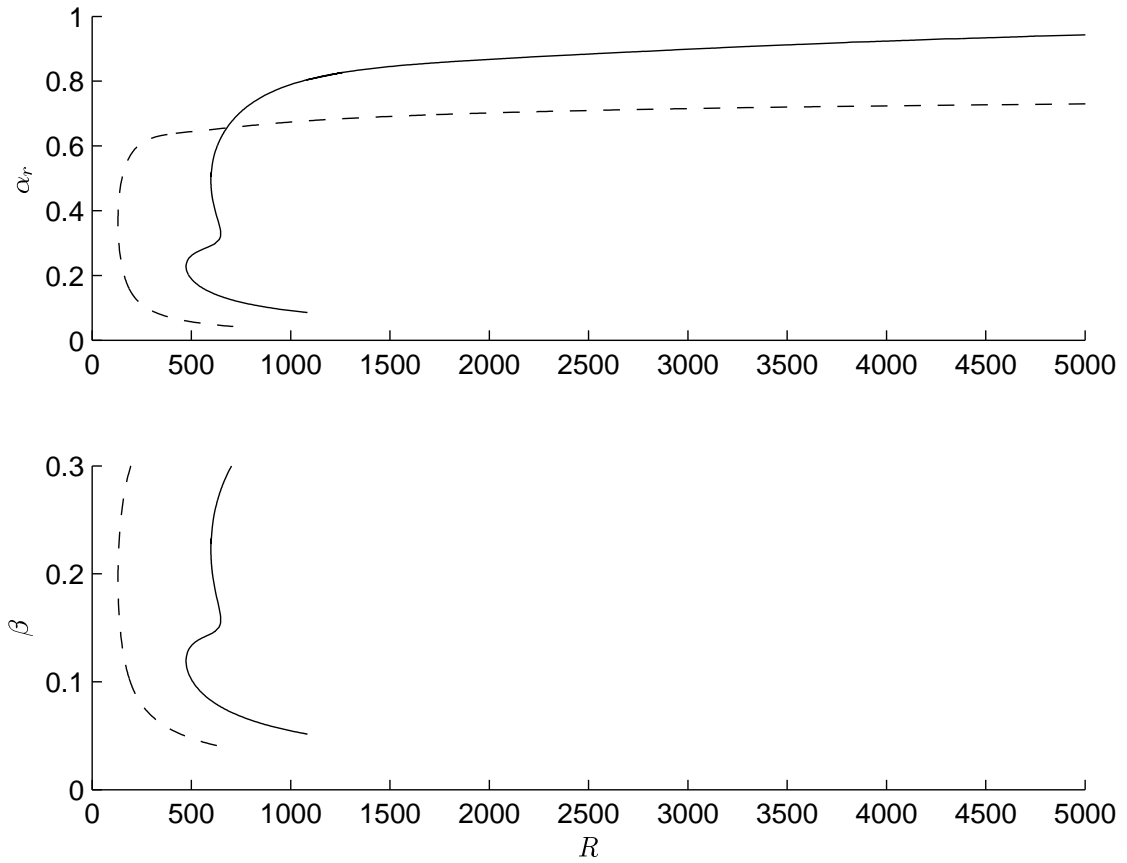


Figure 5.10: Neutral stability curves for  $\alpha_r$  and  $\beta$  at  $\theta = 50^\circ$ ,  $\tau = 0.25$  and  $\iota = 0$  ( $-$ ),  $1$  ( $- -$ ).

produces higher critical Reynolds numbers, and a larger stable region overall. This is to be expected, since suction has been seen to have a stabilising influence in similar boundary-layer flows (see the work by Lingwood (1997c) on rotating disks, for example). Injection has the opposite effect, and we see that the two-lobe form is lost for high magnitudes. The lower, streamline-curvature lobe becomes dominant as suction is increased. It can be seen from the results of Chapters 3 and 4 that suction causes a thinning of the boundary layer; in particular, Figures 3.1–3.3 and 4.1–4.3 demonstrate how the mean velocity profiles become fully developed closer to the sphere surface in the presence of suction. The data also show significantly-reduced streamwise wall jets as suction is increased. Physically, these effects are associated with increased stability, so it is sensible that suction is seen to delay the onset of instability.

Increasing  $\tau$  increases the relative importance of the Type II lobe. It also moves both the upper and lower branches to larger wavenumbers for large  $R$ , but the effect on the upper branch is much greater. This has the effect of allowing convective instability to exist over a wider range of wavenumbers.

Although increasing  $\tau$  typically raises the critical Reynolds number (and therefore promotes stability), small magnitudes of forced axial flow are in fact found to decrease the critical Reynolds number of the Type II lobe (compare the middle rows of Tables 5.1 and 5.2). At high latitudes (with the precise value depending on  $\iota$ ), where the Type II lobe is dominant, this results in a lower value for  $R_c$  overall. To give a specific example: if we fix  $\iota$  and  $\theta$  at 0.0 and 70°, respectively, and allow  $\tau$  to increase from 0.00 to 0.25,  $R_c(\tau)$  initially decreases until it attains a minimum at  $\tau = 0.09$ . It is not until  $\tau$  reaches 0.20 that  $R_c$  exceeds  $R_c(0)$  (see Figure 5.11). Thus, in these cases, moderate axial flow is seen not only to broaden the unstable range of wavenumbers, but also to cause a small decrease in  $R_c$ , making the model more susceptible to instability. Further increasing  $\tau$ , however, increases  $R_c$ , and the behaviour becomes typical of that seen at lower latitudes. The threshold value of  $\tau$ , above which  $R_c$  surpasses its value at  $\tau = 0$ , is dependent on the latitude and  $\iota$ .

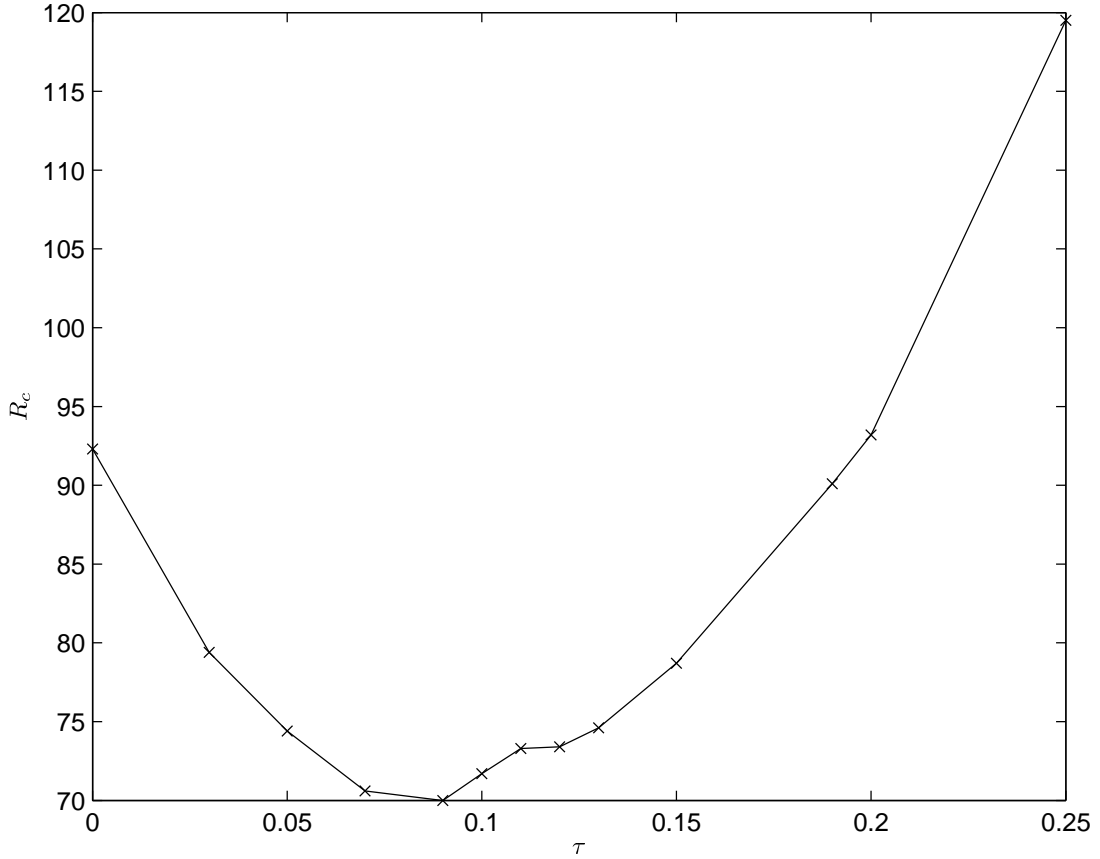


Figure 5.11: Illustration of one case ( $\theta = 70^\circ$ ,  $\iota = 0.0$ ) where small magnitudes of axial flow decrease  $R_c$  relative to the case of  $\tau = 0.00$ .

Both surface mass injection and suction reduce the magnitude of this effect, and it is not observed at all with strong suction. The significance of this effect is questionable, since it only occurs at high latitudes, where the critical Reynolds numbers are low and are more sensitive to the parallel-flow approximation.

We see that, in all cases, changes in both  $\iota$  and  $\tau$  have a significantly more pronounced effect on the upper branches of the neutral curves. Compared to that of the upper branch, the position of the lower branch appears to be less influenced by changes in any of  $\theta$ ,  $\tau$  and  $\iota$ , for large  $R$ . It may be interesting to examine the implications of this by performing an asymptotic analysis at a later date.

Tables 5.1–5.3 show the computed critical Reynolds numbers for a representative range of parameters. Where the neutral curve has two lobes, the critical  $R$  for the crossflow mode is presented first, and the value for the streamline-curvature mode is given in parentheses. Whichever value represents the dominant lobe is given in bold text. A dash in the table indicates a combination of parameter values for which no

$\iota$	$\theta$			
	10°	30°	50°	70°
-1.0	6610.6 ( <b>6309.1</b> )	2272.4 ( <b>1993.5</b> )	1523.0 ( <b>1127.0</b> )	( <b>421.2</b> )
0.0	<b>1601.5</b> (2478.0)	<b>497.2</b> (726.0)	<b>260.7</b> (341.8)	( <b>92.3</b> )
1.0	( <b>602.7</b> )	( <b>176.9</b> )	( <b>82.0</b> )	( <b>36.3</b> )

Table 5.1: Critical Reynolds numbers,  $R_c$ , for  $\tau = 0.00$

$\iota$	$\theta$			
	10°	30°	50°	70°
-1.0	9705.7 ( <b>8350.7</b> )	-	2187.4 ( <b>1469.4</b> )	-
0.0	<b>2117.0</b> (2494.6)	<b>655.6</b> (724.4)	340.9 ( <b>329.9</b> )	( <b>71.7</b> )
1.0	( <b>664.2</b> )	( <b>193.4</b> )	( <b>88.0</b> )	( <b>37.4</b> )

Table 5.2: Critical Reynolds numbers,  $R_c$ , for  $\tau = 0.10$

data could be obtained; these usually correspond to extremes of one or more of the parameters, where numerical instabilities arise in the solution code.

Figure 5.12 examines in detail the case of  $\theta = 30^\circ$ , showing the behaviour of  $R_c$  as  $\tau$  and  $\iota$  are varied. It is clear that the stabilising effect of increasing the rate of axial flow is greater in the presence of suction, and correspondingly, that positive mass injection reduces its effect. The figure also illustrates that  $R_c$  is increased significantly more by suction than it is reduced by the same magnitude of injection. This conclusion was also reached by Lingwood (1997c) and Lingwood & Garrett (2011) for the class of general BEK flows.

The number of spiral vortices occurring on the sphere at the onset of convective instability, and the angle they make with a circle parallel to the equator, have been measured by Kohama & Kobayashi (1983). They observe that the angle,  $\epsilon$ , is always approximately  $14^\circ$ , but the number of vortices,  $n$ , increases with the rotation rate (this is equivalent to increasing with  $R$ , in our formulation) and tends towards approximately 32. These measurements are provided for the still-fluid case only; for

$\iota$	$\theta$			
	10°	30°	50°	70°
-1.0	-	-	-	-
0.0	3541.6 ( <b>3448.2</b> )	1116.0 ( <b>1010.0</b> )	598.5 ( <b>473.4</b> )	( <b>119.5</b> )
1.0	( <b>973.3</b> )	( <b>285.3</b> )	( <b>130.7</b> )	( <b>55.9</b> )

Table 5.3: Critical Reynolds numbers,  $R_c$ , for  $\tau = 0.25$

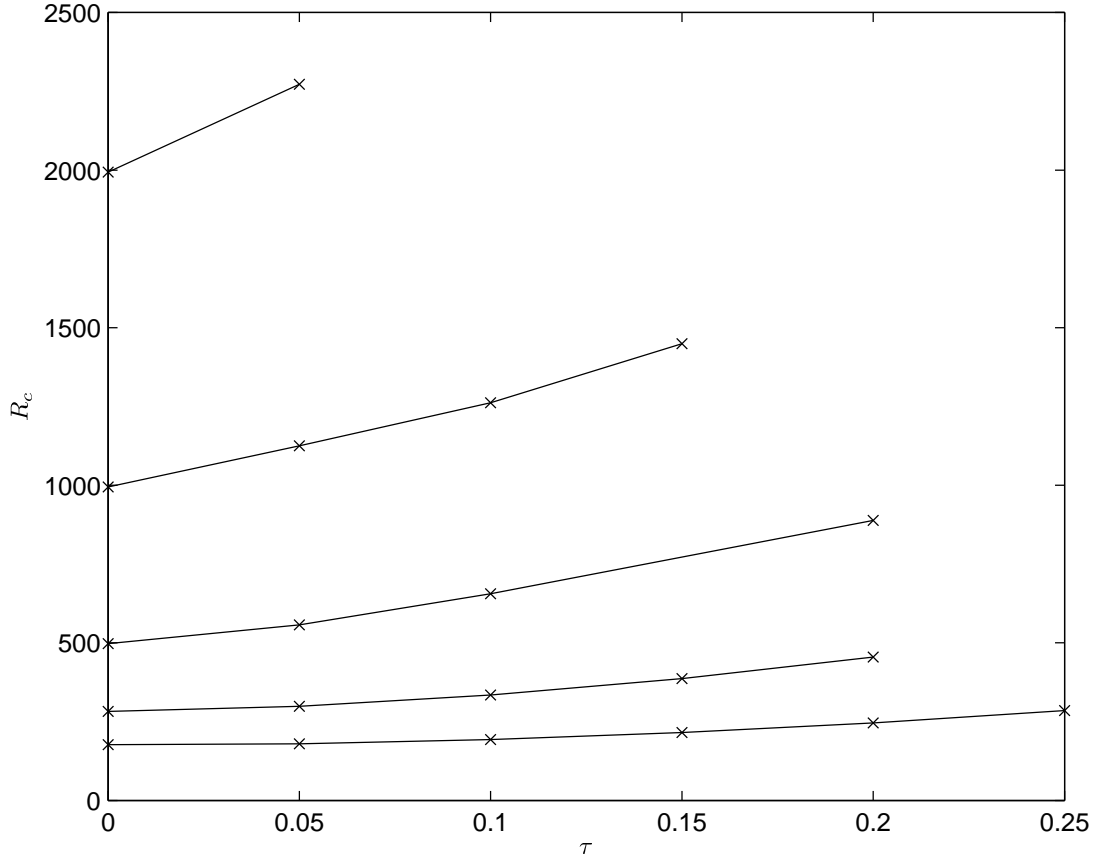


Figure 5.12: Critical Reynolds numbers for the onset of convective instability at  $\theta = 30^\circ$ , for  $\nu = -1, -0.5, 0, 0.5, 1$  (top to bottom).

non-zero axial flow or mass flux, it does not appear that these quantities have yet been experimentally measured. The number of vortices is related to the azimuthal wavenumber  $\beta$ , and is equivalent to the number of complete cycles of the disturbance around the azimuth. It is given by  $n = R\beta \sin \theta$ . Note that this definition does not take into account the fact that the vortices are observed to grow spatially with latitude, and it may not reliably predict the true value of  $n$ , but it is still useful as a quantitative measure of how the number is affected by changing the parameters  $\nu$  and  $\tau$ . The vortex angle is given by  $\epsilon = \tan^{-1}(\beta/\alpha_r)$ .

For each entry in Tables 5.1–5.3, the predicted number of vortices and their angle has been calculated at the critical point of the neutral curve, and these are presented in Tables 5.4–5.6. As with the tables of critical Reynolds numbers, entries corresponding to the dominant lobe are given in bold text. Where  $R_c$  could not be determined in the previous analysis, we are unable to calculate the critical values of  $n$  and  $\epsilon$ , and entries corresponding to these parameter sets are marked with ‘-’.

Number of vortices:				
$\iota$	$\theta$			
	10°	30°	50°	70°
-1.0	62 ( <b>38</b> )	57 ( <b>33</b> )	48 ( <b>24</b> )	( <b>10</b> )
0.0	<b>22</b> (20)	<b>19</b> (17)	<b>14</b> (12)	( <b>4</b> )
1.0	( <b>10</b> )	( <b>8</b> )	( <b>5</b> )	( <b>3</b> )

Angle of vortices:				
$\iota$	$\theta$			
	10°	30°	50°	70°
-1.0	5.3° ( <b>9.3°</b> )	5.1° ( <b>8.6°</b> )	4.4° ( <b>7.1°</b> )	( <b>3.9°</b> )
0.0	<b>11.4°</b> (19.6°)	<b>11.4°</b> (18.9°)	<b>11.2°</b> (17.4°)	( <b>13.7°</b> )
1.0	( <b>16.2°</b> )	( <b>16.6°</b> )	( <b>16.2°</b> )	( <b>15.7°</b> )

Table 5.4: Number and angle of vortices for  $\tau = 0.00$

Number of vortices:				
$\iota$	$\theta$			
	10°	30°	50°	70°
-1.0	258 ( <b>103</b> )	-	210 ( <b>75</b> )	-
0.0	<b>51</b> (32)	<b>43</b> (26)	31 ( <b>18</b> )	( <b>6</b> )
1.0	( <b>16</b> )	( <b>13</b> )	( <b>8</b> )	( <b>4</b> )

Angle of vortices:				
$\iota$	$\theta$			
	10°	30°	50°	70°
-1.0	12.0° ( <b>14.9°</b> )	-	11.0° ( <b>12.9°</b> )	-
0.0	<b>16.1°</b> (22.4°)	<b>16.0°</b> (21.8°)	15.7° ( <b>20.5°</b> )	( <b>16.7°</b> )
1.0	( <b>20.4°</b> )	( <b>20.4°</b> )	( <b>20.2°</b> )	( <b>19.5°</b> )

Table 5.5: Number and angle of vortices for  $\tau = 0.10$

Number of vortices:				
$\iota$	$\theta$			
	10°	30°	50°	70°
-1.0	-	-	-	-
0.0	169 ( <b>76</b> )	-	102 ( <b>44</b> )	( <b>17</b> )
1.0	( <b>40</b> )	( <b>32</b> )	( <b>20</b> )	( <b>9</b> )

Angle of vortices:				
$\iota$	$\theta$			
	10°	30°	50°	70°
-1.0	-	-	-	-
0.0	25.3° ( <b>29.6°</b> )	-	24.3° ( <b>27.6°</b> )	( <b>24.5°</b> )
1.0	( <b>28.7°</b> )	( <b>28.4°</b> )	( <b>28.0°</b> )	( <b>26.8°</b> )

Table 5.6: Number and angle of vortices for  $\tau = 0.25$

In the still-fluid case ( $\tau = \iota = 0$ ), we find that the vortex angle at the onset of the crossflow mode is roughly independent of  $\theta$ . This is consistent with the experimental observations of Kohama & Kobayashi (1983), who report a constant angle of approximately  $14^\circ$ . The results presented in Table 5.4 also show close agreement with the results of Malik (1985), who calculates the vortex angles on the *rotating disk* at the onset of instability to be  $11.4^\circ$  and  $19.5^\circ$  for the crossflow and streamline-curvature modes, respectively.

Beyond this, we see that surface suction has the effect of increasing the number of vortices and shallowing their angle, while injection decreases  $n$  and steepens  $\epsilon$ . As the magnitude of axial flow increases, the number of vortices is predicted to increase, and the vortex angle to become steeper. These observations are in agreement with Garrett (2002); however, there is currently no experimental data for  $\tau$  and  $\iota \neq 0$  for comparison.

## 5.4 Convective stability analysis of non-stationary vortices

We now consider vortices which travel at different speeds relative to the sphere surface,  $c \neq 1$ . We do this by fixing  $c$  at certain values and then taking the same approach as used in §5.3: marching through  $\beta$  and  $R$  to map spatial branches in the complex- $\alpha$  plane. The points at which these branches intersect the real axis represent points of neutral stability, and when measured at various  $R$ , they provide the data used to produce a neutral curve. This method is introduced as *method-2* by Garrett (2010b), for the rotating-disk boundary layer, and is subsequently applied to rotating spheres in Garrett (2010c).

Figures 5.13–5.16 show examples of neutral-stability curves obtained for  $\iota = 0$  at a range of  $c$ . They show good agreement with those of Garrett (2010c).

Figures 5.17–5.20 show examples of neutral-stability curves obtained with no forced axial flow, but with non-zero  $\iota$ . As before, surface suction has a stabilising

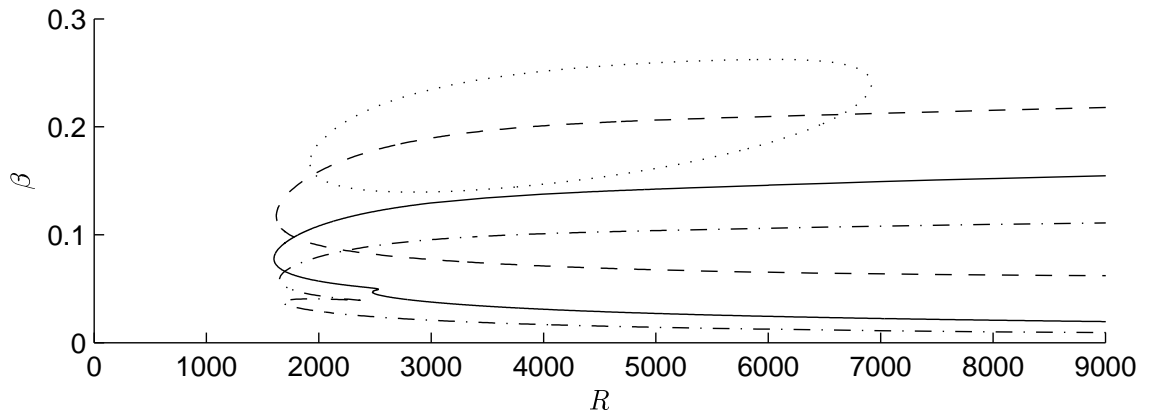
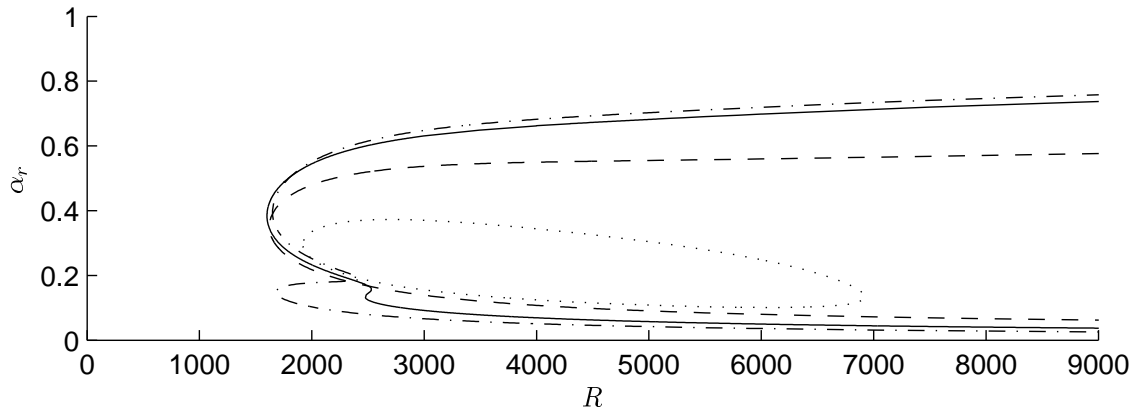


Figure 5.13: Neutral stability curves for  $\alpha_r$  and  $\beta$  at  $\theta = 10^\circ$ ,  $\tau = 0$ ,  $\iota = 0$ , and  $c = 0.7$  ( $\cdots$ ), 0.8 ( $- -$ ), 1 ( $-$ ), 1.2 ( $\cdot -$ ).

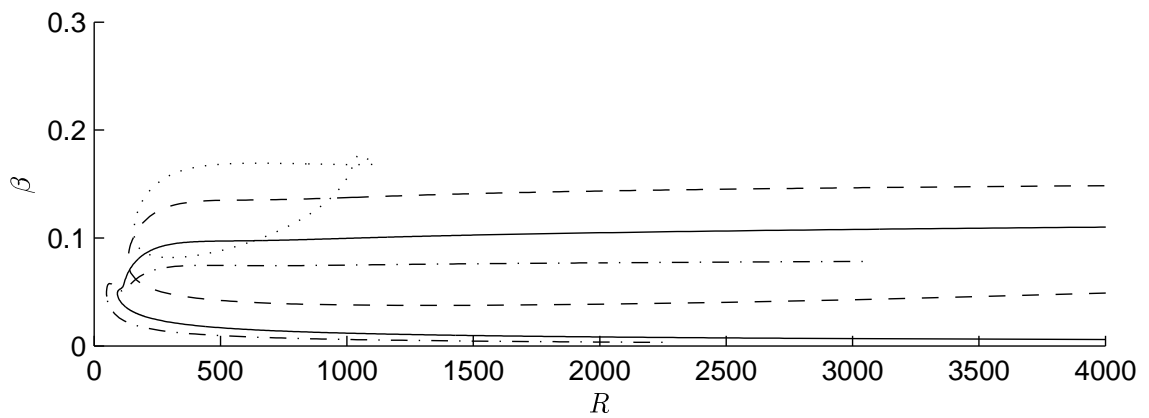
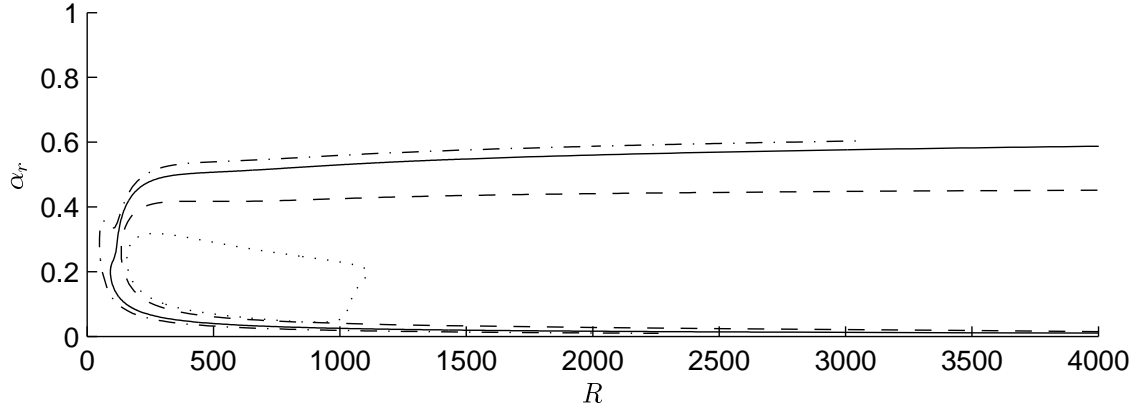


Figure 5.14: Neutral stability curves for  $\alpha_r$  and  $\beta$  at  $\theta = 70^\circ$ ,  $\tau = 0$ ,  $\iota = 0$ , and  $c = 0.7$  ( $\cdots$ ), 0.8 ( $- -$ ), 1 ( $-$ ), 1.2 ( $\cdot -$ ).

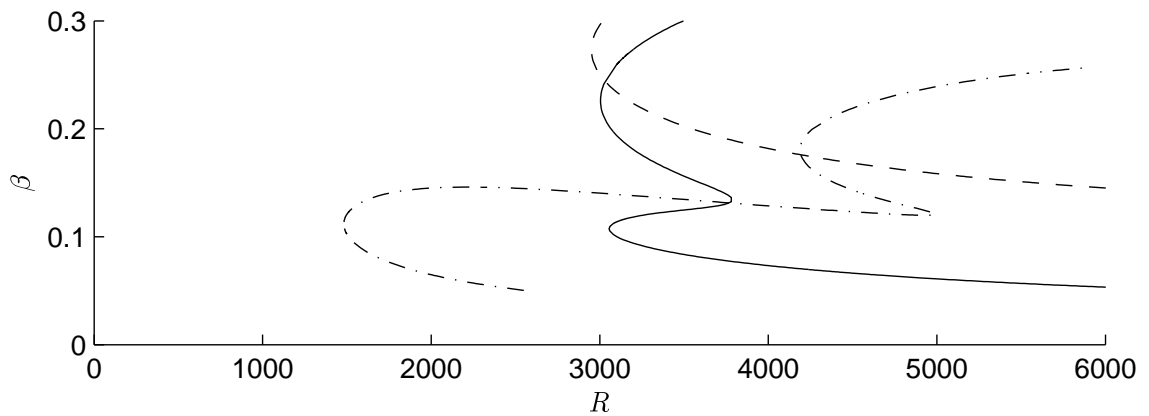
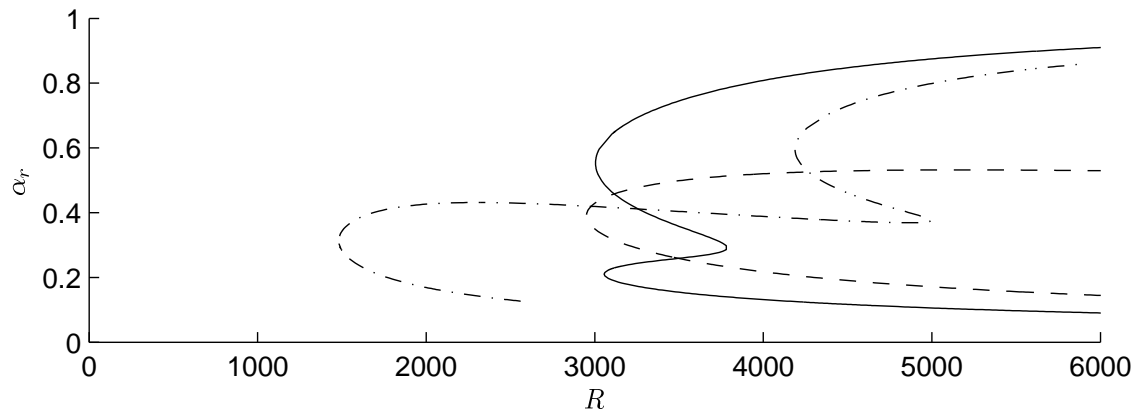


Figure 5.15: Neutral stability curves for  $\alpha_r$  and  $\beta$  at  $\theta = 10^\circ$ ,  $\tau = 0.2$ ,  $\iota = 0$ , and  $c = 0.8$  (- -), 1 (-), 1.2 ( $\cdot$  -).

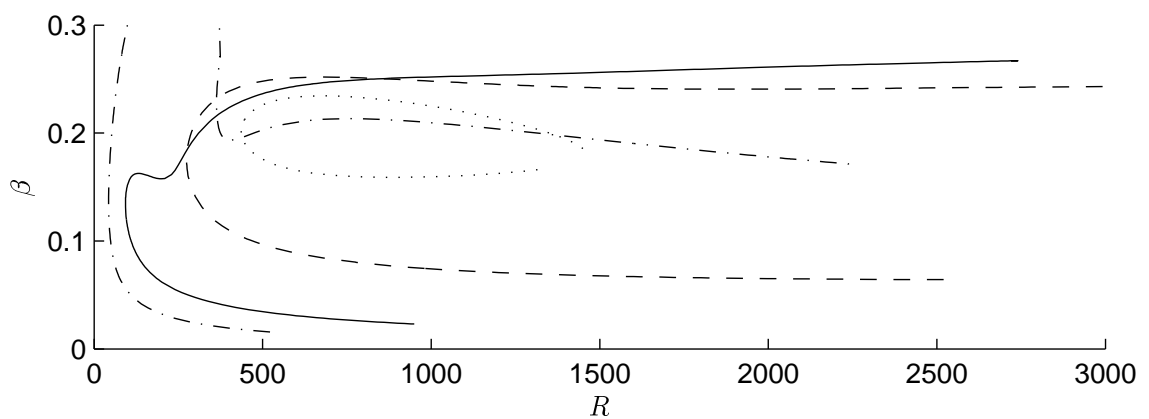
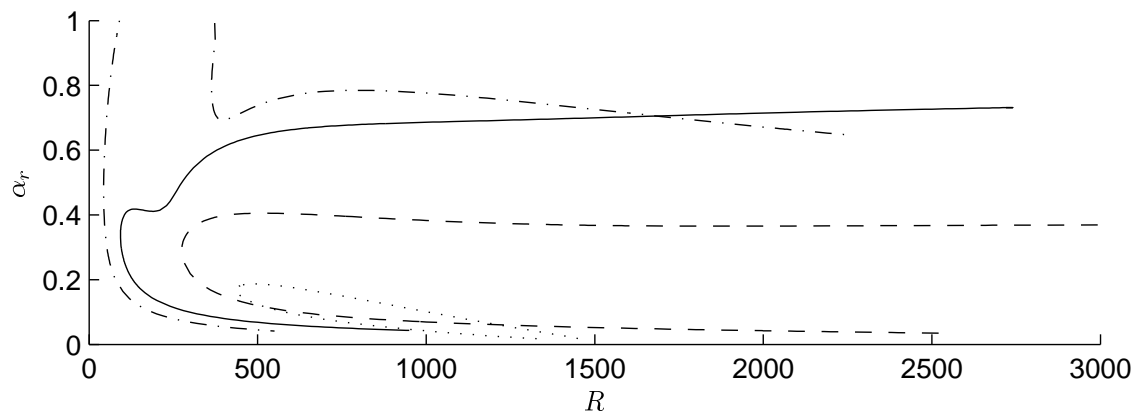


Figure 5.16: Neutral stability curves for  $\alpha_r$  and  $\beta$  at  $\theta = 70^\circ$ ,  $\tau = 0.2$ ,  $\iota = 0$ , and  $c = 0.7$  ( $\cdot$   $\cdot$   $\cdot$ ), 0.8 (- -), 1 (-), 1.2 ( $\cdot$  -).

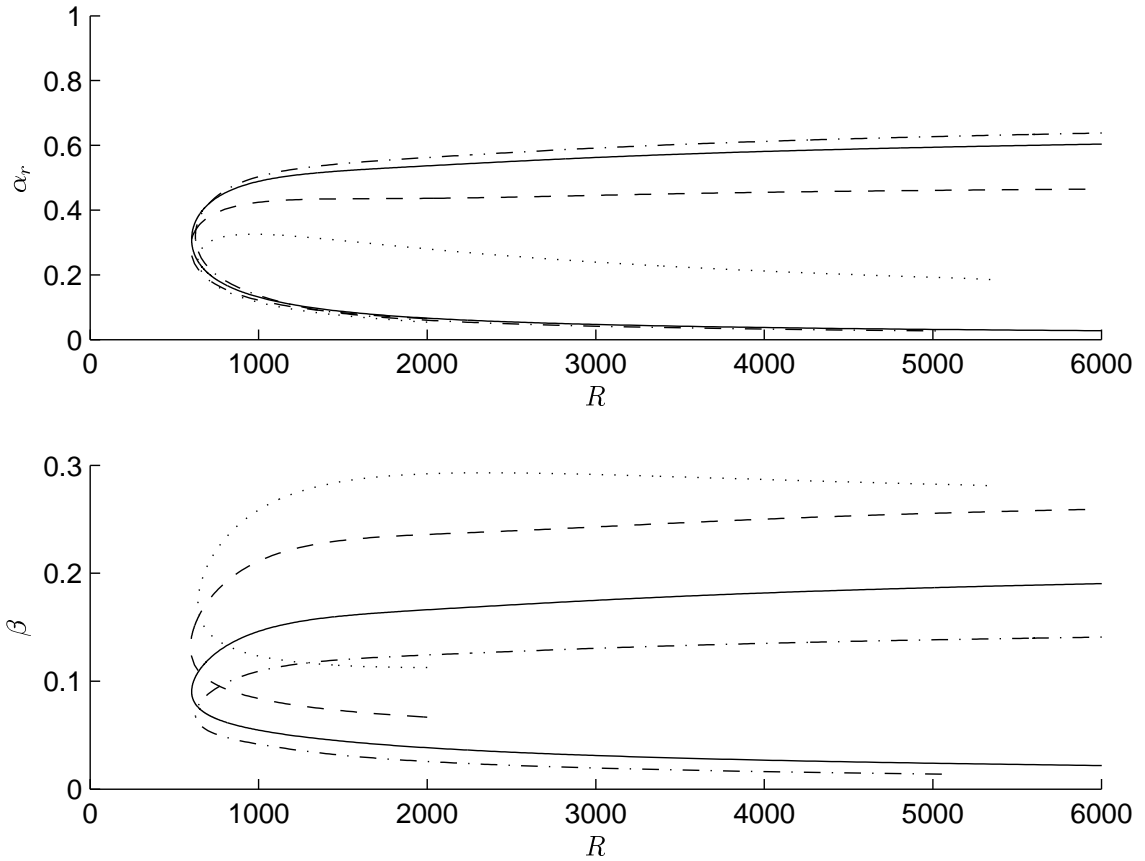


Figure 5.17: Neutral stability curves for  $\alpha_r$  and  $\beta$  at  $\theta = 10^\circ$ ,  $\tau = 0$ ,  $\nu = 1$ , and  $c = 0.7$  ( $\cdots$ ), 0.8 ( $- -$ ), 1 ( $-$ ), 1.2 ( $\cdot -$ ).

effect, increasing the critical Reynolds numbers for all parameter values. It also exaggerates the two-lobe profile of the curve. We see that the lobe corresponding to the streamline-curvature mode of instability is affected more than the crossflow lobe (compare Figures 5.13 and 5.19, for example). The crossflow lobe for  $c = 0.8$  appears to be the least affected by surface suction. Once again, surface mass injection has the effect of decreasing the critical Reynolds numbers for all parameter values.

Figures 5.21–5.22 show examples of neutral-stability curves with both forced axial flow and non-zero  $\nu$ . We see that for large positive  $\nu$ , increasing the magnitude of forced axial flow has only a modest effect on  $R_c$ . However, it broadens the range of wavenumbers over which convective instability is predicted. This effect was observed in §5.3, but we now observe that the magnitude of the distortion is highly dependent on the vortex speed, with greater effects apparent for systems with large  $c$ ; there is very little broadening of the wavenumber range in the slow case of  $c = 0.7$ .

Although only the neutral curves for selected combinations of parameter values

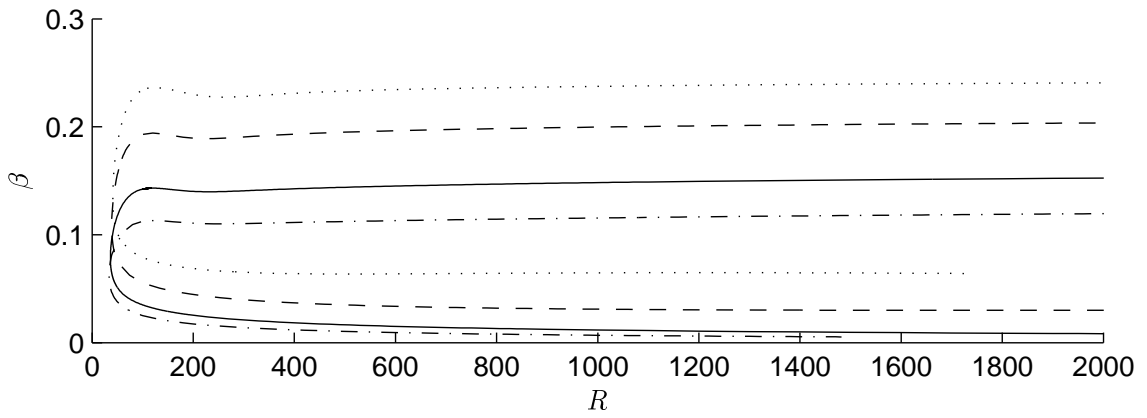
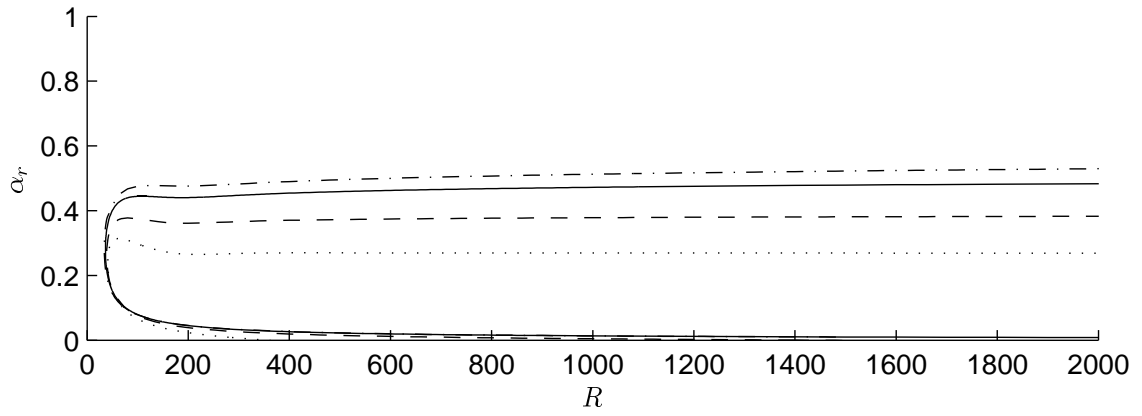


Figure 5.18: Neutral stability curves for  $\alpha_r$  and  $\beta$  at  $\theta = 70^\circ$ ,  $\tau = 0$ ,  $\iota = 1$ , and  $c = 0.7$  ( $\cdots$ ), 0.8 ( $- -$ ), 1 ( $-$ ), 1.2 ( $\cdot -$ ).

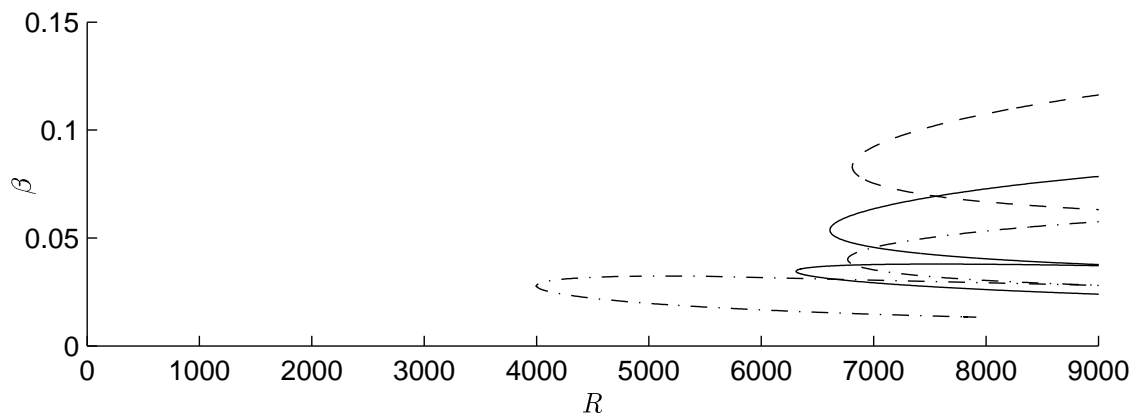
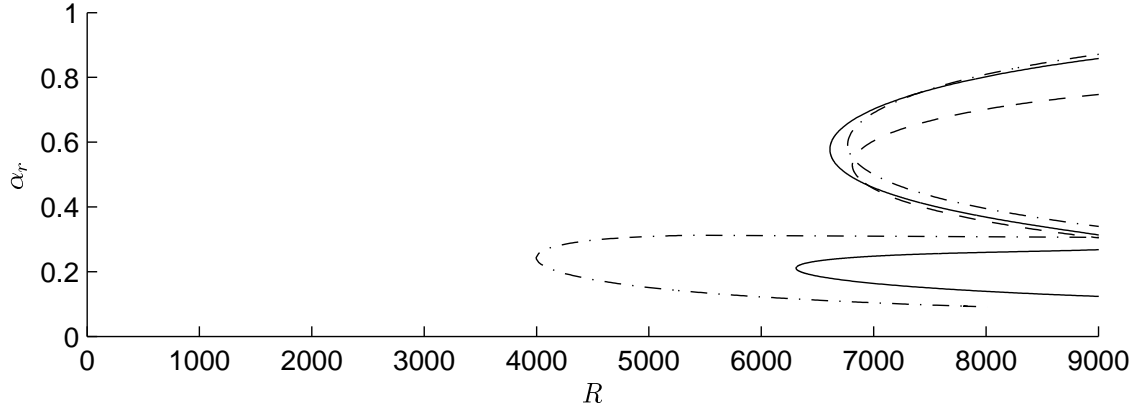


Figure 5.19: Neutral stability curves for  $\alpha_r$  and  $\beta$  at  $\theta = 10^\circ$ ,  $\tau = 0$ ,  $\iota = -1$ , and  $c = 0.7$  ( $\cdots$ ), 0.8 ( $- -$ ), 1 ( $-$ ), 1.2 ( $\cdot -$ ).

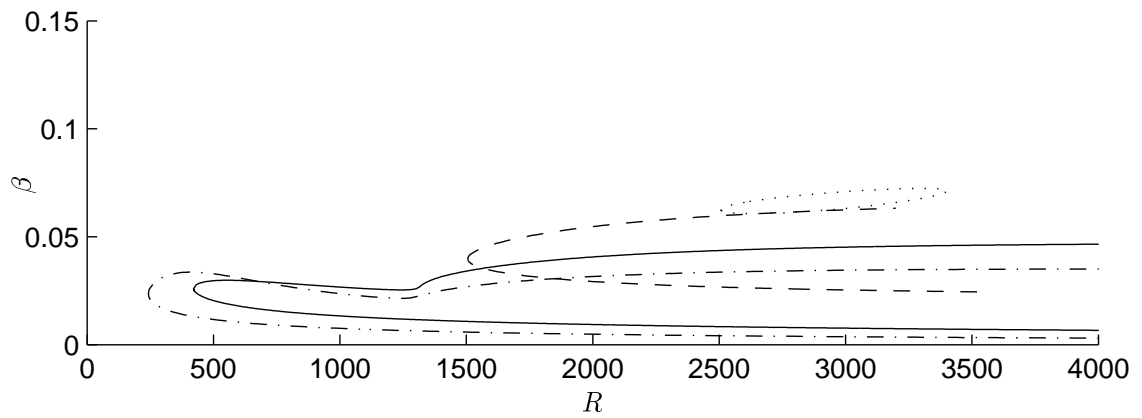
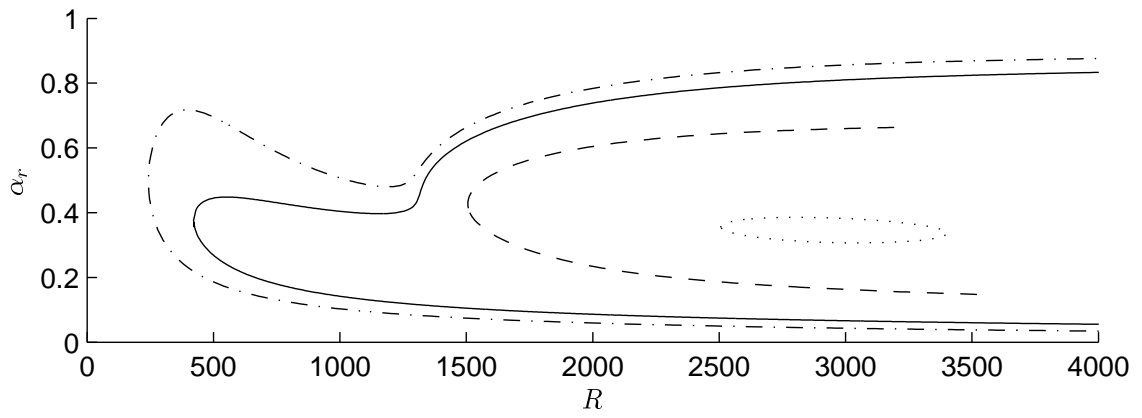


Figure 5.20: Neutral stability curves for  $\alpha_r$  and  $\beta$  at  $\theta = 70^\circ$ ,  $\tau = 0$ ,  $\iota = -1$ , and  $c = 0.7$  ( $\cdots$ ),  $0.8$  ( $- -$ ),  $1$  ( $-$ ),  $1.2$  ( $\cdot -$ ).

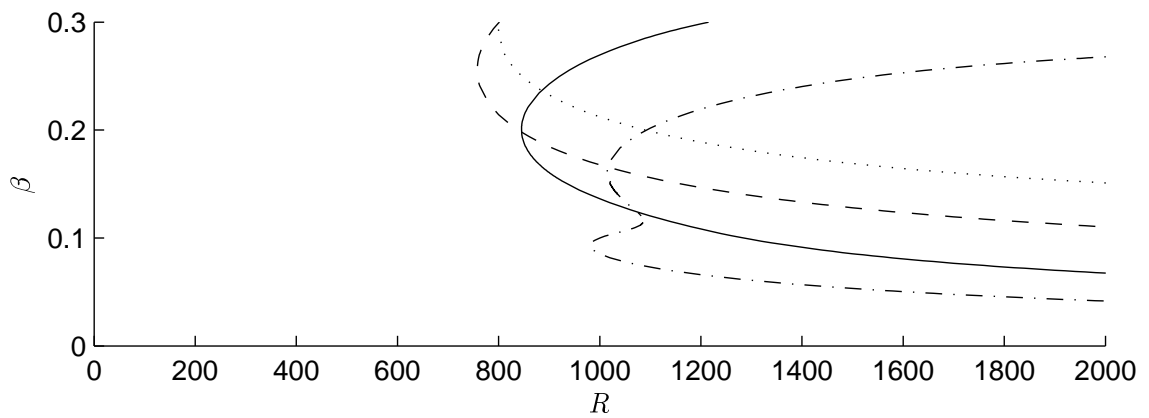
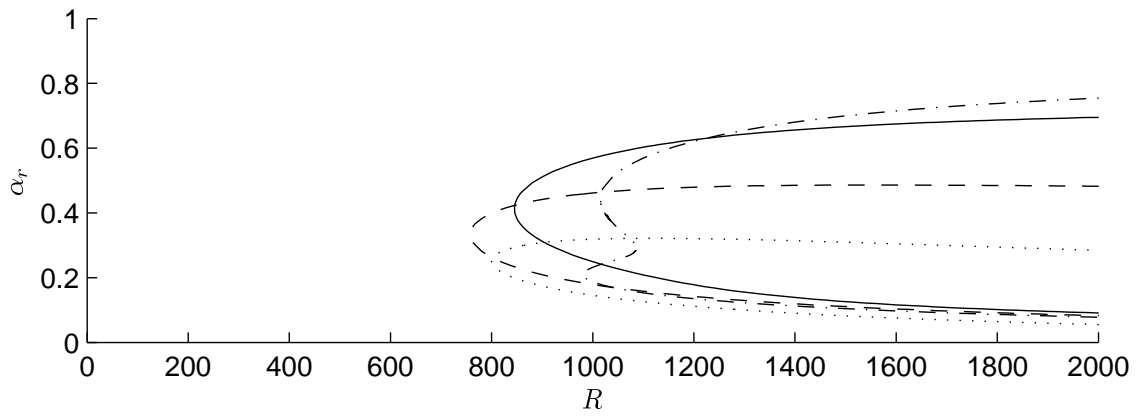


Figure 5.21: Neutral stability curves for  $\alpha_r$  and  $\beta$  at  $\theta = 10^\circ$ ,  $\tau = 0.2$ ,  $\iota = 1$ , and  $c = 0.7$  ( $\cdots$ ),  $0.8$  ( $- -$ ),  $1$  ( $-$ ),  $1.2$  ( $\cdot -$ ).

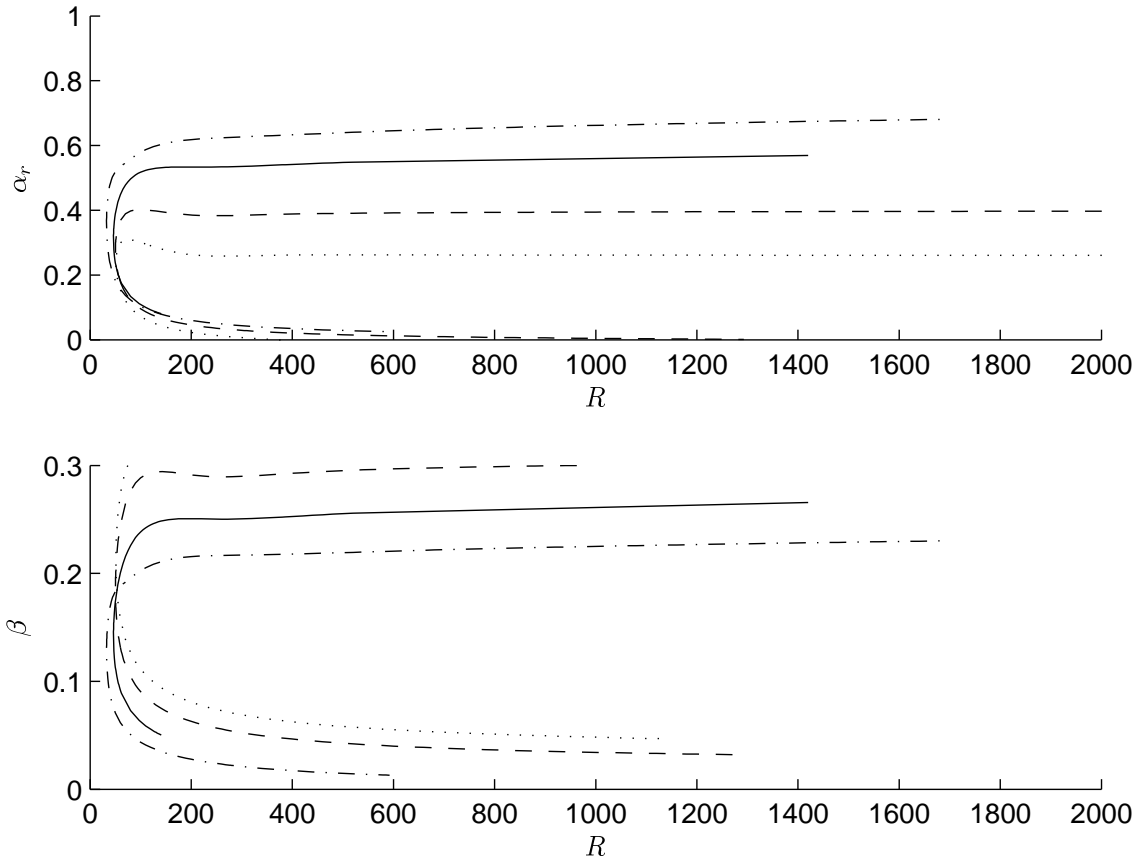


Figure 5.22: Neutral stability curves for  $\alpha_r$  and  $\beta$  at  $\theta = 70^\circ$ ,  $\tau = 0.2$ ,  $\iota = 1$ , and  $c = 0.7$  ( $\cdots$ ), 0.8 ( $- -$ ), 1 ( $-$ ), 1.2 ( $\cdot -$ ).

$\tau$	$\iota$	$c$				$c_{min}$
		0.7	0.8	1.0	1.2	
0.0	-1	<b>9225</b>	<b>6810</b>	6611 ( <b>6309</b> )	6769 ( <b>3997</b> )	0.94
	0	<b>1921</b>	<b>1622</b>	<b>1601</b> (2478)	<b>1650</b> (1681)	0.90
	1	<b>641</b>	<b>596</b>	<b>603</b>	<b>625</b>	0.85
0.2	-1	*	-	-	-	-
	0	*	<b>2951</b>	<b>3005</b> (3056)	4189 ( <b>1482</b> )	0.88
	1	<b>800</b>	<b>758</b>	<b>845</b>	1015 ( <b>982</b> )	0.79

\* No unstable region predicted.

Table 5.7:  $R_c$  for a range of parameter values at  $\theta = 10^\circ$

$\tau$	$\iota$	$c$				$c_{min}$
		0.7	0.8	1.0	1.2	
0.0	-1	<b>3257</b>	<b>2366</b>	2272 ( <b>1993</b> )	2313 ( <b>1249</b> )	0.96
	0	<b>602</b>	<b>508</b>	<b>497</b> (726)	509 ( <b>488</b> )	0.93
	1	<b>190</b>	<b>177</b>	<b>177</b>	<b>181</b>	0.89
0.2	-1	*	-	-	-	-
	0	*	<b>933</b>	937 ( <b>888</b> )	1257 ( <b>416</b> )	0.88
	1	<b>238</b>	<b>226</b>	<b>246</b>	281 ( <b>271</b> )	0.79

\* No unstable region predicted.

Table 5.8:  $R_c$  for a range of parameter values at  $\theta = 30^\circ$

$\tau$	$\iota$	$c$				$c_{min}$
		0.7	0.8	1.0	1.2	
0.0	-1	<b>2317</b>	<b>1615</b>	1523 ( <b>1127</b> )	1536 ( <b>689</b> )	1.02
	0	<b>316</b>	<b>270</b>	<b>261</b> (342)	264 ( <b>226</b> )	0.98
	1	<b>90</b>	<b>84</b>	<b>82</b>	<b>82</b>	1.07
0.2	-1	*	-	-	-	-
	0	*	<b>502</b>	494 ( <b>407</b> )	630 (-)	0.89
	1	<b>112</b>	<b>108</b>	<b>112</b>	<b>109</b>	0.76

\* No unstable region predicted.

Table 5.9:  $R_c$  for a range of parameter values at  $\theta = 50^\circ$

$\tau$	$\iota$	$c$				$c_{min}$
		0.7	0.8	1.0	1.2	
0.0	-1	<b>2506</b>	<b>1506</b>	( <b>421</b> )	( <b>243</b> )	†
	0	<b>157</b>	<b>135</b>	( <b>92</b> )	( <b>49</b> )	†
	1	<b>41</b>	<b>39</b>	<b>36</b>	<b>34</b>	†
0.2	-1	-	-	-	-	-
	0	<b>437</b>	<b>275</b>	<b>93</b>	<b>43</b>	†
	1	<b>51</b>	<b>50</b>	<b>46</b>	<b>33</b>	†

†No minimum within this range of  $c$ .

Table 5.10:  $R_c$  for a range of parameter values at  $\theta = 70^\circ$

are presented here, the results show a smooth transition between the extremes of each parameter. In all cases, larger values of  $c$  make the streamline-curvature lobe increasingly significant with respect to the crossflow lobe.

Tables 5.7–5.10 provide critical Reynolds numbers for a representative range of parameter values, at selected latitudes. Each entry in the table may contain a pair of critical values: one for the crossflow lobe, and one for the streamline-curvature lobe (in brackets). If either lobe is not present, its corresponding value is omitted. In all cases, the lower of the two, representing  $R_c$ , is given in bold text. As with the previous tables, the absence of data is indicated by a dash.

Where the streamline-curvature lobe is present, its critical Reynolds number decreases monotonically with increasing  $c$  over the range examined in this work. For the crossflow lobe, however, there is typically a value of  $c$  for which the critical Reynolds number is minimised; this value is denoted  $c_{min}$  and it is given in the rightmost column.

Also presented here in Tables 5.11–5.14 are the predicted numbers of vortices

Number of vortices:					
$\tau$	$\iota$	$c$			
		0.7	0.8	1.0	1.2
0.0	-1	<b>214</b>	<b>98</b>	62 ( <b>38</b> )	47 ( <b>19</b> )
	0	<b>56</b>	<b>33</b>	<b>22</b> (20)	<b>17</b> (11)
	1	<b>19</b>	<b>14</b>	<b>10</b>	8
0.2	-1	*	-	-	-
	0	*	<b>140</b>	<b>118</b> (57)	132 ( <b>29</b> )
	1	<b>40</b>	<b>34</b>	<b>29</b>	29 ( <b>16</b> )

Angle of vortices:					
$\tau$	$\iota$	$c$			
		0.7	0.8	1.0	1.2
0.0	-1	<b>16.8°</b>	<b>8.9°</b>	5.3° ( <b>9.3°</b> )	3.9° ( <b>6.5°</b> )
	0	<b>29.4°</b>	<b>18.5°</b>	<b>11.4°</b> (19.6°)	<b>8.4°</b> (14.1°)
	1	<b>34.9°</b>	<b>24.8°</b>	<b>16.2°</b>	<b>12.2°</b>
0.2	-1	*	-	-	-
	0	*	<b>35.0°</b>	<b>22.2°</b> (27.0°)	16.9° ( <b>19.6°</b> )
	1	<b>49.4°</b>	<b>37.5°</b>	<b>25.9°</b>	20.0° ( <b>23.9°</b> )

\* No unstable region predicted.

Table 5.11: Vortex number and angle for a range of parameter values at  $\theta = 10^\circ$

and their angles, calculated in the same way as in §5.3. In all cases, increasing  $c$  decreases  $n$  and causes the vortices to assume a shallower angle at the critical point.

Travelling modes with  $c < 1$ , which are expected to be dominant on highly-polished surfaces, appear to be more sensitive to both suction and axial flow than are stationary modes. In most cases, the value of  $c$  that minimises  $R_c$  is less than one, though close to the equator, we can no longer find a minimum in  $R_c$  within the range of  $c$  examined.

## 5.5 Summary of results

In this chapter we have investigated the onset of local convective instability, and presented tables of critical Reynolds numbers for a range of parameter values. Systems with fixed vortex speeds,  $c$ , between 0.7 and 1.2 were considered.

In §5.3, surface suction and injection were seen to have a stabilising and destabilising effect, respectively, upon the flow. There were seen to be two factors involved in understanding the stability of the system: one was the value of  $R_c$ , below which no

Number of vortices:					
$\tau$	$\iota$	$c$			
		0.7	0.8	1.0	1.2
0.0	-1	<b>201</b>	<b>90</b>	57 ( <b>33</b> )	43 ( <b>17</b> )
	0	<b>48</b>	<b>29</b>	<b>19</b> (17)	14 ( <b>9</b> )
	1	<b>16</b>	<b>12</b>	<b>8</b>	<b>6</b>
0.2	-1	*	-	-	-
	0	*	<b>120</b>	98 ( <b>47</b> )	109 ( <b>24</b> )
	1	<b>33</b>	<b>27</b>	<b>23</b>	21 ( <b>13</b> )

Angle of vortices:					
$\tau$	$\iota$	$c$			
		0.7	0.8	1.0	1.2
0.0	-1	<b>15.8°</b>	<b>8.5°</b>	5.1° ( <b>8.6°</b> )	3.7° ( <b>6.0°</b> )
	0	<b>28.8°</b>	<b>18.3°</b>	<b>11.4°</b> (18.8°)	8.4° ( <b>13.7°</b> )
	1	<b>34.4°</b>	<b>24.7°</b>	<b>16.6°</b>	<b>12.3°</b>
0.2	-1	*	-	-	-
	0	*	<b>34.3°</b>	21.9° ( <b>26.4°</b> )	16.6° ( <b>19.0°</b> )
	1	<b>48.3°</b>	<b>37°</b>	<b>25.8°</b>	20.0° ( <b>22.9°</b> )

\* No unstable region predicted.

Table 5.12: Vortex number and angle for a range of parameter values at  $\theta = 30^\circ$

Number of vortices:					
$\tau$	$\iota$	$c$			
		0.7	0.8	1.0	1.2
0.0	-1	<b>176</b>	<b>77</b>	48 ( <b>24</b> )	37 ( <b>13</b> )
	0	<b>33</b>	<b>21</b>	<b>14</b> (12)	11 ( <b>6</b> )
	1	10	8	5	4
0.2	-1	*	-	-	-
	0	*	<b>87</b>	70 ( <b>32</b> )	- (-)
	1	<b>22</b>	<b>18</b>	<b>15</b>	<b>10</b>

Angle of vortices:					
$\tau$	$\iota$	$c$			
		0.7	0.8	1.0	1.2
0.0	-1	<b>13.8°</b>	<b>7.4°</b>	4.4° ( <b>7.0°</b> )	3.2° ( <b>4.9°</b> )
	0	<b>27.5°</b>	<b>17.8°</b>	<b>11.2°</b> (17.4°)	8.3° ( <b>12.7°</b> )
	1	<b>33.0°</b>	<b>24.2°</b>	<b>16.2°</b>	<b>12.5°</b>
0.2	-1	*	-	-	-
	0	*	<b>33.2°</b>	21.3° ( <b>25.0°</b> )	16.2° (-)
	1	<b>46.4°</b>	<b>35.9°</b>	<b>25.3°</b>	<b>20.9°</b>

\* No unstable region predicted.

Table 5.13: Vortex number and angle for a range of parameter values at  $\theta = 50^\circ$

Number of vortices:					
$\tau$	$\iota$	$c$			
		0.7	0.8	1.0	1.2
0.0	-1	<b>148</b>	<b>56</b>	<b>(10)</b>	<b>(5)</b>
	0	<b>16</b>	<b>10</b>	<b>(4)</b>	<b>(2)</b>
	1	<b>5</b>	<b>4</b>	<b>3</b>	<b>2</b>
0.2	-1	-	-	-	-
	0	<b>83</b>	<b>45</b>	<b>12</b>	<b>6</b>
	1	<b>10</b>	<b>9</b>	<b>6</b>	<b>4</b>

Angle of vortices:					
$\tau$	$\iota$	$c$			
		0.7	0.8	1.0	1.2
0.0	-1	<b>9.9°</b>	<b>5.3°</b>	<b>(3.9°)</b>	<b>(2.7°)</b>
	0	<b>24.1°</b>	<b>17.3°</b>	<b>(13.7°)</b>	<b>(9.5°)</b>
	1	<b>29.4°</b>	<b>22.5°</b>	<b>15.7°</b>	<b>12.3°</b>
0.2	-1	-	-	-	-
	0	<b>50.0°</b>	<b>31.2°</b>	<b>21.7°</b>	<b>16.1°</b>
	1	<b>41.8°</b>	<b>33.2°</b>	<b>24.4°</b>	<b>19.5°</b>

Table 5.14: Vortex number and angle for a range of parameter values at  $\theta = 70^\circ$

convective instability is predicted to arise; the other was the range of wavenumbers,  $\alpha$  and  $\beta$ , that is susceptible to instability.

Increased axial flow was seen to exaggerate the streamline curvature lobe relative to the crossflow lobe, and in most cases, it significantly increased  $R_c$ . However, it typically broadened the range of  $\alpha$  and  $\beta$  that supported the convectively unstable flow regime, with the greatest effect seen in the position of the upper branch.

In §5.4, similar effects were observed over the range of  $c$  that was studied. Models with low vortex speeds were typically seen to be more sensitive to changes in  $\tau$  and  $\iota$ . Lowering  $c$  caused the unstable region to shrink or, in some cases, disappear altogether.

# Chapter 6

## Convective growth rates

### 6.1 Growth rates

Before examining local absolute instability in the model, we now look at the spatial growth rates of the azimuthal disturbance. In the previous chapter, we used  $\alpha = \alpha_r + i\alpha_i$  to represent the complex wavenumber of the latitudinal disturbance, and our formulation (in particular, the form of Equation (5.1)) means that  $-\alpha_i$  can be interpreted as the amplification rate of the disturbance. This quantity may dictate which combination of wavenumber and phase velocity is likely to be selected, and this will have implications for the long-time behaviour of the flow.

The procedure for finding the maximum growth rate associated with a given point in the parameter space is similar to that used to obtain neutral-stability curves in Chapter 5. Because the range of Reynolds numbers covered by the convectively unstable region varies with  $\theta, \iota, \tau$  and  $c$ , maximum growth rates are sampled at a fixed distance into this region. In this way, a consistent comparison can be made between different models. Garrett & Peake (2002) have shown that the rotating-sphere boundary layer becomes absolutely unstable at a particular Reynolds number,  $R_a$ . Beyond this point, the flow is turbulent and the spatial growth rate is undefined. For this reason, it is important to sample the convective growth rate at some  $R$  within the range  $R_c < R < R_a$ . Having chosen values for  $\theta, \iota, \tau$  and  $c$ , we select the Reynolds number to be  $R = R_c + 150$ . This is far enough into the unstable region

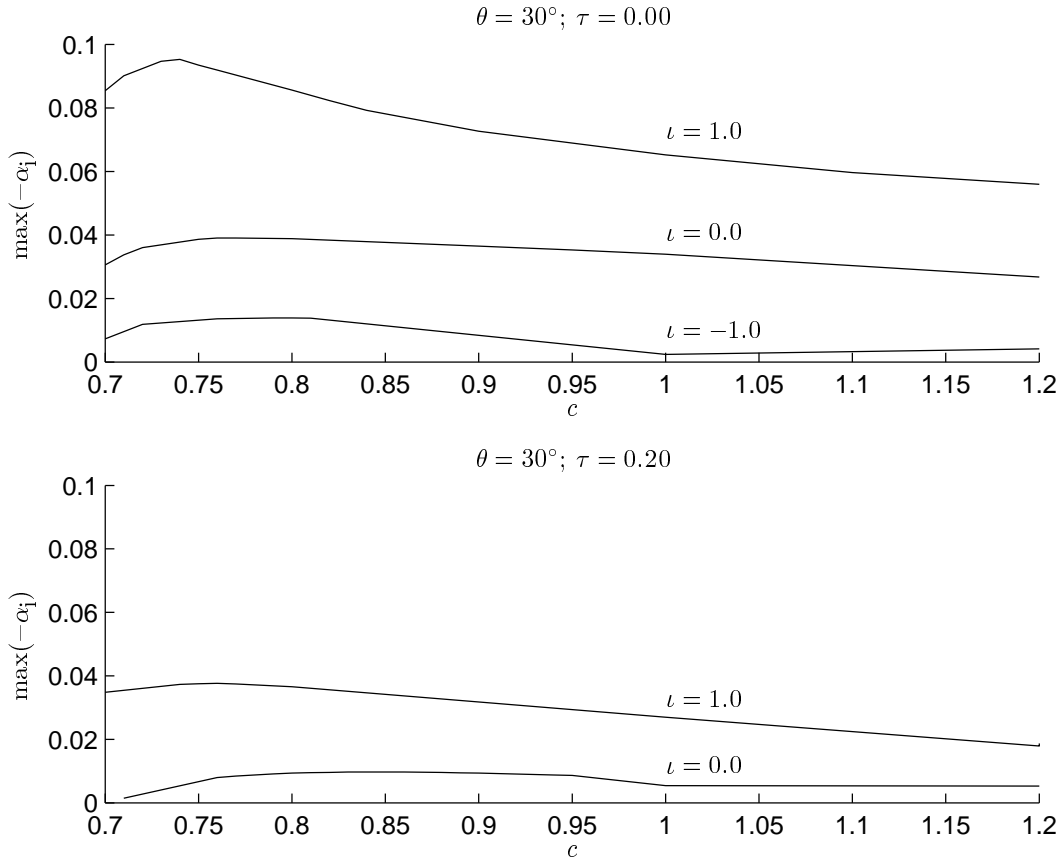


Figure 6.1: Spatial growth rates over a range of  $c$  at selected  $\tau$  and  $\nu$ ;  $R = R_c + 150$ ,  $\theta = 30^\circ$ .

to conduct the study. Beginning at some arbitrary value of  $\beta$ , we use the dispersion relation (5.35) to solve for  $\alpha$ , then proceed to march through  $\beta$ , solving for  $\alpha$  at each step. Rather than recording only the neutral points, where  $\alpha_i = 0$ , we record the entire spatial branch. At some point along the branch, within the unstable region,  $\alpha_i$  will attain a minimum (and the growth rate,  $-\alpha_i$ , will attain a maximum) and this gives the growth rate we use for comparison.

## 6.2 Results

Figure 6.1 shows how spatial growth-rates vary with suction, axial flow and vortex speed, at  $\theta = 30^\circ$ .

Table 6.1 presents this information in tabular form, giving the values of  $c$  for which  $-\alpha_i$  is maximised, computed for certain models at  $\theta = 30^\circ$ . At this latitude, the maximum growth rate is always associated with vortices travelling more slowly

		$\tau$	
		0.00	0.20
$\iota$	-1.0	0.80	-
	0.0	0.76	0.84
	1.0	0.74	0.76

Table 6.1: Vortex speed,  $c$ , giving maximum spatial growth rate at  $\theta = 30^\circ$

than the sphere surface. With  $\iota = \tau = 0$ , the maximum growth rate is predicted at a disturbance speed of  $c = 0.76$ , which shows excellent agreement with theoretical results of Garrett (2010c), and may provide some insight into the slow-vortex observations of Kobayashi & Arai (1990). It is interesting to note that the same value of  $c$  is found in all related rotating geometries, (Garrett (2010a,b, 2011), Samad & Garrett (2013)). In the absence of mass flux, the data also corroborate Garrett's observation that the peak moves to a slightly higher value of  $c$  with increased axial flow. In general, increased axial flow decreases the maximum growth rate. Although not shown here, results obtained for latitudes other than  $30^\circ$  indicate that the growth rates increase with  $\theta$ .

Suction is seen to significantly lower the growth rate in all cases. This is sensible, given that suction has already been shown to have a stabilising effect. If we insist on stationary vortices, we find that with  $\tau = 0$  and  $\theta = 30^\circ$ , one unit of suction causes a 93% decrease in the maximum growth rate and one unit of injection increases it by 92%. With  $c$  fixed at 0.76, these figures become 65% and 135%, respectively. It is clear that the effects of suction are highly dependent on the selected vortex speed. Suction also raises the vortex speed that possesses the maximum growth rate.

The plots in Figure 6.2 show the spatial branches for a broad sample of the parameter space at a fixed latitude of  $30^\circ$ . The points at which the branches intersect with the  $(R, \alpha_r)$ -plane form the neutral curve in each case, and the branches' height above the  $(R, \alpha_r)$ -plane gives the spatial growth rate at that point. These plots emphasise the previous observation that slowly-travelling vortices (to the left of the figure) are associated with larger growth rates.

Beyond a certain Reynolds number, some cases exhibit a change in the form

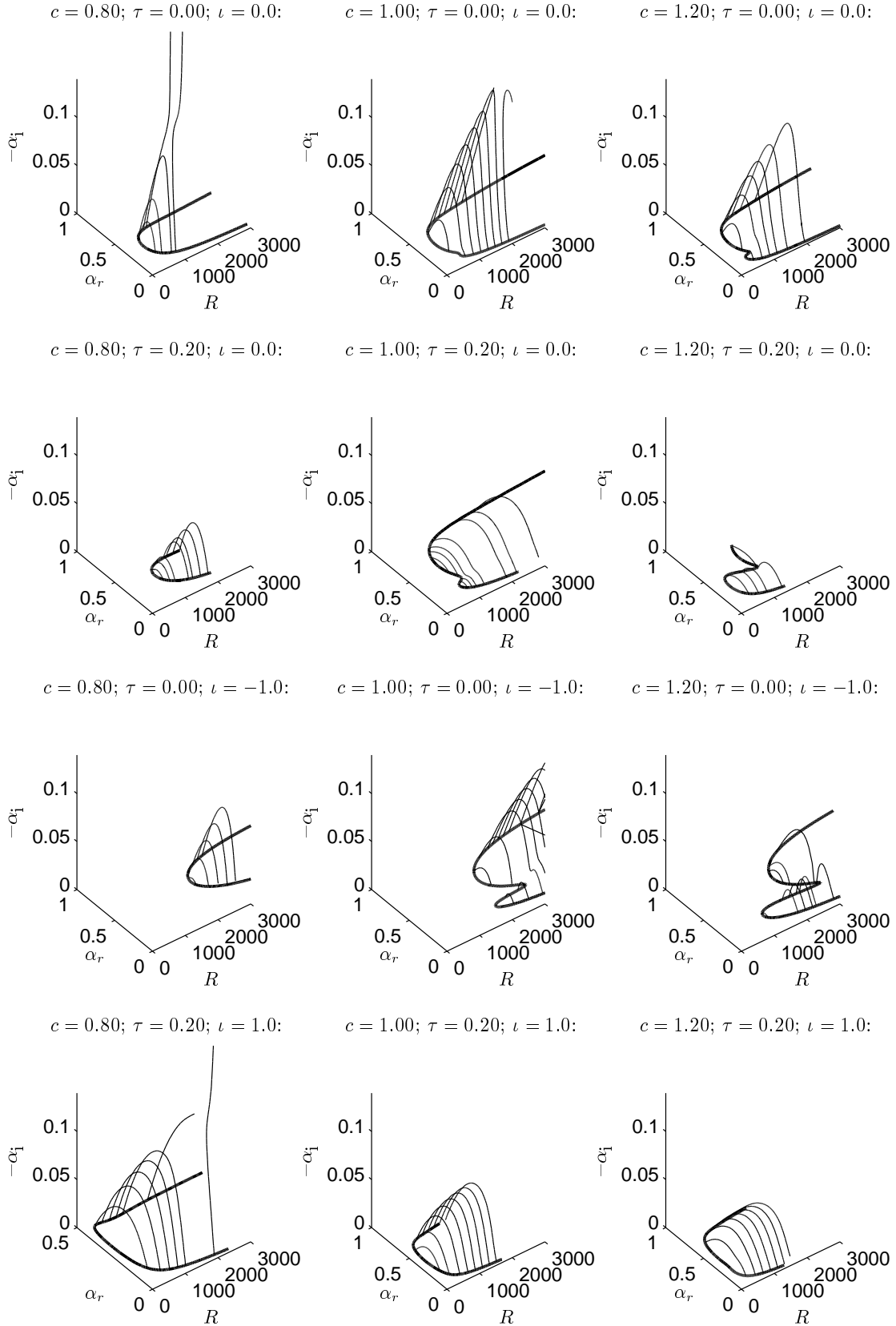


Figure 6.2: Spatial branches showing growth rates for various  $R$  at  $\theta = 30^\circ$ . The bold lines in the  $(R, \alpha_r)$ -plane are the neutral curves calculated previously.

of the spatial branches, and the maximum growth rate becomes undefined. This corresponds to the onset of absolute instability, which is the subject of the next chapter.

# Chapter 7

## Absolute stability analysis

### 7.1 Absolute instability

We now turn our attention to the occurrence of local absolute instability, where the initial disturbance causes a reaction that is unbounded for large time at all points in space. Prediction of the onset of absolute instability therefore requires that we use a spatio-temporal analysis, in contrast to the purely spatial analysis that was sufficient when modelling convective instability. While the imaginary part of  $\gamma$  was zero by assumption during the convective analysis, it can no longer be restricted to taking on real values; both  $\alpha$  and  $\gamma$  are considered to be complex quantities, while  $\beta$  remains real to ensure periodicity in the rotating system.

The notion of disturbance phase velocity, denoted  $c$  in Chapters 5 and 6, is not relevant to the analysis of absolute instability. Consequently,  $c$  does not appear in the dispersion relation:

$$D(\alpha, \beta, \gamma; R, \theta, \tau, \iota) = 0.$$

Occurrences of absolute instability can be found using the time-asymptotic Briggs-Bers procedure (see Briggs (1964), Bers (1972)). At  $t = 0$ , the system is perturbed at a particular latitude  $\theta_s$ , by an impulsive line forcing parallel to the equator, given by  $\delta(\theta - \theta_s)\delta(t)e^{in\phi}$ , where  $\delta$  is the Dirac delta function. Singularities in the dispersion

relation are sought, where

$$D(\alpha, \beta, \gamma; R, \theta, \tau, \iota) = 0,$$

which correspond to points where spatial branches “pinch” together. In order for the point of this coalescence to be considered a “pinch point”, it is necessary for the two branches forming the singularity to originate on opposite sides of the complex- $\alpha$  plane, in the limit of large positive  $\gamma_i$ . The frequency at such a pinch point is then denoted  $\gamma_0$ , with real and imaginary parts,  $\gamma_{0,r}$  and  $\gamma_{0,i}$ , respectively. The corresponding wavenumber is  $\alpha_0 = \alpha_{0,r} + i\alpha_{0,i}$ . At a pinch point, the latitudinal group velocity,  $\partial\gamma/\partial\alpha(\alpha_0) = 0$ . It is necessary for  $\gamma_{0,i}$  to be positive in order to identify absolute instability (see §1.2.1 for a more detailed explanation of the relevant stability theory). If  $\gamma_{0,i}$  is negative, the pinch point does not imply the existence of absolute instability; if instability exists at such a point, it is convective in nature.

## 7.2 Results

Unlike the convective neutral stability curves of previous chapters, neutral curves for absolute instability are always single-lobed. The critical Reynolds number for the onset of absolute instability for a given case is denoted by  $R_a(\theta; \iota, \tau)$ , and it always holds that  $R_a \geq R_c$ . No attempt has been made to present all the relevant neutral curves, but for the purposes of illustration, Figure 7.1 gives some typical examples of the form they take. Although only these plots are presented here, it is found that for fixed  $\theta$ ,  $\iota$  and  $\tau$ , the range of wavenumbers  $\alpha$  and  $\beta$  that is susceptible to absolute instability is typically far narrower than that which is susceptible to convective instability, even when compared against the results for low convective vortex speeds which usually produce narrower neutral curves.

Table 7.1 gives the critical Reynolds numbers for the onset of absolute instability at a range of latitudes, for various magnitudes of axial flow, all with  $\iota = 0$ . Axial

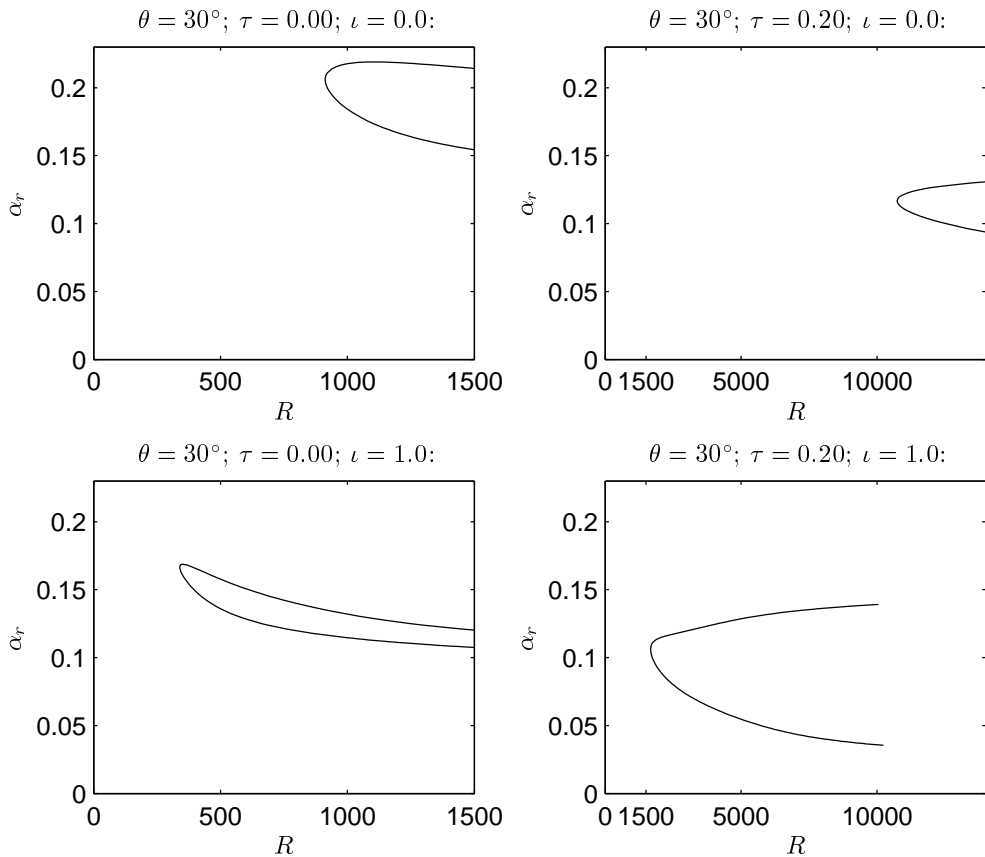


Figure 7.1: Examples of neutral absolute instability curves at  $\theta = 30^\circ$ .

flow is seen to significantly increase  $R_a$ , especially at low latitudes. Comparing these figures to those calculated by Garrett & Peake (2002), Garrett (2002), we find they are in excellent agreement at low-to-moderate latitudes. However, the data (which are not presented here) show an increasing discrepancy as  $\theta$  is increased. The author believes that this is due to a slight difference in the steady basic flow profiles used, and the results presented here are considered to be more reliable, as they are based on a refined version of the NAG implementation.

With the introduction of non-zero mass flux, we examine in detail the latitudinal position of  $\theta = 30^\circ$ . Table 7.2 gives the value of  $R_a$  for several combinations of parameters (combinations for which no data could be obtained are marked with '-'), and Figure 7.2 uses the same data to show how  $R_a$  is affected by changes in  $\tau$  and  $\nu$ . It shows that as  $\nu$  increases from  $-1.0$  (the topmost line) to  $1.0$  (the bottom-most line),  $R_a$  grows less quickly with  $\tau$ . This suggests that surface suction postpones the onset of absolute instability and that injection promotes it, with a substantially greater effect observed for large magnitudes of forced axial flow. These plots are

		$\tau$					
		0.00	0.05	0.10	0.15	0.20	0.25
$\theta$	10°	2883	4198	7420	15317	36703	103663
	30°	913	1321	2299	4626	10738	29165
	50°	482	690	1177	2299	5139	13368
	70°	240	346	578	1095	2370	5989

Table 7.1:  $R_a$  at selected latitudes for  $\iota = 0.0$

		$\tau$					
		0.00	0.05	0.10	0.15	0.20	0.25
$\iota$	-1.0	3784	8531	20509	-	-	-
	-0.5	1735	3017	6184	14552	-	-
	0.0	913	1321	2299	4626	10738	29165
	0.5	535	697	1072	1881	3735	8418
	1.0	339	417	594	947	1673	3276

Table 7.2:  $R_a$  at selected parameter values for  $\theta = 30^\circ$

similar in shape to those in Figure 5.12, demonstrating that altering the suction and axial-flow parameters has qualitatively the same effect on absolute instability as it has on convective instability.

### 7.2.1 Comparison to experiment

There has been limited experimental work on the rotating sphere in still fluid; here we attempt to relate our results to the observed onset of turbulence in those experiments; this is distinct from the onset of the convective instability that is associated with and compared to the onset of the spiral vortices. Figure 7.3 places the Reynolds numbers we have calculated as marking the onset of local absolute instability (the dashed line) alongside the Reynolds numbers for the observed onset of turbulence from three experiments. The earliest of these experiments was performed by Sawatzki (1970) using a sphere of diameter 240mm, and the remaining two were performed by Kohama & Kobayashi (1983), using spheres of diameter 150mm and 250mm. Note that these experimental results have simply been read off the graphs in the latter paper and they are therefore approximate. The experimental data is presented in terms of the “spin” Reynolds number,  $R_S$ , which is equal to  $R^2$  in our notation. It can be seen that turbulence is observed to arise at a higher Reynolds

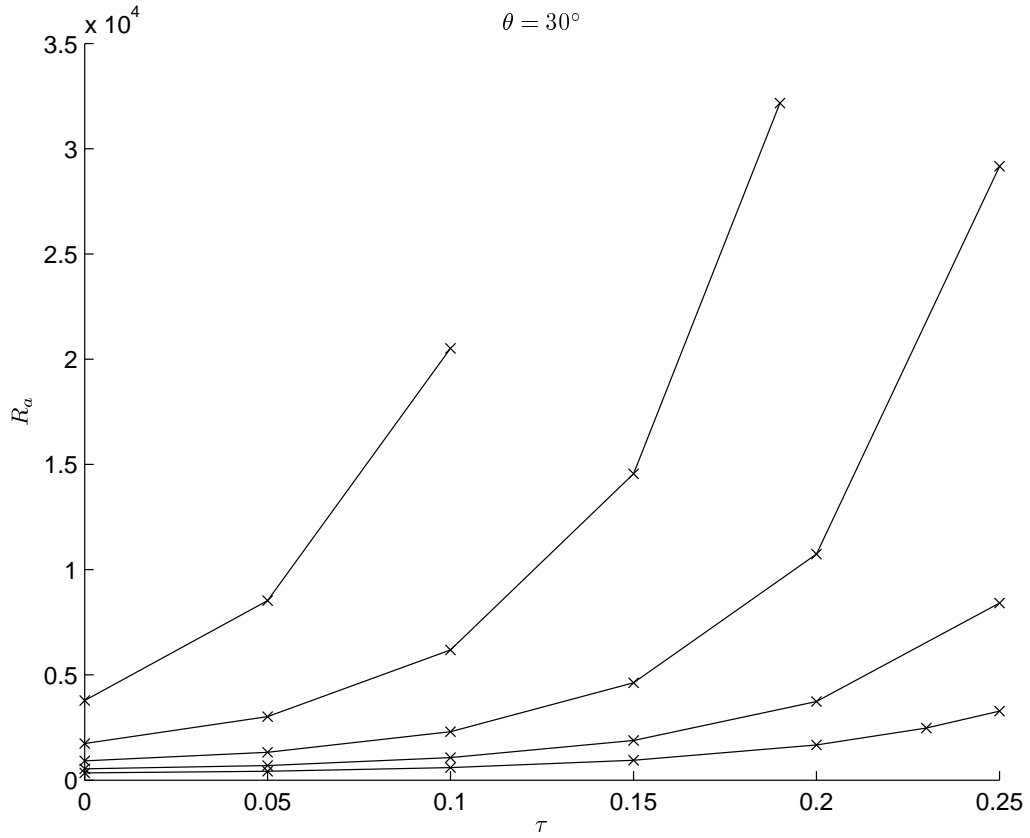


Figure 7.2: Critical Reynolds numbers,  $R_a$ , for the onset of absolute instability at  $\theta = 30^\circ$ ; for  $\nu = -1, -0.5, 0, 0.5, 1$  (leftmost-top to bottom).

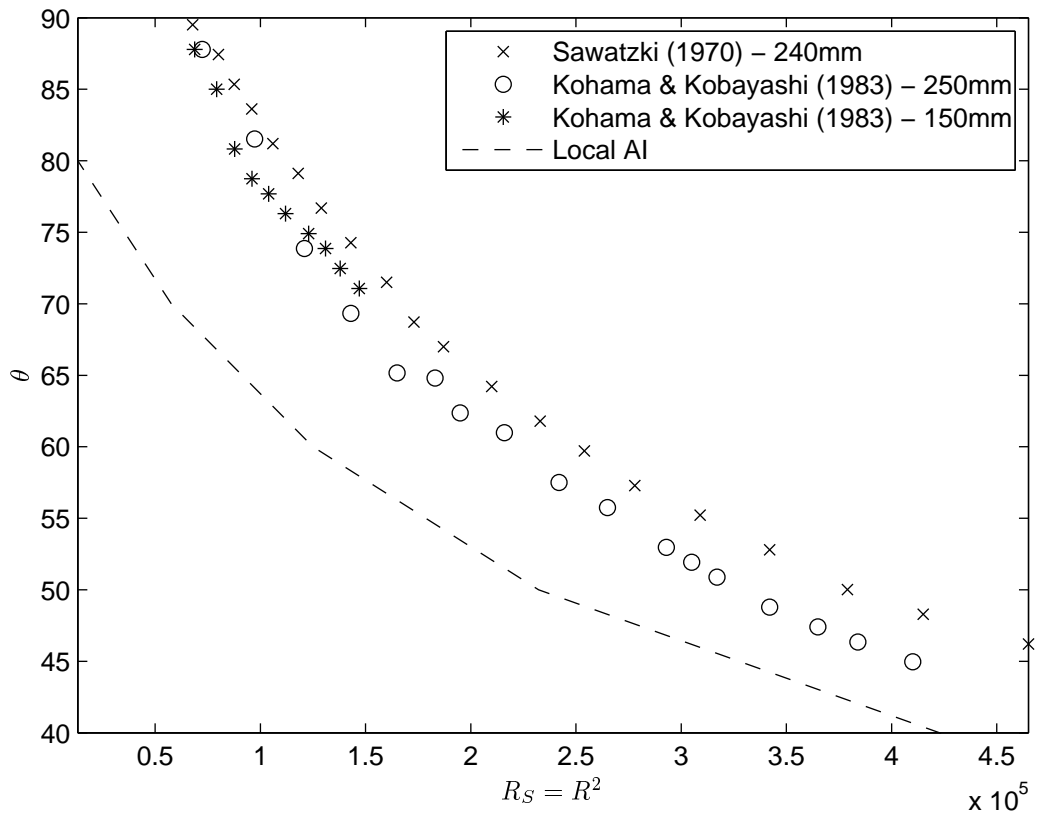


Figure 7.3: Reynolds numbers at the onset of turbulence

		$\tau$		
		0.00	0.10	0.20
$\iota$	-1.0	0.104	0.010	-
	-0.5	0.265	0.052	-
	0.0	0.594	0.195	0.024
	0.5	1.116	0.516	0.101
	1.0	1.855	1.047	0.289
		$\times 10^{-3}$		

Table 7.3: Maximum temporal growth rates,  $\gamma_i$ , for absolute instability at  $\theta = 30^\circ$

number than our predicted value of  $R_a$  at all latitudes above  $40^\circ$ . The difference appears to decrease with decreased latitude, however. More recent experimental observations on disks (for example, Lingwood (1996)) report transitional Reynolds numbers much closer to the theoretical onset of absolute instability; it is therefore possible that further experiment on the sphere at lower latitudes (where the sphere increasingly approximates a flat disk) could give closer agreement with our results at a later date. Unfortunately there is no experimental data available for latitudes  $\theta < 40^\circ$ . The discrepancy at high latitudes may indicate that the onset of turbulence is governed by a different mechanism at these positions. We will consider these experimental results again in Chapter 8, during the global stability analysis.

### 7.2.2 Absolute growth rates

During the convective stability analysis, we considered the spatial growth rate of the disturbance. Here we can identify  $\gamma_i$  as the temporal growth rate, which we sample in a manner similar to the way  $-\alpha_i$  was sampled in Chapter 6, i.e. by taking its maximum value at a fixed distance beyond the critical Reynolds number. Table 7.3 gives the maximum value of  $\gamma_i$  at the position  $R_a(\theta; \iota, \tau) + 150$ , for a range of parameter values at  $\theta = 30^\circ$ . Where  $R_a$  could not be determined in §7.1, table entries are marked with ‘-’. Growth rates are seen to be affected in the same way as the value of  $R_a$  by changes in the parameters  $\iota$  and  $\tau$ : they are reduced by surface mass-suction and axial flow, and increased by surface mass-injection. Although data for other latitudes are not shown here, growth rates also increase with  $\theta$ .

The results of the local stability analysis obtained in this chapter form the basis of the global stability analysis of Chapters 8 and 9.

# Chapter 8

## Global stability analysis

### 8.1 Introduction

The stability analysis up to this point has been based on the assumption that the boundary layer is spatially homogeneous. This has limited us to examining the local stability characteristics at individual latitudinal positions on the rotating sphere. We now wish to infer the global behaviour of the flow from the collection of local analyses over the body surface.

### 8.2 Formulation

In this chapter we continue with the viscous formulation used previously. This enables control over the spin rate as determined by  $R$ . We initially analyse the global instability with a low Reynolds number of  $R = 100$ , then examine the effects of increasing this in several steps to  $R = 2000$ . As  $R$  is increased, we expect our results to tend to those for the inviscid case.

As described in §1.2.2, the global analysis requires us to use a slowly-varying streamwise parameter. For this reason we reformulate the problem to satisfy this condition. We consider a spherical body of revolution with surface described by the equation  $r_0^* = r_0^*(s^*)$ , where  $s^*$  is the arc length measured along the surface of the body starting from the pole and  $r_0^*(s^*)$  is the cross-sectional radius of the body in

the plane perpendicular to the axis of symmetry. The body spins about its axis with angular velocity  $\Omega^*$ , in an otherwise undisturbed incompressible fluid. We consider typical length and time scales to be  $(\nu^*/\Omega^*)^{1/2}$  and  $(\nu^*/\Omega^{*3})^{1/2}/a^*$  respectively. We non-dimensionalise  $s^*$  and  $r_0^*(s^*)$  with the typical length scale to form

$$s = \frac{s^*}{(\nu^*/\Omega^*)^{1/2}}, \quad r_0(s) = \frac{r_0^*(s^*)}{(\nu^*/\Omega^*)^{1/2}},$$

and define further nondimensional spatial variables

$$\mathcal{S} = \frac{s^*}{a^*}, \quad R_0(\mathcal{S}) = \frac{r_0^*}{a^*}.$$

By eliminating  $s^*$  and  $r_0^*(s^*)$  between the two sets of scaled spatial variables we find that  $\mathcal{S}$  is the slow spatial variable and  $R_0$  is the slowly varying surface radius, i.e.

$$\mathcal{S} = \varepsilon s^*, \quad R_0(\mathcal{S}) = \varepsilon r_0^*$$

with

$$\varepsilon = \frac{1}{a^*} \sqrt{\frac{\nu^*}{\Omega^*}}, \quad (8.1)$$

which is the ratio of the characteristic boundary-layer thickness to the characteristic size of the body. In what follows we assume that  $\varepsilon \ll 1$ , which will be seen to be consistent with the assumption of large Reynolds number by Equation (8.4). From our previous calculations in Chapter 7 (Tables 7.1 and 7.2), it would then follow that  $\varepsilon = 1/2883 \rightarrow 1/240$ , which provides an *a posteriori* justification of the small  $\varepsilon$  analysis at each location over the sphere. It is clear that  $R_0(\mathcal{S}) = \sin \mathcal{S}$  and we see that the slow spatial variable  $\mathcal{S}$  can be identified with the latitudinal angle,  $\theta$ .

We now introduce the transverse coordinate  $\eta^* \equiv (\nu^*/\Omega^*)^{1/2}\eta$ , which points in the normal direction out of the sphere, with  $\eta = 0$  being the sphere surface, together with the azimuthal angle  $\phi$  measured around the axis. The coordinates  $\mathcal{S}$ ,  $\phi$  and  $\eta$  form the coordinate system for our problem, and the fluid velocity has components  $U^*$ ,  $V^*$ ,  $W^*$  in these respective directions. We write these velocity components in

the form of an axisymmetric non-swirling steady flow plus an unsteady perturbation,

$$\begin{aligned} U^* &= a^* \Omega^* [U(\mathcal{S}, \eta) + \varepsilon \bar{u}(\mathcal{S}, \phi, \eta, t)] \\ V^* &= a^* \Omega^* [V(\mathcal{S}, \eta) + \varepsilon \bar{v}(\mathcal{S}, \phi, \eta, t)] \\ W^* &= a^* \Omega^* \varepsilon [W(\mathcal{S}, \eta) + \bar{w}(\mathcal{S}, \phi, \eta, t)], \end{aligned} \quad (8.2)$$

where  $t$  is time nondimensionalised as indicated above, and the overbar denotes the unsteady perturbation. Note that the characteristic scale of the steady velocities in the  $\mathcal{S}$  and  $\phi$  directions is  $a^* \Omega^*$ , while the steady  $\eta$  (wall-normal) velocity has scale  $(\nu^* \Omega^*)^{1/2}$ , which we have also taken as the scale of the unsteady perturbations. Finally, we note that the corresponding dimensional pressure can be written in the form

$$\rho^* (a^* \Omega^*)^2 \varepsilon [\varepsilon P(\theta, \eta) + \bar{p}(\theta, \phi, \eta, t)], \quad (8.3)$$

where  $\rho^*$  is the fluid density. These scalings define the Reynolds number of the system as

$$R = \frac{a^* \Omega^* \sqrt{\nu^* / \Omega^*}}{\nu^*} = a^* \sqrt{\frac{\Omega^*}{\nu^*}} = \frac{1}{\varepsilon}. \quad (8.4)$$

The Reynolds number is therefore seen to be a direct measure of the scaled boundary-layer thickness and an indirect measure of the rotation rate,  $\Omega^*$ .

The equations for the steady boundary-layer flow around the sphere to leading order in  $\varepsilon$  are given in Chapter 2 as Equations (2.5)–(2.7). After the substitution of  $\mathcal{S}$  for  $\theta$ , these partial differential equations in  $\mathcal{S}$  and  $\eta$  are solved subject to the no-slip and quiescent fluid boundary conditions (4.6).

We now consider the unsteady flow where the resulting perturbation equations are as stated in (5.6)–(5.9) (after appropriate variable substitutions). In what follows we will be interested in the long-time response of the perturbation equations to initial forcing. Briggs (1964) and Bers (1972) have shown that such behaviour can be analysed by investigating the dispersion properties of single-frequency homogeneous solutions. The Briggs-Bers procedure was developed for spatially homo-

geneous systems, but a significant extension was made by Monkewitz *et al.* (1993), who considered weakly-nonparallel flows which evolve only slowly in the streamwise direction. We therefore look for solutions of the perturbation equations of the form

$$(\bar{u}, \bar{v}, \bar{w}, \bar{p})(\mathcal{S}, \eta, \phi, t) = (\tilde{u}, \tilde{v}, \tilde{w}, \tilde{p})(\mathcal{S}, \eta) \exp\left(in\phi - i\gamma t + i \int^{\mathcal{S}} \alpha(\mathcal{S}') d\mathcal{S}'\right). \quad (8.5)$$

Here  $n$  must be an integer in order to enforce periodicity in the  $\phi$  direction around the axis of symmetry. We will require  $n$  to be large, and choose the preferred scaling  $n = \bar{n}/\varepsilon$ , with  $\bar{n} = O(1)$ . It is crucial to note that we are looking for a global mode with azimuthal order which is the same at all  $\mathcal{S}$ . We now proceed by substituting (8.5) into the perturbation equations and, after completing a series of straightforward manipulations, we find the system identical to (5.16)–(5.21) after the simple substitution of  $\beta = \bar{n}/\sin\theta$  and  $\theta = \mathcal{S}$ .

As the steady flow is a mixed function of  $\mathcal{S}$  and  $\eta$ , it is impossible to scale out  $\bar{n}$  in the perturbation system and we must consider each value of  $\bar{n}$  separately. The numerical solution of the perturbation system is completed in a standard fashion, using a fourth-order Runge-Kutta integrator, starting from an analytical solution at the outer edge of the boundary layer (taken to be at  $\eta = 20$ ), and using a Newton-Raphson search procedure to solve the associated eigenvalue problem. The implementation of this solution method is an amended version of a Fortran routine used by Garrett (2002), based on code originally developed by Lingwood (1995a). Full details can be found in Chapter 5.

### 8.3 Global modes

Monkewitz *et al.* (1993) show that the long-time behaviour of a weakly-nonparallel flow is governed by the behaviour of the global mode of complex frequency  $\gamma_G$ : if  $\text{Im}(\gamma_G) > 0$  then the global mode is unstable, and hence the flow will be globally unstable, whereas if  $\text{Im}(\gamma_G) < 0$  then the global mode is damped and the flow will be globally stable. The global-mode frequency is determined as follows. First, for

each real  $\mathcal{S}$  we look for a pinch in the complex- $\alpha$  plane, i.e. for points of zero group velocity,  $\partial\gamma/\partial\alpha = 0$ , formed by the coalescence of modes from opposite halves of the complex- $\alpha$  plane. This provides us with a complex local absolute frequency,  $\gamma = \gamma^\circ(\mathcal{S})$ , along the real- $\mathcal{S}$  axis. Second, we search for a  $\mathcal{S}$  pinch point in  $\gamma^\circ(\mathcal{S})$ , which in general will occur at complex  $\mathcal{S}$  and will therefore necessitate analytical continuation off the real- $\mathcal{S}$  axis. In other words, we find a saddle point  $\partial\gamma^\circ/\partial\mathcal{S} = 0$ , and then verify that the  $\mathcal{S}$  contour can be deformed off the real axis so as to lie along the steepest descent contour through this saddle. Once these conditions have been satisfied, the global mode frequency simply corresponds to the frequency,  $\gamma_G$ , of this double  $\alpha$ - $\mathcal{S}$  pinch at the saddle location,  $\mathcal{S}_G$ .

We solve the perturbation system for local absolute instability over the sphere by marching through the range of  $\mathcal{S}$  in one degree increments for pairs of values of azimuthal wavenumber  $\bar{n}$  and Reynolds number  $R$ . In practice, it is known that an eruption of the boundary layer occurs at the equator ( $\mathcal{S} = 90^\circ$ ) and pollutes the steady flow around that region (see Sawatzki (1970), Kohama & Kobayashi (1983)), for this reason the study is confined to  $\mathcal{S} \leq 80^\circ$ . Typical results are demonstrated in Figure 8.1 where we show the absolute frequency  $\gamma^\circ(\mathcal{S})$  for a sample of  $\bar{n}$ ,  $R$  parameter pairs. Pockets of local absolute instability can be seen provided that  $\bar{n}$  is sufficiently small and  $R$  sufficiently large. Although not shown in Figure 8.1, our study considers all combinations of parameter pairs from  $\bar{n} = 0.05$  to 0.25 (in increments of 0.05) and  $R = 100, 200, 300, 400, 500, 1000, 2000$ .

Unlike for the rotating disk/cone (see Garrett & Peake (2007)), an analytical continuation of the absolute frequencies to complex  $\mathcal{S}$  cannot be undertaken easily, due to the complicated dependence of the base flow on  $\mathcal{S}$  in the governing partial differential equations. Instead we follow the suggestion of Cooper & Crighton (2000) and use Páde approximants. The idea is that a rational function is fitted to complex  $\gamma^\circ(\mathcal{S})$  for real  $\mathcal{S}$  (see Press *et al.* (1992)), which can then be interrogated to determine the location of any pinch point in complex  $\mathcal{S}$ . After extensive tests with different orders of Páde approximant, it was found that using polynomials of order five for

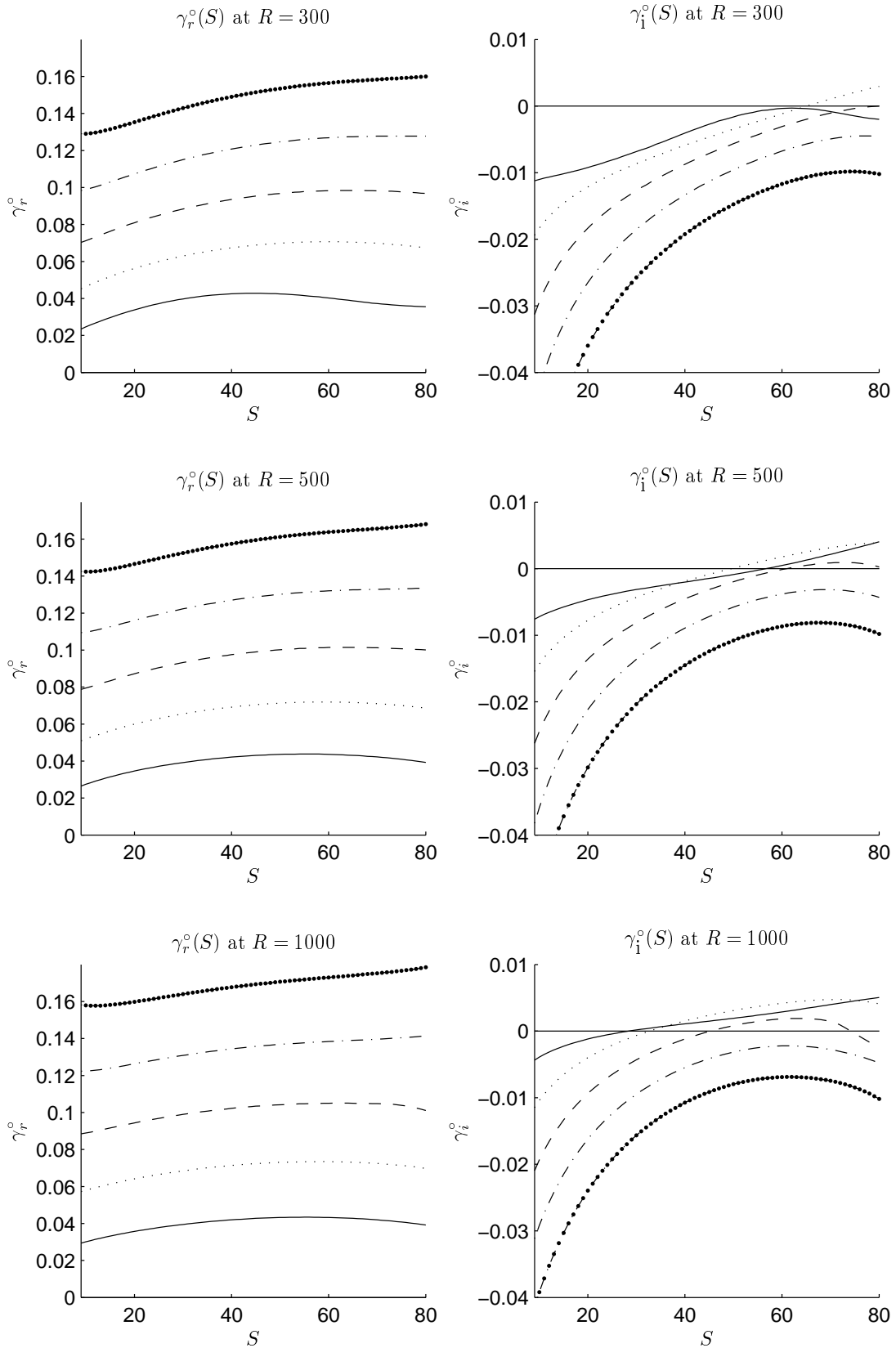


Figure 8.1: Plots of absolute frequency,  $\gamma^\circ(\mathcal{S})$  at various  $R$ ;  $\bar{n} = 0.05, 0.10, 0.15, 0.20, 0.25$ : ‘—’, ‘- -’, ‘...’, ‘- · -’, ‘- · - · -’, respectively.

both the numerator and the denominator typically gave the smallest error for each parameter set. In Cooper & Crighton's notation,  $E_m$ , the root mean square error incurred by using the Páde function to approximate the data on the real axis, is at worst  $O(10^{-4})$ . This method of approximation yields a complex absolute frequency which agrees with the original results to three decimal places for each  $\bar{n}$  and  $R$  at all integer values of  $\mathcal{S}$  in the range  $10^\circ \leq \mathcal{S} \leq 80^\circ$ .

Figures 8.2–8.4 show sample contours of  $\gamma_i^\circ$  in the complex- $\mathcal{S}$  plane for a small sample of  $\bar{n}, R$  parameter pairs. Saddle points are visible towards the right of each plot and are marked with a '\*'. The thicker lines represent the zero contour ( $\gamma_i^\circ = 0$ ). Table 8.1 gives the positions of the saddle points,  $\mathcal{S}_S$ , and the associated global frequencies,  $\gamma_G$ , for a range of parameters. Positive growth rates ( $\text{Im}(\gamma_G)$ ) indicating globally unstable flow are highlighted with bold text. Furthermore, we are able to plot the neutral curve for linear global instability by repeating the analysis at various  $\bar{n}$  and recording  $R$  such that  $\text{Im}(\gamma_G) = 0$ ; this is shown in Figure 8.5.

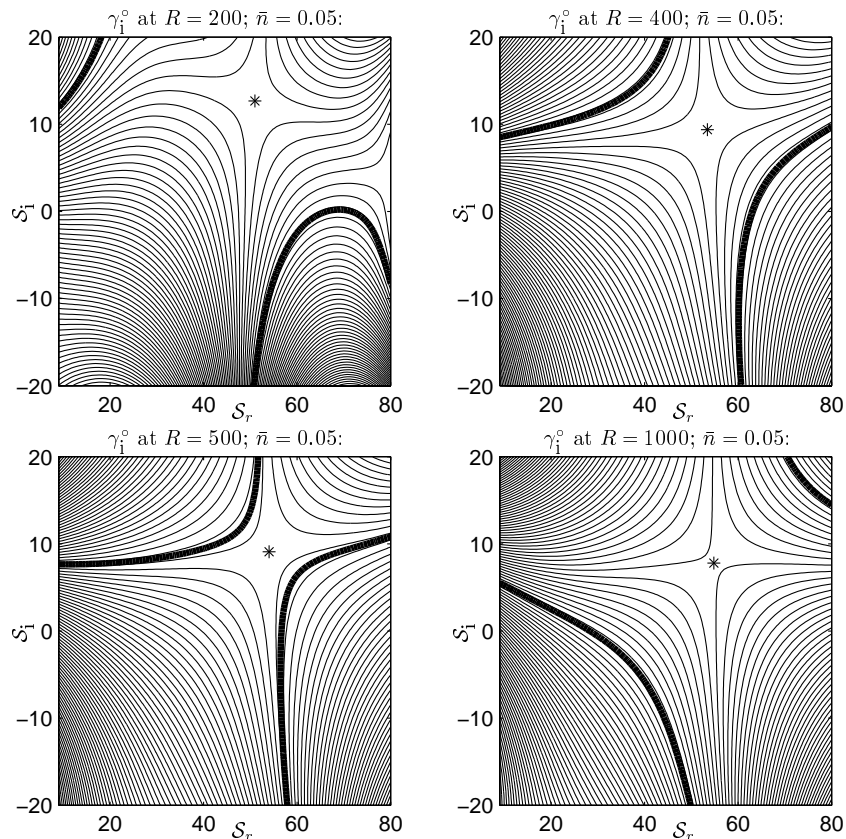


Figure 8.2: Level curves of  $\gamma_i^\circ$  in the complex- $\mathcal{S}$  plane at  $\bar{n} = 0.05$ . Saddle points are marked with '\*'.

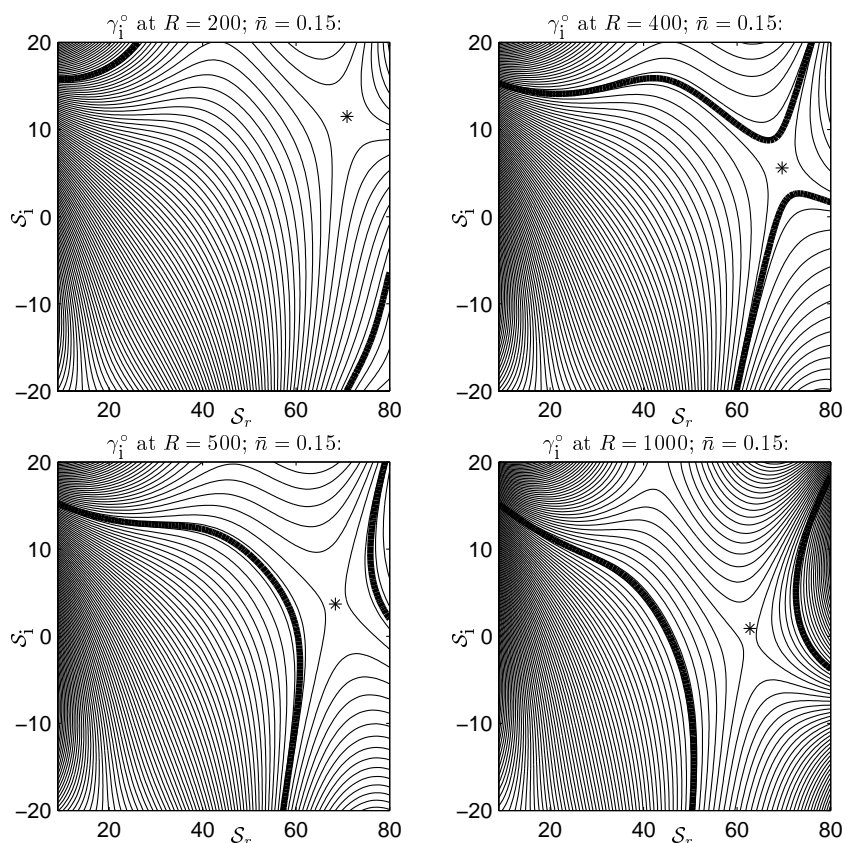


Figure 8.3: Level curves of  $\gamma_i^\circ$  in the complex- $S$  plane at  $\bar{n} = 0.15$ . Saddle points are marked with ‘\*’.

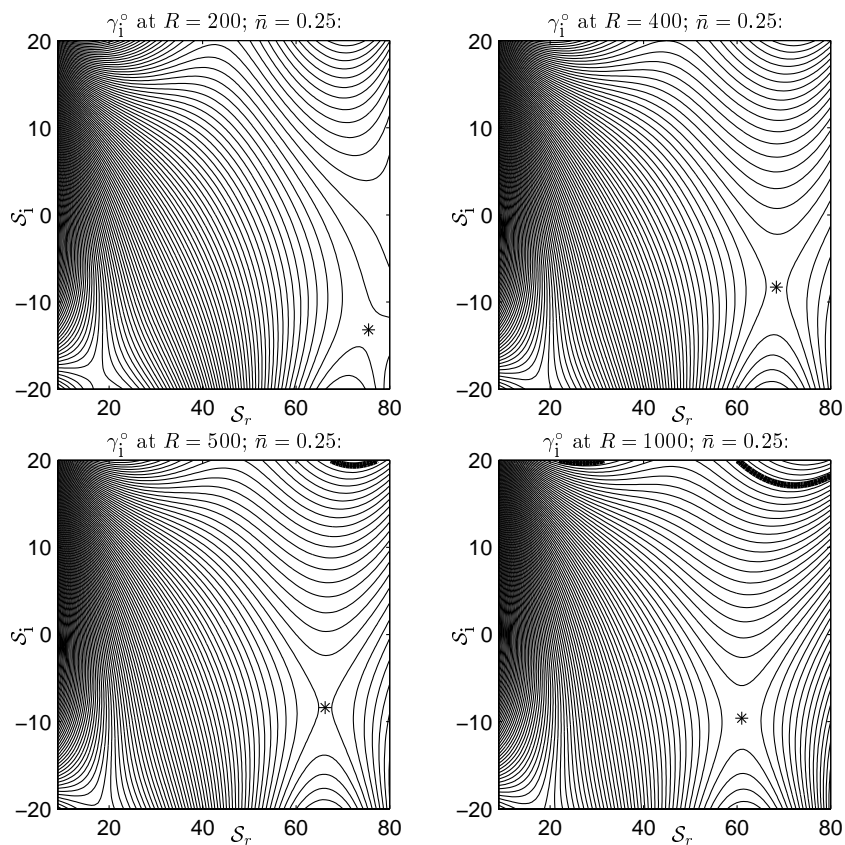


Figure 8.4: Level curves on  $\gamma_i^\circ$  in the complex- $S$  plane at  $\bar{n} = 0.25$ . Saddle points are marked with ‘\*’.

$R$	$\bar{n}$	$\mathcal{S}$	$\gamma_G$
100	0.05	73.6 + 0.6i	0.06668 - 0.01436i
	0.10	60.9 + 16.5i	0.06508 - 0.01382i
	0.15	70.8 + 15.5i	0.08714 - 0.01195i
	0.20	75.6 + 10.6i	0.11341 - 0.01410i
	0.25	78.7 + 4.7i	0.14156 - 0.02013i
200	0.05	51.0 + 12.7i	0.04466 - 0.00525i
	0.10	63.4 + 16.6i	0.06730 - 0.00405i
	0.15	70.9 + 11.5i	0.09418 - 0.00415i
	0.20	75.8 + 6.8i	0.12294 - 0.00697i
	0.25	75.5 - 13.2i	0.15414 - 0.01348i
300	0.05	48.0 + 11.7i	0.04146 - 0.00243i
	0.10	63.1 + 13.5i	0.06914 - 0.00084i
	0.15	70.3 + 8.5i	0.09758 - 0.00148i
	0.20	75.3 + 1.6i	0.12781 - 0.00485i
	0.25	72.1 - 9.4i	0.15890 - 0.01106i
400	0.05	53.4 + 9.4i	0.04327 - 0.00143i
	<b>0.10</b>	<b>63.1 + 11.4i</b>	<b>0.07031 + 0.00087i</b>
	0.15	69.6 + 5.6i	0.09978 - 0.00012i
	0.20	71.8 - 2.8i	0.13077 - 0.00395i
	0.25	68.4 - 8.3i	0.16228 - 0.00979i
500	0.05	54.0 + 9.1i	0.04316 - 0.00027i
	<b>0.10</b>	<b>63.0 + 9.8i</b>	<b>0.07113 + 0.00196i</b>
	<b>0.15</b>	<b>68.4 + 3.7i</b>	<b>0.10123 + 0.00066i</b>
	0.20	68.7 - 4.1i	0.13276 - 0.00340i
	0.25	66.2 - 8.4i	0.16500 - 0.00908i
1000	<b>0.05</b>	<b>54.8 + 7.8i</b>	<b>0.04302 + 0.00240i</b>
	<b>0.10</b>	<b>61.8 + 5.9i</b>	<b>0.07313 + 0.00423i</b>
	<b>0.15</b>	<b>62.8 - 0.9i</b>	<b>0.10515 + 0.00197i</b>
	0.20	61.5 - 6.6i	0.13851 - 0.00263i
	0.25	61.0 - 9.6i	0.17317 - 0.00796i
2000	<b>0.05</b>	<b>55.0 + 6.4i</b>	<b>0.04299 + 0.00412i</b>
	<b>0.10</b>	<b>59.2 + 3.9i</b>	<b>0.07443 + 0.00538i</b>
	<b>0.15</b>	<b>55.9 + 2.0i</b>	<b>0.10742 + 0.00167i</b>
	0.20	57.9 - 11.0i	0.14463 - 0.00336i
	0.25	58.2 - 11.5i	0.18148 - 0.00804i

Table 8.1: Saddle-point location,  $\mathcal{S}_S$ , and associated values of global frequencies  $\gamma_G$ .

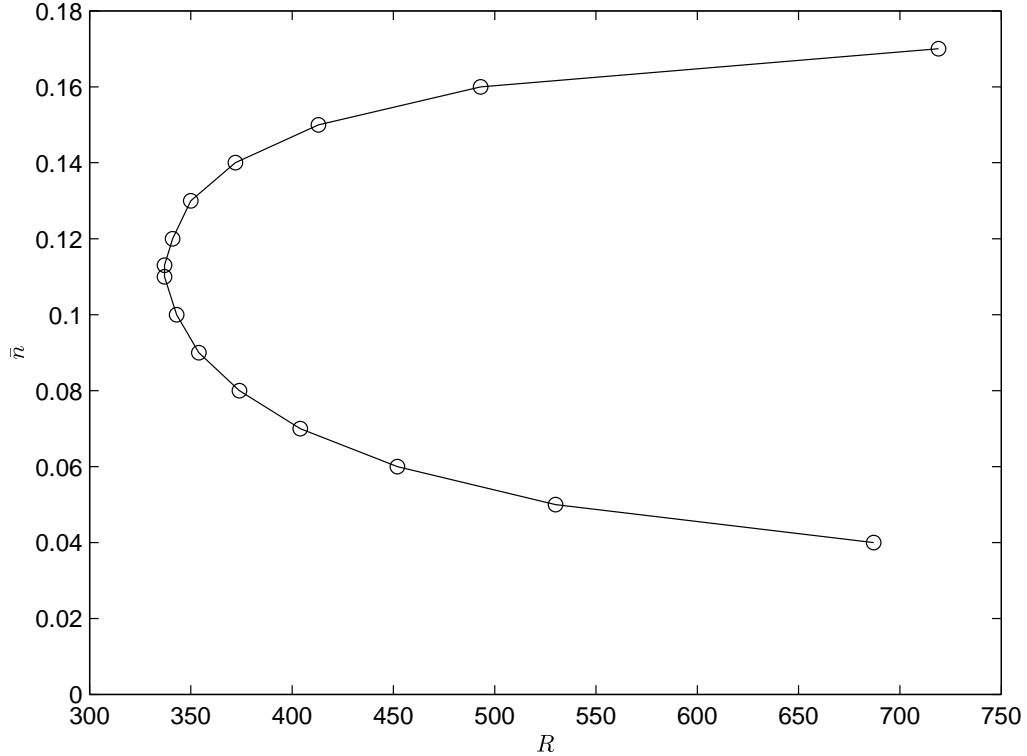


Figure 8.5: Neutral curve for the onset of linear global instability.

The results in Table 8.1 and Figure 8.5 show that a linear global mode exists in the boundary-layer flow over the rotating sphere. The mode is damped for rotation rates corresponding to  $R$  below a critical value of  $R = 337$  (which occurs at  $\bar{n} = 0.11$ ). As the rotation rate is increased beyond this, the range of  $\bar{n}$  for which a self-sustained global mode can exist broadens, reflecting the increased extent of the pockets of absolute instabilities that exist at these parameter values. Interestingly, Table 8.1 shows that the properties of the unstable global mode at each  $R$  appear to be fixed by properties of the flow at latitudes between  $50^\circ$ – $60^\circ$  for all  $R \leq 2000$ , by which point the boundary layer is known to be locally absolutely unstable at all latitudes above approximately  $15^\circ$  (see Garrett & Peake (2002) and Barrow & Garrett (2013)).

We can compare our results to the experimentally-observed onset of turbulence by expressing them in terms of the “spin” Reynolds number,  $R_S$ , used by Kohama & Kobayashi (1983). This is equal to  $R^2$  in our notation. Figure 8.6 places our results alongside those of Sawatzki (1970) and Kohama & Kobayashi (1983). The vertical line corresponds to our calculated minimum Reynolds number for the exis-

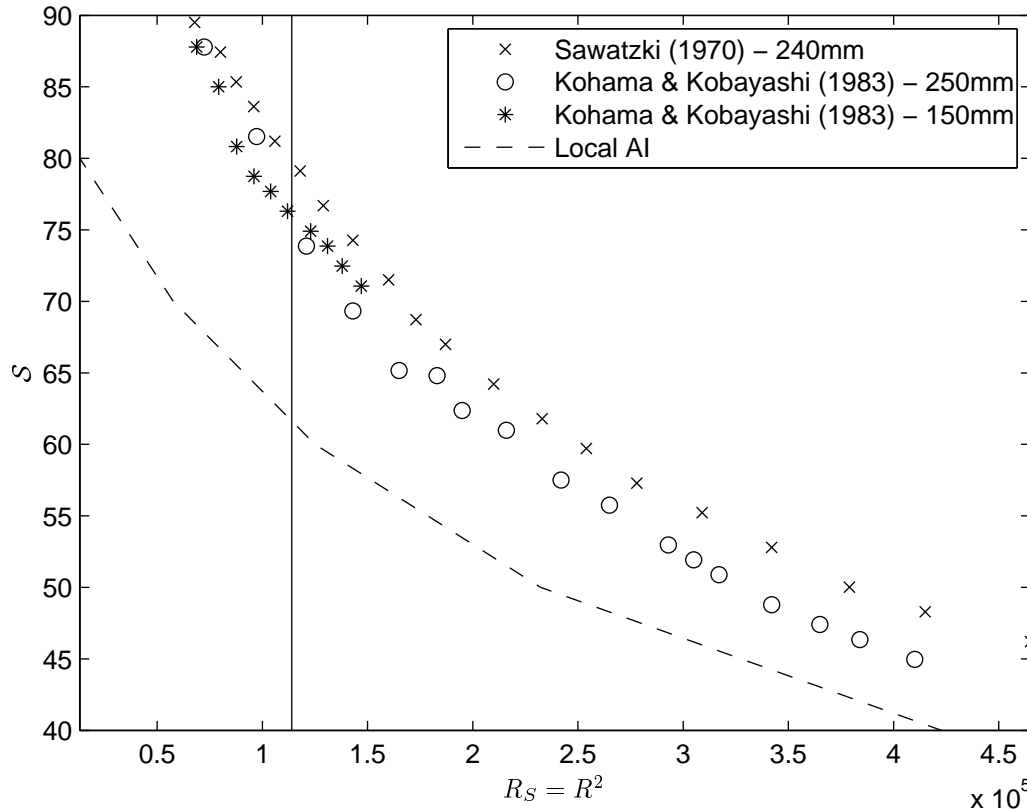


Figure 8.6: Comparison of the experimentally-observed onset of turbulence to our results.

tence of global instability, and the dashed line gives our calculated positions for the onset of local absolute instability. We might expect to see the experimental results asymptotically approach the global instability line; however, turbulence is observed at a lower Reynolds number than our results suggest. The difference (corresponding to roughly 300 units in  $R$  - a discrepancy on the order of 100%) may be attributable to inaccuracies introduced by some combination of, firstly, the Padé approximant method used to predict the global modes; and secondly, the parallel-flow approximation used in the local absolute stability analysis which underpins the inference of the global response. It may also be due to issues with the experimental techniques employed in the studies in the 1970s and 1980s. Close to the equator, where turbulence is first observed, the boundary layer is known to erupt, causing a breakdown of the assumptions made in this work. Further investigation is required to determine whether this discrepancy can be totally explained by these factors, or whether the mechanism of linear global instability is insufficient to accurately predict the occurrence of turbulence.

## 8.4 Conclusions

These results suggest that the boundary-layer flow over a sphere rotating in an otherwise still fluid can support self-sustained linear global modes if it is rotated at a rate such that  $R > 337$ . This conclusion has been reached with knowledge of the local absolute instability properties of the boundary layer, as calculated by Garrett & Peake (2002) and in Chapter 7 of this thesis, which have been used to locate the complex  $\mathcal{S}$  saddle point. The existence of the unstable linear global mode is in contrast to the literature concerning the linear global modes over a rotating disk (Davies & Carpenter (2003) and Pier (2003)), where it is generally accepted that self-sustained linear global modes do not exist. It is important to note that these results do not contradict this result as the unstable linear global mode found on the sphere appears to be fixed by properties of the flow at latitudes between  $50^\circ$ – $60^\circ$ . This location is well away from the pole where the boundary-layer flow over the sphere approximates that of the disk. These results suggest that, despite both being susceptible to local absolute instability, the mechanisms by which transition to turbulence occurs over rotating disks and spheres could be fundamentally different.

# Chapter 9

## Global instability with surface mass-flux and axial flow

Having studied the effects of surface mass-flux and axial flow on local stability in Chapters 5–7, it is appropriate also to consider these parameters in the global analysis, and that is the focus of this chapter. Parameters  $\iota$  and  $\tau$  are as defined in Chapters 3 and 4, respectively. The equations that govern the system are unaltered by the addition of these parameters, and they are solved using an identical process to that of Chapter 8. Changes in the values of  $\iota$  and  $\tau$  are modelled by switching to the appropriate steady-flow velocity profiles that were calculated previously.

As with previous chapters, it is impractical to generate results for finely-grained intervals in each parameter, but the data presented can be usefully treated as a qualitative indication of how changes to  $\tau$  and  $\iota$  typically affect the global stability of the flow. It should also be noted that with the inclusion of positive mass flux (i.e. injection), the critical Reynolds number for the onset of local absolute instability decreases, and in these positions this may negatively affect the validity of our assumption of large  $R$ , or equivalently, small  $\varepsilon$ , used in the formulation of the problem. Consequently, results may become less reliable as  $\iota$  becomes more positive.

For each combination of  $\iota$  and  $\tau$  it is possible to calculate the neutral curve for linear global instability and the corresponding critical Reynolds number, using

$R$	$\bar{n}$	$\mathcal{S}$	$\gamma_G$
100	0.05	55.1 + 13.1i	0.04725 - 0.00697i
	0.10	66.0 + 18.0i	0.06760 - 0.00444i
	0.15	71.0 + 14.2i	0.09218 - 0.00347i
	0.20	75.1 + 9.9i	0.11913 - 0.00562i
	0.25	78.0 + 4.8i	0.14807 - 0.01154i
300	<b>0.05</b>	<b>54.4 + 11.2i</b>	<b>0.04542 + 0.00038i</b>
	<b>0.10</b>	<b>64.1 + 13.1i</b>	<b>0.07184 + 0.00407i</b>
	<b>0.15</b>	<b>69.3 + 9.0i</b>	<b>0.10050 + 0.00381i</b>
	<b>0.20</b>	<b>71.9 + 4.2i</b>	<b>0.13068 + 0.00035i</b>
	0.25	73.0 - 2.0i	0.16215 - 0.00586i
500	<b>0.05</b>	<b>55.1 + 10.2i</b>	<b>0.04498 + 0.00269i</b>
	<b>0.10</b>	<b>63.5 + 10.8i</b>	<b>0.07320 + 0.00608i</b>
	<b>0.15</b>	<b>66.4 + 6.2i</b>	<b>0.10320 + 0.00493i</b>
	<b>0.20</b>	<b>67.4 + 1.1i</b>	<b>0.13453 + 0.00063i</b>
	0.25	66.1 - 3.5i	0.16717 - 0.00589i
1000	<b>0.05</b>	<b>55.6 + 9.0i</b>	<b>0.04456 + 0.00481i</b>
	<b>0.10</b>	<b>61.7 + 8.5i</b>	<b>0.07441 + 0.00764i</b>
	<b>0.15</b>	<b>61.5 + 6.6i</b>	<b>0.10535 + 0.00521i</b>
	0.20	60.4 - 2.9i	0.13915 - 0.00075i
	0.25	59.8 - 4.6i	0.17417 - 0.00714i
2000	<b>0.05</b>	<b>55.9 + 7.8i</b>	<b>0.04426 + 0.00619i</b>
	<b>0.10</b>	<b>60.0 + 7.7i</b>	<b>0.07501 + 0.00856i</b>
	<b>0.15</b>	<b>53.3 - 9.2i</b>	<b>0.10823 + 0.00137i</b>
	0.20	58.1 - 5.3i	0.14479 - 0.00294i
	0.25	55.0 - 6.0i	0.18172 - 0.00915i

Table 9.1:  $\gamma_G$  location and magnitude for  $\iota = 0.5$ ,  $\tau = 0$

the same process used in §8.3 (see Figure 8.5). However, the time required to calculate these precisely is prohibitive of giving good coverage of the parameter space. Therefore, the data presented here consists only of saddle-point location and associated frequency for selected Reynolds numbers and values of  $\bar{n}$ .

Table 9.1 gives the values of  $\mathcal{S}$  and  $\gamma_G$  at the calculated saddle points, subject to half a unit of surface injection, and Table 9.2 gives the same, subject to half a unit of surface suction. Bold text indicates a parameter set where the system is predicted to be globally unstable ( $\gamma_{Gi} > 0$ ).

When considered alongside the data for  $\iota = 0$  in Chapter 8, we see a clear trend of decreasing global stability as  $\iota$  is increased. In the cases considered, we never find a globally-unstable mode for Reynolds numbers below 100, nor is the instability ever present at or above  $\bar{n} = 0.25$ .

$R$	$\bar{n}$	$\mathcal{S}$	$\gamma_G$
100	0.05	58.7 + 9.5i	0.02897 - 0.04073i
	0.10	66.6 + 10.2i	0.05609 - 0.03622i
	0.15	78.7 + 1.7i	0.08810 - 0.03062i
	0.20	76.4 + 9.5i	0.10541 - 0.02825i
	0.25	78.8 + 3.6i	0.13129 - 0.03423i
300	0.05	48.7 + 11.7i	0.04316 - 0.00977i
	0.10	60.4 + 12.3i	0.06494 - 0.00775i
	0.15	69.1 + 7.1i	0.09175 - 0.00922i
	0.20	71.9 - 3.6i	0.12065 - 0.01307i
	0.25	68.1 - 8.8i	0.14993 - 0.01860i
500	0.05	49.0 + 10.1i	0.04047 - 0.00314i
	0.10	60.7 + 8.5i	0.06707 - 0.00347i
	0.15	66.6 + 1.4i	0.09617 - 0.00543i
	0.20	65.9 - 5.7i	0.12656 - 0.00933i
	0.25	64.1 - 9.7i	0.15773 - 0.01429i
1000	0.05	51.0 + 6.1i	0.04036 - 0.00045i
	<b>0.10</b>	<b>59.8 + 3.8i</b>	<b>0.06986 + 0.00005i</b>
	0.15	61.7 - 2.9i	0.10128 - 0.00230i
	0.20	60.6 - 8.1i	0.13410 - 0.00615i
	0.25	60.1 - 11.8i	0.16792 - 0.01064i
2000	<b>0.05</b>	<b>53.4 + 4.6i</b>	<b>0.04068 + 0.00177i</b>
	<b>0.10</b>	<b>57.4 + 0.7i</b>	<b>0.07213 + 0.00197i</b>
	0.15	56.8 - 5.9i	0.10573 - 0.00097i
	0.20	56.2 - 11.9i	0.14116 - 0.00497i
	0.25	57.8 - 15.2i	0.17779 - 0.00885i

Table 9.2:  $\gamma_G$  location and magnitude for  $\iota = -0.5$ ,  $\tau = 0$

$R$	$\bar{n}$	$\mathcal{S}$	$\gamma_G$
100	0.05	53.3 - 3.1i	0.05338 - 0.04170i
	0.10	41.3 + 12.7i	0.07513 - 0.02878i
	0.15	49.3 + 12.1i	0.10195 - 0.03197i
	0.20	60.2 + 11.7i	0.12298 - 0.03440i
	0.25	72.2 + 10.0i	0.14433 - 0.03348i
300	0.05	50.2 + 5.3i	0.04540 - 0.01607i
	0.10	48.4 + 14.1i	0.07569 - 0.01355i
	0.15	66.4 + 14.9i	0.10284 - 0.01118i
	0.20	69.6 + 10.9i	0.13085 - 0.01161i
	0.25	72.2 + 7.3i	0.15931 - 0.01427i
500	0.05	49.6 + 4.8i	0.04443 - 0.01206i
	0.10	47.4 + 15.8i	0.07602 - 0.00850i
	0.15	66.0 + 12.7i	0.10598 - 0.00620i
	0.20	69.2 + 8.4i	0.13577 - 0.00694i
	0.25	71.6 + 3.7i	0.16602 - 0.01019i
1000	0.05	48.8 + 3.8i	0.04384 - 0.00765i
	0.10	61.5 + 15.0i	0.07773 - 0.00308i
	0.15	65.7 + 9.2i	0.10985 - 0.00175i
	0.20	67.6 + 4.3i	0.14156 - 0.00322i
	0.25	66.6 - 0.7i	0.17359 - 0.00749i
2000	0.05	48.2 + 4.0i	0.04380 - 0.00435i
	<b>0.10</b>	<b>61.7 + 11.6i</b>	<b>0.07947 + 0.00000i</b>
	<b>0.15</b>	<b>64.8 + 5.5i</b>	<b>0.11305 + 0.00083i</b>
	0.20	62.8 + 0.9i	0.14619 - 0.00176i
	0.25	60.1 - 4.0i	0.18008 - 0.00699i

Table 9.3:  $\gamma_G$  location and magnitude for  $\iota = 0, \tau = 0.15$

$R$	$\bar{n}$	$\mathcal{S}$	$\gamma_G$
500	0.05	42.3 + 5.7i	0.03803 - 0.04006i
	0.10	55.4 + 12.7i	0.07482 - 0.01368i
	0.15	64.5 + 12.3i	0.10510 - 0.01432i
	0.20	67.6 + 8.5i	0.13447 - 0.01587i
	0.25	70.6 + 5.4i	0.16390 - 0.01845i
1000	0.05	50.3 + 3.0i	0.04177 - 0.01041i
	0.10	58.7 + 12.7i	0.07669 - 0.00847i
	0.15	64.6 + 8.9i	0.10904 - 0.00833i
	0.20	68.3 + 5.1i	0.14077 - 0.00945i
	0.25	71.7 + 0.8i	0.17276 - 0.01202i
2000	0.05	49.9 + 2.4i	0.04224 - 0.00686i
	0.10	60.7 + 9.9i	0.07867 - 0.00458i
	0.15	65.0 + 5.2i	0.11282 - 0.00422i
	0.20	68.5 + 0.3i	0.14662 - 0.00546i
	0.25	68.9 - 6.4i	0.18066 - 0.00850i

Table 9.4:  $\gamma_G$  location and magnitude for  $\iota = -0.5, \tau = 0.15$

$R$	$\bar{n}$	$\mathcal{S}$	$\gamma_G$
500	0.05	48.2 + 4.9i	0.04632 - 0.00895i
	0.10	62.9 + 18.0i	0.07689 - 0.00201i
	<b>0.15</b>	<b>66.7 + 11.9i</b>	<b>0.10690 + 0.00048i</b>
	0.20	67.8 + 7.9i	0.13648 - 0.00107i
	0.25	67.2 + 3.0i	0.16693 - 0.00619i
1000	0.05	47.3 + 4.8i	0.04528 - 0.00481i
	<b>0.10</b>	<b>62.5 + 14.7i</b>	<b>0.07853 + 0.00168i</b>
	<b>0.15</b>	<b>64.0 + 9.8i</b>	<b>0.10992 + 0.00308i</b>
	<b>0.20</b>	<b>62.6 + 5.9i</b>	<b>0.14079 + 0.00024i</b>
	0.25	59.7 + 2.7i	0.17213 - 0.00646i
2000	0.05	46.6 + 5.1i	0.04495 - 0.00185i
	<b>0.10</b>	<b>61.2 + 12.6i</b>	<b>0.07981 + 0.00386i</b>
	<b>0.15</b>	<b>60.0 + 8.6i</b>	<b>0.11205 + 0.00433i</b>
	<b>0.20</b>	<b>58.4 + 5.8i</b>	<b>0.14342 + 0.00047i</b>
	0.25	52.4 - 2.0i	0.17725 - 0.00987i

Table 9.5:  $\gamma_G$  location and magnitude for  $\iota = 0.5, \tau = 0.15$

For comparison, example cases of suction and injection combined with forced axial flow are given in Tables 9.4 and 9.5.

Since no experimental data is available for cases including axial flow or mass flux, we are unable to compare these results to empirical observations.

# Chapter 10

## Conclusions

In this chapter, we will review the work that makes up this dissertation, and discuss the results obtained and their implications.

### 10.1 Review and summary

The first part of this work required us to solve the simplified Navier-Stokes equations that govern the velocity of the steady flow around a rotating sphere, subject to a forced axial flow, and surface suction or injection. This is documented in Chapters 2–4. Results obtained using the NAG solver were compared to those using other solution methods, and the NAG results were determined to be the most accurate. This data underpins the subsequent linear-stability analyses.

In Chapter 5, we first derive the perturbation equations that govern the response resulting from an initial disturbance. The formulation of these equations is such that they do not depend on the axial flow or injection parameters, so they remain unaltered from the form they take in the still-fluid case. Changes in the values of  $\iota$  and  $\tau$  change only the steady mean flow profiles on which the stability analysis is performed.

We consider the onset of linear convective instability by insisting initially that the disturbance rotates at the same rate as the sphere, so that its speed is equal to

the local surface speed. We find that the critical Reynolds number,  $R_c(\theta; \iota, \tau; c = 1)$ , decreases with increased latitudinal distance from the pole. In addition to the still-fluid case, the effects of axial flow and surface mass-flux are considered, and this decrease in  $R_c$  with increased  $\theta$  is found in all considered cases.

Increased axial flow (parameterised by  $\tau$ ) is found to increase  $R_c$  in all cases. However, it also broadens the range of wavenumbers that are susceptible to convective instability. Surface fluid injection ( $\iota > 0$ ) is found to exaggerate the streamline-curvature lobe and lower  $R_c$ , while surface suction ( $\iota < 0$ ) has the opposite effect. For equivalent magnitudes of suction and injection, suction is found to increase  $R_c$  more than injection decreases it, i.e. the flow is more sensitive to surface suction.

We go on to consider non-stationary disturbances that move at a fixed multiple,  $c \neq 1$ , of the sphere surface speed. “Slow” vortices travelling at 0.76 times the local surface speed have been observed experimentally by Kobayashi & Arai (1990). The chosen value of  $c$  was seen to have varying effects on the stability, depending on the magnitude of axial flow and surface suction. Typically, when all other parameters are fixed,  $R_c$  is higher with  $c < 1$ , and lower with  $c > 1$ , but this is not true in all cases. In particular, in the presence of strong surface injection at positions close to the pole,  $R_c$  achieves its lowest value when  $c < 1$ .

For all considered vortex speeds, suction increases  $R_c$ . Axial flow also increases  $R_c$ , except in some cases near to the equator with large values of  $c$ .  $R_c$  is found to be lower at higher latitudes, except in cases near to the equator with small  $c$  and suction.

When we consider the growth rates of the disturbances, we find that “slow” vortices, with  $c < 1$  are the most amplified in all cases. In the still-fluid case ( $\iota = \tau = 0$ ), disturbances with  $c = 0.76$  are found to be the most amplified, which may explain why experiments on the rotating sphere (Kobayashi & Arai (1990)) have shown this speed to be selected.

Of less direct relevance to flow stability are the predicted number and angle of spiral vortices, which are nonetheless included in this work for completeness, and

can be compared to experimental measurements. Typically, as  $c$  is increased, the number of vortices decreases and their angle becomes shallower. Suction and axial flow both act to increase the vortex count, but while suction causes them to assume a shallower angle, axial flow steepens the angle. Vortices are predicted to be more numerous and have steeper angles when they occur at lower latitudes.

In Chapter 7, we consider absolute instability, where the perturbation response is unbounded in time at any spatial location. Absolute instability is identified at all latitudes. Here the disturbance has no associated speed,  $c$ . Qualitatively, surface mass-flux and axial flow affect the critical parameters for absolute instability in the same way as they affect the critical parameters for convective instability, i.e. increased surface suction and axial flow increase  $R_a$ , and injection decreases it. As with convective instability, higher latitudes are found to be more susceptible. These trends hold for every case examined.

The final part of this work is concerned with global instability. It is found that the sphere in still fluid can support a globally-unstable mode when it is rotated at a rate such that  $R > 337$ . This is in contrast to the case of the rotating disk, where Davies & Carpenter (2003) and Pier (2003) predict that absolute instability does not give rise to a self-sustained linear global mode, and a non-linear theory is required to explain the onset of turbulence. That the unstable global mode appears to be fixed by properties of the flow at latitudes well away from the pole suggests that the mechanism by which turbulence arises on the rotating sphere may be distinct from that of the rotating disk, and consequently these results do not contradict their findings.

We also consider the effects of axial flow and surface mass-flux. As with the other instability types, axial flow and suction are seen to increase the minimum Reynolds number required to sustain a globally-unstable mode, while injection decreases it.

## 10.2 Applications

In the aeronautical industry, the optimisation of fuel efficiency and the reduction of noise emissions are considerations of increasing importance in the design of aircraft. These affect not only the costs incurred by both airlines and passengers, but also the environmental impact of air travel in the face of growing demand<sup>1</sup>. With oil supplies decreasing, it is vital to maximise fuel efficiency for sustainability. An important factor in these effects is the drag incurred by the various components that make up the aircraft, and an understanding of the laminar/turbulent nature of the airflow around these components is useful in order to locate areas that could potentially be modified to promote laminar flow. Generally, the goal is to improve the aerodynamics of an aeroplane such that turbulence close to its surface is greatly reduced or eliminated, since turbulence has been identified as causing a significant increase in both drag and noise emissions. It is also beneficial for the air-intake into an aero-engine to be as smooth as possible, since turbulent airflow can increase mechanical wear. The results presented in this dissertation have implications for engineering applications such as these. We have seen that surface suction typically stabilises the boundary layer flow around a sphere, and it might be possible, for example, for a hemispherical nose-cone to employ a mechanism to provide distributed suction over its surface. It will, however, require further research to determine whether the potential efficiency gains provided by such a system are enough to offset the additional fuel use owing to the extra weight the hardware would contribute to the engine.

The theory presented here and in related work may also be of interest in the defence industry, where the accuracy of spinning projectiles, for example, can be adversely affected by turbulence; delaying transition is therefore desirable. An understanding of the transition mechanisms on hemispheres (and also cones) and the parameters that affect them is important. Of course, in the case of engines and projectiles, axial flow speed is not a parameter which can be easily adjusted and

---

<sup>1</sup>See “European Aeronautics: A Vision for 2020” ([http://ec.europa.eu/research/growth/aeronautics2020/pdf/aeronautics2020\\_en.pdf](http://ec.europa.eu/research/growth/aeronautics2020/pdf/aeronautics2020_en.pdf))

exploited as a flow-control mechanism; rather, it has been included to simulate the effects of flight in leading-edge components. These results may, however, be relevant to other kinds of machinery where axial flow could usefully be incorporated for flow control.

Chemical Vapour Deposition (CVD), a process widely used in the semiconductor industry, is another application where the reduction or elimination of turbulence is important. Typically, a gaseous compound is passed over a substrate with which it reacts, and maintaining high precision and uniformity of deposition requires a stable flow. In the manufacture of semiconductors, the rotating disk is typically a more relevant model; however, CVD can also be used for applying thin films of material to surfaces of various geometries, including spheres, and therefore these results form part of a body of research that is applicable to these problems.

Since experimental research on systems such as those described above can be costly, requiring wind-tunnels and specialist equipment, verifiable theoretical results form a valuable basis for this area of research.

### 10.3 Future work

The next stage in this work may be to study the effects of increased rotation rate and the connection between the properties of the rotating sphere near to the pole and the rotating disk, particularly in relation to global modes. As mentioned in §5.3, it would also be interesting to perform an asymptotic study to confirm the results obtained for high Reynolds numbers. Such a study could be carried out without making the parallel-flow assumption. Asymptotic methods have already been applied to similar studies on the rotating disk (Hussain *et al.* (2011)), and the rotating cone (Garrett *et al.* (2009a)).

An absolute instability, which grows temporally, is known to give rise to nonlinear effects given sufficient time. The present study is limited to analysing the linear response of the flow to an initial perturbation, due to the assumption that this

perturbation is small enough to make nonlinear effects negligible. There is scope for further work which considers nonlinear effects on this and similar systems.

Further research is also needed on the effects of compressibility on rotating flows, and indeed, this is the subject of current work by, for example, Towers & Garrett (2012).

# Bibliography

- BANKS, W. H. H., 1965. The boundary layer on a rotating sphere. *Q. J. Mech. Appl. Math.*, 18:443–454.
- BANKS, W. H. H., 1976. Laminar boundary-layer on a rotating sphere. *Acta Mechanica*, 24(24):273–287.
- BARROW, A. & GARRETT, S. J., 2013. Convective and absolute instabilities in the boundary layer over rotating spheres with surface mass flux and incident axial flow. *Eur. J. Mech. B-Fluids*, 38(0):93–100. ISSN 0997-7546. doi:10.1016/j.euromechflu.2012.10.010.
- BARROW, A., GARRETT, S. J. & PEAKE, N., 2013. Global linear stability of the boundary-layer flow over a rotating sphere. In preparation for *J. Fluid Mech.*
- BASSOM, A. P. & SEDDOUGUI, S. O., 1992. The effects of suction on the nonlinear stability of the three-dimensional boundary layer above a rotating disc. *P. R. Soc. London. Series A: Mathematical and Physical Sciences*, 436(1897):405–415. doi:10.1098/rspa.1992.0026.
- BERS, A., 1972. *Linear Waves and Instabilities*. Plasma research report. Research Laboratory of Electronics, Massachusetts Institute of Technology.
- BERS, A., 1984. Space-time evolution of plasma instabilities-absolute and convective. In A. A. Galeev & R. N. Sudan, eds., *Basic Plasma Physics: Selected Chapters, Handbook of Plasma Physics, Volume 1*, volume 1, 451.

- BRIGGS, R. J., 1964. *Electron-stream interaction with plasmas*. M.I.T. Press (Cambridge).
- COOPER, A. J. & CRIGHTON, D. G., 2000. Global modes and superdirective acoustic radiation in low-speed axisymmetric jets. *Eur. J. Mech. B-Fluids*, 19(5):559 – 574. ISSN 0997-7546. doi:10.1016/S0997-7546(00)90101-8.
- CRIGHTON, D. G. & GASTER, M., 1976. Stability of slowly diverging jet flow. *J. Fluid Mech.*, 77:397–413. ISSN 1469-7645. doi:10.1017/S0022112076002176.
- DAVIES, C. & CARPENTER, P. W., 2003. Global behaviour corresponding to the absolute instability of the rotating-disc boundary layer. *J. Fluid Mech.*, 486:287–329. doi:10.1017/S0022112003004701.
- DHANAK, M. R., 1992. Effects of uniform suction on the stability of flow on a rotating disc. *P. R. Soc. London. Series A: Mathematical and Physical Sciences*, 439(1906):431–440. doi:10.1098/rspa.1992.0160.
- VAN DYKE, M., 1982. *An album of fluid motion*. Parabolic Press Stanford, CA.
- EL-SHAARAWI, M. A. I., EL-REFAIE, M. F. & EL-BEDEAWI, S. A., 1985. Numerical solution of laminar boundary layer flow about a rotating sphere in an axial stream. *J. Fluids Eng.*, 107:97–105.
- EL-SHAARAWI, M. A. I., KEMRY, M. M. & EL-BEDEAWI, S. A., 1987. Experiments on laminar flow about a rotating sphere in an air stream. In *Proceedings of the Institution of Mechanical Engineers, Part C: Journal of Mechanical Engineering Science*, volume 201, 427–438. doi:10.1243/PIME\_PROC\_1987\_201\_146\_02.
- FAGE, A., 1936. Experiments on a sphere at critical reynolds numbers. *Aeronaut. Res. C. London*, R & M(1766).
- FURUTA, T., JIMBO, T., OKAZAKI, M. & TOEI, R., 1975. Mass transfer to a rotating sphere in an axial stream. *J. Chem. Eng. Japan*, 8:456–462.

- GARRETT, S. J., 2002. *The stability and transition of the boundary layer on rotating bodies*. Ph.D. thesis, Cambridge University.
- GARRETT, S. J., 2010a. Linear growth rates of types i and ii convective modes within the rotating-cone boundary layer. *Fluid Dyn. Res.*, 42(2):025504. doi:10.1088/0169-5983/42/2/025504.
- GARRETT, S. J., 2010b. Vortex-speed selection within the rotating-disk boundary layer. *Journal of Algorithms & Computational Technology*, 4(1).
- GARRETT, S. J., 2010c. Vortex-speed selection within the boundary-layer flow over a rotating sphere placed in an enforced axial flow. *Eur. J. Mech. B-Fluids*, 29(2):84–92. ISSN 0997-7546. doi:10.1016/j.euromechflu.2009.11.004.
- GARRETT, S. J., 2011. Vortex-speed selection within the transitional region of rotating boundary-layer flows, paper aiaa-2011-3885. In *Proceedings of the 41st AIAA Fluid Dynamics Conference, Honolulu, HI, USA*.
- GARRETT, S. J., HUSSAIN, Z. & STEPHEN, S. O., 2009. Boundary-layer transition on broad cones rotating in an imposed axial flow. In *Proceedings of the 39th AIAA Fluid Dynamics Conference, San Antonio, Texas*, 1184–1194.
- GARRETT, S. J., HUSSAIN, Z. & STEPHEN, S. O., 2009a. The cross-flow instability of the boundary layer on a rotating cone. *J. Fluid Mech.*, 622:209–232. ISSN 1469-7645. doi:10.1017/S0022112008005181.
- GARRETT, S. J. & PEAKE, N., 2002. The stability and transition of the boundary layer on a rotating sphere. *J. Fluid Mech.*, 456:199–218. ISSN 0022-1120. doi:10.1017/S0022112001007571.
- GARRETT, S. J. & PEAKE, N., 2004. The stability of the boundary layer on a sphere rotating in a uniform axial flow. *Eur. J. Mech. B-Fluids*, 23(2):241–253. doi:10.1016/j.euromechflu.2003.08.004.

- GARRETT, S. J. & PEAKE, N., 2007. The absolute instability of the boundary layer on a rotating cone. *Eur. J. Mech. B-Fluids*, 26(3):344–353. ISSN 0997-7546. doi:10.1016/j.euromechflu.2006.08.002.
- GREGORY, N., STUART, J. T. & WALKER, W. S., 1955. On the stability of three-dimensional boundary layers with application to the flow due to a rotating disk. *Philos. T. R. Soc. Lond. A*, 248:155–199.
- GREGORY, N. & WALKER, W. S., 1960. Experiments on the effect of suction on the flow due to a rotating disk. *J. Fluid Mech.*, 9:225–234. ISSN 1469-7645. doi:10.1017/S0022112060001067.
- HEALEY, J. J., 2004. On the relation between the viscous and inviscid absolute instabilities of the rotating-disk boundary layer. *J. Fluid Mech.*, 511:179–199. ISSN 1469-7645. doi:10.1017/S0022112004009565.
- HEALEY, J. J., 2010. Model for unstable global modes in the rotating-disk boundary layer. *J. Fluid Mech.*, 663:148–159. ISSN 1469-7645. doi:10.1017/S0022112010003836.
- HOWARTH, L., 1951. Note on the boundary layer on a rotating sphere. *Philos. Mag.*, 42:1308–1315. doi:10.1080/14786444108561386.
- HUERRE, P. & MONKEWITZ, P. A., 1990. Local and global instabilities in spatially developing flows. *Annu. Rev. Fluid Mech.*, 22:473–537.
- HUSSAIN, Z., 2010. *Stability and transition of three-dimensional rotating boundary layers*. Ph.D. thesis, University of Birmingham.
- HUSSAIN, Z., GARRETT, S. J. & STEPHEN, S. O., 2011. The instability of the boundary layer over a disk rotating in an enforced axial flow. *Phys. Fluids*, 23(11):114108. doi:10.1063/1.3662133.
- IMAYAMA, S., ALFREDSSON, P. H. & LINGWOOD, R. J., 2012. A new way

- to describe the transition characteristics of a rotating-disk boundary-layer flow. *Phys. Fluids*, 24(3):031701. doi:10.1063/1.3696020.
- IMAYAMA, S., ALFREDSSON, P. H. & LINGWOOD, R. J., 2013. An experimental study of edge effects on rotating-disk transition. *J. Fluid Mech.*, 716:638–657. ISSN 1469-7645. doi:10.1017/jfm.2012.564.
- JAIN, M. K. & VENKATARAMAN, M. K., 1966. Calculation of thermal boundary layer on the axially symmetric laminar viscous flow due to rotating bodies of revolution. In *National Inst. of Sciences of India, Proceedings*, volume 35.
- KAPPESSER, R., GREIF, R. & CORNET, I., 1973. Mass transfer to rotating cones. *Appl. Sci. Res.*, 28:442–452. ISSN 0003-6994. doi:10.1007/BF00413082.
- VON KÁRMÁN, T., 1921. Über laminare und turbulente reibung. *Z. Angew. Math. Mech.*, 1(4):233–253.
- KOBAYASHI, R. & ARAI, T., 1990. Spiral vortex behavior in transition region and separation of three-dimensional boundary layers on spheres rotating in axial flow. In D. A. . R. Michel, ed., *Berlin and New York, Springer-Verlag*, 551–557.
- KOBAYASHI, R., ARAI, T. & NAKAJIMA, M., 1988. Boundary layer transition and separation on spheres rotating in axial flow. *Exp. Therm. Fluid Sci.*, 1(1):99–104. ISSN 0894-1777. doi:10.1016/0894-1777(88)90053-2.
- KOBAYASHI, R. & IZUMI, H., 1983. Boundary-layer transition on a rotating cone in still fluid. *J. Fluid Mech.*, 127:353–364. ISSN 1469-7645. doi:10.1017/S0022112083002761.
- KOBAYASHI, R., KOHAMA, Y., ARAI, T. & UKAKU, M., 1987. The boundary-layer transition on rotating cones in axial flow with free-stream turbulence. *JSME International Journal*, 30:423–429.
- KOBAYASHI, R., KOHAMA, Y. & KUROSAWA, M., 1983. Boundary-layer transition

- on a rotating cone in axial flow. *J. Fluid Mech.*, 127:341–352. ISSN 1469-7645. doi:10.1017/S002211208300275X.
- KOBAYASHI, R., KOHAMA, Y. & TAKAMADATE, C., 1980. Spiral vortices in boundary layer transition regime on a rotating disk. *Acta Mechanica*, 35:71–82.
- KOHAMA, Y., 1984a. Behaviour of spiral vortices on a rotating cone in axial flow. *Acta Mechanica*, 51:105–117. ISSN 0001-5970. doi:10.1007/BF01177066.
- KOHAMA, Y., 1984b. Study on boundary layer transition of a rotating disk. *Acta Mechanica*, 50:193–199. ISSN 0001-5970. doi:10.1007/BF01170959.
- KOHAMA, Y. & KOBAYASHI, R., 1983. Boundary-layer transition and the behaviour of spiral vortices on rotating spheres. *J. Fluid Mech.*, 137:153–164. ISSN 1469-7645. doi:10.1017/S0022112083002335.
- LINGWOOD, R. J., 1995a. Absolute instability of the boundary layer on a rotating disk. *J. Fluid Mech.*, 299:17–33.
- LINGWOOD, R. J., 1996. An experimental study of absolute instability of the rotating-disk boundary-layer flow. *J. Fluid Mech.*, 314:373–405.
- LINGWOOD, R. J., 1997c. On the effects of suction and injection on the absolute instability of the rotating-disk boundary layer. *Phys. Fluids*, 9.
- LINGWOOD, R. J. & GARRETT, S. J., 2011. The effects of surface mass flux on the instability of the bek system of rotating boundary-layer flows. *Eur. J. Mech. B-Fluids*, 30(3):299–310. ISSN 0997-7546. doi:10.1016/j.euromechflu.2011.02.003.
- MALIK, M. R., WILKINSON, S. P. & ORSZAG, S. A., 1981. Instability and transition in rotating disk flow. *AIAA J.*, 19:1131–1138.
- MALIK, R. M., 1985. The neutral curve for stationary disturbances in rotating-disk flow. *J. Fluid Mech.*, 164:275–287. ISSN 1469-7645. doi:10.1017/S0022112086002550.

- MANGLER, W., 1945. Boundary layers on bodies of revolution in symmetrical flow. *Ber. Aerodyn Versuchsanst Ber. Aerodyn Versuchsanst. Goett.*
- MANOHAR, R., 1967. The boundary layer on a rotating sphere. *Z. Angew. Math. Phys.*, 18:320.
- MONKEWITZ, P. A., HUERRE, P. & CHOMAZ, J., 1993. Global linear stability analysis of weakly non-parallel shear flows. *J. Fluid Mech.*, 251:1–20. ISSN 1469-7645. doi:10.1017/S0022112093003313.
- NOORDSIJ, P. & ROTTE, J., 1967. Mass transfer coefficients to a rotating and to a vibrating sphere. *Chem. Eng. Sci.*, 22(11):1475–1481. ISSN 0009-2509. doi:10.1016/0009-2509(67)80073-3.
- NOORDZIJ, M. & ROTTE, J., 1968. Mass-transfer coefficients for a simultaneously rotating and translating sphere. *Chem. Eng. Sci.*, 23(6):657–660. ISSN 0009-2509. doi:10.1016/0009-2509(68)89010-4.
- OCKENDON, H., 1972. An asymptotic solution for steady flow above an infinite rotating disc with suction. *Q. J. Mech. Appl. Math.*, 25(3):291–301. doi:10.1093/qjmam/25.3.291.
- PIER, B., 2003. Finite-amplitude crossflow vortices, secondary instability and transition in the rotating-disk boundary layer. *J. Fluid Mech.*, 487:315–343. ISSN 1469-7645. doi:10.1017/S0022112003004981.
- PRESS, W. H., TEUKOLSHY, S. A., VETTERLING, W. T. & FLANNERY, B. P., 1992. Numerical recipes.
- SALZBERG, F. & KEZIOS, S. P., 1965. Mass transfer from a rotating cone in axisymmetric flow. *J. Heat Transf.*, 87:469.
- SAMAD, A. & GARRETT, S. J., 2009. The convective instability of boundary-layer flows over rotating spheroids. In *Proceedings of FEDSM2009*, ASME 2009 Fluids Engineering Summer Meeting.

- SAMAD, A. & GARRETT, S. J., 2010. On the laminar boundary-layer flow over rotating spheroids. *Int. J. Eng. Sci.* doi:10.1016/j.ijengsci.2010.05.001.
- SAMAD, A. & GARRETT, S. J., 2013. On the stability of the boundary-layer flow over rotating spheroids. Submitted to *Int. J. Eng. Sci.*
- SAWATZKI, O., 1970. Das strömungsfeld um eine rotierende kugel. *Acta Mechanica*, 9:159–214.
- STUART, J. T., 1954. On the effects of uniform suction on the steady flow due to a rotating disk. *Q. J. Mech. Appl. Math.*, 7(4):446–457. doi:10.1093/qjmam/7.4.446.
- TANAKA, H. & TAGO, O., 1975. Mass transfer from a rotating sphere in air stream. *Kagaku Kōgaku*, 37:151.
- THOMAS, C., 2007. *Numerical simulations of disturbance development in rotating boundary-layers*. Ph.D. thesis, PhD thesis, Cardiff University, UK.
- TOWERS, P. D. & GARRETT, S. J., 2012. On the stability of the compressible boundary-layer flow over a rotating cone. In *Proceedings of the 42nd AIAA Fluid Dynamics Conference, New Orleans, LA, USA*.
- WILKINSON, S. P. & MALIK, M. R., 1985. Stability experiments in the flow over a rotating disk. *AIAA J.*, 23(4):588–595.